

Electronic Thesis and Dissertation Repository

9-19-2014 12:00 AM

Effect of Gamma Radiation on the Interfacial Reactions and Transfer Processes of Phosphonium-based Ionic Liquids with Carbon Steel

Ryan P. Morco, *The University of Western Ontario*

Supervisor: J. Clara Wren, *The University of Western Ontario*

A thesis submitted in partial fulfillment of the requirements for the Master of Science degree in Chemistry

© Ryan P. Morco 2014

Follow this and additional works at: <https://ir.lib.uwo.ca/etd>

 Part of the [Analytical Chemistry Commons](#), [Physical Chemistry Commons](#), and the [Radiochemistry Commons](#)

Recommended Citation

Morco, Ryan P., "Effect of Gamma Radiation on the Interfacial Reactions and Transfer Processes of Phosphonium-based Ionic Liquids with Carbon Steel" (2014). *Electronic Thesis and Dissertation Repository*. 2442.

<https://ir.lib.uwo.ca/etd/2442>

This Dissertation/Thesis is brought to you for free and open access by Scholarship@Western. It has been accepted for inclusion in Electronic Thesis and Dissertation Repository by an authorized administrator of Scholarship@Western. For more information, please contact wlsadmin@uwo.ca.

**EFFECT OF GAMMA RADIATION ON THE INTERFACIAL
REACTIONS AND TRANSFER PROCESSES OF PHOSPHONIUM-
BASED IONIC LIQUIDS WITH CARBON STEEL**

(Thesis format: Integrated-Article)

by

Ryan P. Morco

Graduate Program in Chemistry

A thesis submitted in partial fulfillment
of the requirements for the degree of
Master of Science

The School of Graduate and Postdoctoral Studies
The University of Western Ontario
London, Ontario, Canada

© Ryan P. Morco 2014

Abstract

This thesis presents work on the effects of ionizing radiation on phosphonium-based ionic liquids (ILs). Ionic liquids are known for their tunable properties which make them attractive options for applications for the separation and sequestration of metal ions from spent nuclear fuels, and candidate lubricants for systems under severe conditions. The high radiation environment found in spent fuel processing may decompose the solvents (ILs) used in the process and affect their separation efficiency. The radiolytic decomposition products can also alter the physical and chemical properties of an IL in ways which can affect the potential corrosion of metal alloys in contact with the IL.

This thesis focusses on the study of phosphonium-based ILs, a class of ILs which has not been extensively investigated, but which holds promise for future applications. The first part of the thesis contains a quantum chemical calculation of the molecular properties of several phosphonium-based ILs using density functional theory. Correlations between the molecular properties (e.g., dipole moment) and physical properties (e.g., viscosity) are explored. The second part of the thesis presents work on the irradiation of these ILs alone or in contact with carbon steel. Pure IL samples were exposed to γ -radiation for up to 192 h and the liquid and gas phases were analyzed using spectroscopic, electrochemical and chromatographic techniques. The results show that the ILs are relatively resistant to radiolytic degradation, but there are measurable quantities of small organic species created from fragmentation of the alkyl ligands of the IL cation. Corrosion of carbon steel in the IL [P₁₄₆₆₆] [Br] was studied with the IL in contact with an inert (Ar) or oxidizing (air) cover gas in the presence and absence of γ -

radiation. Significant corrosion was observed and the extent of the corrosion appeared greater for the tests performed in the absence of γ -radiation. The corrosion is attributed to the presence of impurity H_2O and O_2 dissolved in the IL, and a corrosion mechanism is presented to explain the results.

Keywords:

ionic liquid, gamma-radiolysis, chemical stability, electrolyte property, carbon steel, non-aqueous corrosion, density functional theory

Co-Authorship Statement

This thesis includes published data (Chapter 4) and manuscripts in preparation (Chapter 5 and 6). For the published and prepared results, I was the lead experimental investigator and writer. The research presented in Chapter 4 includes co-authored work. The calculation for that study was performed by Dr. Ahmed Musa with my assistance, while I performed a significant portion of data analysis and writing.

Dedication

**To my Parents
Queenie
& Sam**

Acknowledgements

First and foremost I would like to express my gratitude and admiration to my supervisor, Dr. J. Clara Wren, for her guidance and support throughout my years of graduate education. Clara has provided a fulfilling graduate experience with her dedication to her students. Under her guidance I have learned countless things both personally and professionally. I appreciate all of the time and patience she provided to shape me into the chemist and person I am today.

I would also like to specially thank Drs. Jiju Joseph and Ahmed Musa for the countless hours they spent guiding me through my research. They were always willing to answer my questions and ready to share their knowledge with me.

I would also like to thank Dr. Dave Wren who has been of great assistance in the writing process. His input on styles and techniques in scientific writing has been a great help.

I would also like to thank the members of Wren's group, both past and present, for their years of advice, assistance and support.

To the wonderful people of Surface Science Western and Western Nanofabrication facility, who provided assistance in analyzing my samples, your help are very much appreciated.

Finally, I would like to thank my family for giving me the inspiration to keep going. To my wife Queenie, for her love, support and patience throughout my life as a graduate student. And to my son Samuel Acyl, who inspire and makes me happy all the time. This thesis is dedicated to them.

Table of Contents

Abstract	ii
Co-Authorship Statement.....	iv
Dedication	v
Acknowledgements.....	vi
Table of Contents	vii
List of Symbols, Acronyms, and Ionic Liquids	xi
List of Tables	xiv
List of Figures	xv
Chapter 1: Introduction	1
1.1 Thesis Objective and Organization.....	1
Chapter 2: Background and Literature Review	5
2.1 Materials and Background	5
2.1.1 Ionic Liquids	5
2.1.2 Physical and chemical properties of ionic liquids.....	7
2.1.3 Phosphonium-based ionic liquids	10
2.2 Radiation Background	12
2.2.1 Ionizing Radiation.....	12
2.2.2 Radiation Interaction to Matter	13
2.2.3 Radiation-induced chemistry	15
2.2.3.1 Water Radiolysis.....	16
2.2.3.2 Ionic Liquid/Organic Liquid Radiolysis	19
2.3 Corrosion Background.....	20

2.4 Ionic Liquids, Radiation and Corrosion.....	22
2.5 References.....	23
Chapter 3: Experimental Principles and Details	27
3.1 Sample Analysis Techniques	27
3.1.1 Gas Chromatography-Mass Spectrometry.....	27
3.1.2 UV-Visible Spectrophotometry	29
3.1.3 Raman Spectroscopy.....	31
3.1.4 Fourier Transform Infrared Spectroscopy (FTIR)	34
3.1.5 Nuclear Magnetic Resonance Spectroscopy (NMR)	35
3.1.6 Electrochemical Impedance Spectroscopy (EIS).....	35
3.2 Surface Analyses.....	39
3.2.1 X-Ray Photoelectron Spectroscopy (XPS)	39
3.2.2 Scanning Electron Microscopy/ Energy Dispersive X-ray Spectroscopy (SEM/EDX)	41
3.3 Experimental Procedures	44
3.3.1 Sample Preparation	44
3.3.1.1 Ionic Liquid Radiolysis Test.....	44
3.3.1.2 Ionic Liquid Corrosivity Test	44
3.3.2 Sample Irradiation.....	46
3.3.3 Sample Analysis.....	46
3.3.3.1 Ionic Liquid Radiolysis Test.....	46
3.3.3.2 Ionic Liquid Corrosivity Test	48
3.4 References.....	48

Chapter 4: The Molecular Structures and the Relationships between the Calculated and Observed Bulk Phase Properties of Phosphonium-Based Ionic Liquids	50
4.1 Introduction.....	50
4.2 Methodology	52
4.2.1 Computational Details	52
4.2.2 Spectroscopic Measurements.....	54
4.3 Results and Discussion	54
4.3.1 Optimized Geometries	54
4.3.2 IR and UV-Vis Spectra	62
4.3.3 Correlations between Molecular and Bulk Properties	67
4.4 Conclusions.....	72
4.5 References.....	73
Chapter 5: The Chemical Stability of Phosphonium-based Ionic Liquids under Gamma Irradiation	75
5.1 Introduction.....	75
5.2 Experimental.....	78
5.2.1 Materials and Sample Preparation	78
5.2.2 Test Vial Irradiation Analysis	78
5.3 Results and Discussion	79
5.3.1 Background on the Interaction of a γ -Photon and with an IL.....	79
5.3.2 Airborne Radiolysis Products	81
5.3.3 Spectroscopic Analyses of the IL Phases.....	84
5.3.3.1 The [P ₁₄₆₆₆] ILs	85
5.3.3.2 Short Carbon Chain ILs	91
5.3.4 Conductivity.....	95
5.3.5 Comparison with Other Studies on the Irradiation of ILs.....	96
5.4 Summary.....	98

5.5 References.....	99
Chapter 6: Corrosion Behaviour of Carbon Steel in the [P14666][Br] Ionic Liquid: The Effects of γ-Radiation and Cover Gas	102
6.1 Introduction.....	102
6.2 Experimental.....	104
6.2.1 X-ray Photoelectron Spectroscopy	104
6.2.2 Scanning Electron Microscopy/ Energy Dispersive X-ray Spectroscopy ..	105
6.2.3 Raman Spectroscopy.....	105
6.3 Results.....	106
6.3.1 The Physical and Chemical Properties of the [P14666] [Br] IL	106
6.3.2 Corrosion Behaviour in the Absence of Radiation	107
6.3.3 Corrosion Behaviour in the Presence of γ -Radiation.....	115
6.3.4 Corrosion Behaviour in 20 % Hexane and 80% [P14666] [Br] Mixture....	123
6.4 Proposed Corrosion Mechanism.....	128
6.5 Conclusions.....	134
6.6 References.....	135
Chapter 7: Summary and Future Work.....	138
7.1 Summary.....	138
7.2 Future Work	140
Appendix A	144
Copyright Permission.....	144
Curriculum Vitae	151

Symbols, Acronyms, and Ionic Liquids

Symbols

A	electrode area
A	absorbance
b	coherent scattering length
C	capacitance
c	concentration
cP	centipoise
e	electron charge
E°	electrode potential
E_{EQ}	elquilibrium potential
E_{amp}	amplitude of electrochemical impedance spectroscopy sinusoidal potential
ΔE	interaction energy
F	Faraday constant
f	oscillator strength
h	Plank constant
I_o	incident radiation
I	transmitted radiation
I	current
I_{amp}	EIS current amplitude
j	imaginary unit
k_B	Boltzmann constant
ℓ	distance between two electrodes
l	cuvette's path length
m/z	mass to charge ratio
P_{esc}	escape probability
R	resistance
R	gas constant
r_c	Onsager Radius
T	transmittance
T_{mp}	melting point
T	absolute temperature (K)
Z	impedance
Z_{im}	imaginary impedance
Z_r	real impedance
ΔE_{H-L}	HOMO-LUMO energy gap
ϵ_o	dielectric constant of permittivity in a vacuum

ϵ_r	dielectric permittivity of a medium
ϵ	extinction coefficient
η	viscosity
η_e	detector efficiency
θ	phase shift
λ	wavelength
μ	dipole moment
ν_i	incident photon frequency
ν	scattered photon frequency
ν_{vib}	vibrational frequency
ϕ	work function
ρ	density
σ	conductivity of a system
ω	angular frequency

Acronyms

ATR	Attenuated Total Reflectance
BE	Binding Energy
BLYP	Becke-Lee-Yang-Parr
CS	Carbon Steel
DFT	Density Functional Theory
DNP	Double Numeric Plus Polarization
DSC	Differential Scanning Calorimetry
ECD	Electron Capture Detector
EDX	Energy Dispersive X-ray Spectroscopy
EIS	Electrochemical Impedance Spectroscopy
ESI-MS	Electrospray Ionization-Mass Spectrometry
FIB	Focused Ion Beam
FTIR	Fourier Transform Infrared Spectroscopy
GC/MS	Gas Chromatography-Mass Spectrometry
GGA	Generalized Gradient Approximation
HOMO	Highest Occupied Molecular Orbital
ICP-MS	Inductively Coupled Plasma Mass Spectrometry
IL	Ionic Liquid
IR	Infrared
KE	Kinetic Energy

LET	Linear Energy Transfer
LUMO	Lowest Unoccupied Molecular Orbital
MD	Molecular Dynamics
MSD	Mass Selective Detector
MSD	Mean Square Displacement
NMR	Nuclear Magnetic Resonance
PTFE	Polytetrafluoroethylene
PUREX	Plutonium Uranium Redox Extraction
PW91	Perdew-Wang 1991
RTIL	Room-Temperature Ionic Liquid
SEM	Scanning Electron Microscopy
SSW	Surface Science Western
TCD	Thermal Conductivity Detector
TD-DFT	Time-Dependent Density Functional Theory
UV-Vis	Ultraviolet and Visible
XPS	X-ray Photoelectron Spectroscopy

Ionic Liquids

[P ₁₄₆₆₆] [Cl]	Tetradecyl(trihexyl)phosphonium chloride
[P ₁₄₆₆₆] [Br]	Tetradecyl(trihexyl)phosphonium bromide
[P ₁₄₆₆₆] [NTf ₂]	Tetradecyl(trihexyl)phosphonium bis(trifluoromethylsulfonyl)imide
[P ₁₄₆₆₆] [DCA]	Tetradecyl(trihexyl)phosphonium dicyanamide
[P ₁₄₆₆₆] [PF ₆]	Tetradecyl(trihexyl)phosphonium hexafluorophosphate
[P ₁₄₆₆₆] [BF ₄]	Tetradecyl(trihexyl)phosphonium tetrafluoroborate
[P ₄₁₁₁] [MeSO ₄]	Tributylmethylphosphonium methyl sulfate
[PTiBMe] [TsO]	Triisobutylmethylphosphonium tosylate

List of Tables

Table 1.1	Ionic liquids used in this thesis with their given full names, short names and Cytec IL number3
Table 4.1	Hydrogen bond lengths (Å) and angles for phosphonium-based ILs58
Table 4.2	Calculated properties for the phosphonium-based ILs61
Table 5.1	The physical properties of the ionic liquids investigated (T = 25 °C)65
Table 5.2	The major radiolytic decomposition products of ionic liquids detected in the gas phase using GC-MS76
Table 6.1	The chemical and physical properties (T = 25 °C) of [P ₁₄₆₆₆] [Br]108
Table 6.2	EDX elemental analysis results (in atomic %) of the surfaces of the carbon steel coupons corroded in [P ₁₄₆₆₆] [Br] exposed to different cover gases112
Table 6.3	Dissolved iron concentration in [P ₁₄₆₆₆] [Br] after 96 h corrosion of carbon steel exposed to different cover gases in the absence and presence of γ -irradiation116
Table 6.4	XPS analysis results of Fe speciation (in atomic %) in the surface layer of the carbon steel coupons corroded in [P ₁₄₆₆₆] [Br] exposed to different cover gases in the absence and the presence of γ -irradiation122
Table 6.5	EDX elemental analysis (in atomic %) of the surfaces of carbon steel coupons corroded in 20% hexane in [P ₁₄₆₆₆] [Br] solutions exposed to different cover gases129
Table 6.6	Key reactions and transport processes involved in the electrochemical corrosion of carbon steel131

List of Figures

Figure 2.1	Most commonly used cations and anions in ILs [18]	7
Figure 2.2	Penetration depth of ionizing radiation and density of excited species in water	4
Figure 2.3	The radiation track resulting from a γ -photon [43].....	17
Figure 2.4	Schematic of the initial reactions and the approximate time scales that occur in water to generate the primary radiolysis products during absorption of ionizing radiation [44]	17
Figure 3.1	Gas chromatogram of the headspace gas from a test with a pure IL irradiated for 192 hours. Insets are the mass spectra from the a) hexane and b) hexane peaks	29
Figure 3.2	Illustration of a diode array UV-Vis spectrophotometer	31
Figure 3.3	Illustration showing Rayleigh scattering, Stokes (Raman) scattering, and Anti-Stokes (Raman) scattering	33
Figure 3.4	Illustration of the relative peak intensities of Rayleigh scattering, Stokes (Raman) scattering, and Anti-Stokes (Raman) scattering	33
Figure 3.5	The (a) purely resistive and (b) purely capacitive impedance response arising from a given electrochemical impedance experiment [13].....	37
Figure 3.6	Schematic representation of a single photon/electron ejection process	40
Figure 3.7	Schematic diagram of a scanning electron microscope with an energy dispersive X-ray detector. Image source: http://www.purdue.edu/rem/rs/sem.htm	43
Figure 3.8	Photographs of the vial and carbon steel mount assembly	45
Figure 4.1	Chemical structures of the phosphonium cation and the anions of the ILs used in this study	52
Figure 4.2	The equilibrium geometries of phosphonium ILs. Dashed lines represent the hydrogen bonds between the atoms. The colour assignments for the atoms are: purple - P, maroon - Br, blue - N, red - O, yellow - S, light-blue - F, peach - B, dark-gray - C atoms, and light-gray - H.....	56
Figure 4.3	Electrostatic potentials of phosphonium ILs mapped onto an electron density isosurface of 0.017 e/au^3 . The electron density scale spans -0.09 (red) through 0.0 (green) to $+0.09$ (blue).....	59

Figure 4.4	Measured (the top panel) and calculated (the lower two panels) IR spectra of selected ILs. The calculated results were obtained using two functionals, BLYP and PW91.....	63
Figure 4.5	Calculated electronic transition lines overlaid on the measured UV-Visible spectra of selected ILs. The calculated results were obtained using the BLYP functional	66
Figure 4.6	Relationship between the calculated dipole moments and the molar conductivity of the phosphonium ILs. The conductivity values were taken from ref. [52]. The solid and open symbols are the calculated values using the BLYP and PW91 functionals, respectively.....	68
Figure 4.7	Relationship between the calculated interaction energy (ΔE) and the viscosity of the phosphonium ILs. The viscosity values were taken from ref. [52]. The solid and open symbols are the calculated values using the BLYP and PW91 functionals, respectively	69
Figure 4.8	Relationship between the calculated dipole moment and the viscosity of the phosphonium ILs. The viscosity values were taken from ref. [52]. The solid and open symbols are the calculated values using the BLYP and , respectively	69
Figure 4.9	Relationship between the calculated interaction energy (ΔE) and the melting point (T_{mp}) of the phosphonium ILs. The melting points were taken from ref. [54]. The solid and open symbols are the calculated values using the BLYP and PW91 functionals, respectively.....	71
Figure 5.1	The physical properties of the ionic liquids investigated ($T = 25\text{ }^{\circ}\text{C}$).....	75
Figure 5.2	Photographs of irradiated [P ₁₄₆₆₆] [Br] and the corresponding UV-Vis, FTIR and Raman spectra as a function of irradiation time. Black, blue and red lines are at 0, 96 and 192 h, respectively	85
Figure 5.3	Photographs of irradiated [P ₁₄₆₆₆] [NTf ₂] and the corresponding UV-Vis, FTIR and Raman spectra as a function of irradiation time. Black, blue and red lines are at 0, 96 and 192 h, respectively	87
Figure 5.4	Photographs of irradiated [P ₁₄₆₆₆] [DCA] and the corresponding UV-Vis, FTIR and Raman spectra as a function of irradiation time. Black, blue and red lines are at 0, 96 and 192 h, respectively	89
Figure 5.5	Photographs of irradiated [P ₄₄₄₁] [MeSO ₄] and the corresponding UV-Vis, FTIR and Raman spectra as a function of irradiation time. Black, blue and red lines are at 0, 96 and 192 h, respectively. The blue and red lines are heavily overlapping for the Raman and FTIR spectra	93

Figure 5.6	Photographs of irradiated [PTiBMe] [TsO] and the corresponding UV-Vis, FTIR and Raman spectra as a function of irradiation time. Black, blue and red lines are at 0, 96 and 192 h, respectively95
Figure 5.7	Conductivities of phosphonium ILs as a function of irradiation time: ● [P ₁₄₆₆₆] [DCA], ▲ [P ₁₄₆₆₆] [Br], ■ [P ₁₄₆₆₆] [NTf ₂], ◀ [PTiBMe] [TsO] and ▼ [P ₄₄₄₁] [MeSO ₄]97
Figure 6.1	SEM images and the Raman spectra of carbon steel surfaces corroded for 96 h in [P ₁₄₆₆₆] [Br] in the absence of γ -radiation, where the IL was exposed to: (top) open air, (middle) sealed air and (bottom) argon.....109
Figure 6.2	Reference Raman spectra of iron oxides and oxyhydroxide minerals112
Figure 6.3	XPS spectra taken from a carbon steel surface corroded for 96 h in [P ₁₄₆₆₆] [Br] exposed to open air in the absence of γ -irradiation. The survey spectrum in the binding energy of 0 to 1100 eV and the high resolution spectra of the C 1s, O 1s, and Fe 2p bands are shown. The inset in the Fe 2p spectrum shows the deconvoluted Fe _x O _y components, each consisting of multiple peaks.....113
Figure 6.4	The SEM images with different magnifications of the cross section of the carbon steel coupons corroded for 96 h in [P ₁₄₆₆₆] [Br] exposed to open air in the absence of γ -irradiation115
Figure 6.5	SEM images and Raman spectra of the carbon steel coupon surfaces corroded for 96 h in [P ₁₄₆₆₆] [Br] under γ -irradiation where the IL was exposed to: (top) open air, (middle) sealed air and (bottom) argon.....118
Figure 6.6	Cross-sectional SEM image of a carbon steel surface corroded for 96 h in [P ₁₄₆₆₆] [Br] in argon under γ -irradiation119
Figure 6.7	XPS spectra taken from a carbon steel surface corroded for 96 h in [P ₁₄₆₆₆] [Br] exposed to Ar under γ -irradiation. The survey spectrum in the binding energy of 0 to 1100 eV and the high resolution spectra of the C 1s, O 1s, and Fe 2p bands are shown. The inset in the Fe 2p spectrum shows the deconvoluted Fe _x O _y components, each consisting of multiple peaks 120
Figure 6.8	XPS spectra taken from a carbon steel surface corroded for 96 h in [P ₁₄₆₆₆] [Br] exposed to open air under γ -irradiation. The survey spectrum in the binding energy of 0 to 1100 eV and the high resolution spectra of the C 1s, O 1s, and Fe 2p bands are shown. The inset in the Fe 2p spectrum shows the deconvoluted Fe _x O _y components, each consisting of multiple peaks121
Figure 6.9	SEM images and the Raman spectra of carbon steel surfaces corroded for 96 h in 20% hexane in [P ₁₄₆₆₆] [Br] solutions, where the IL was exposed to: (top) open air, (middle) sealed air and (bottom) argon.....126

Figure 6.10 SEM image with the elemental distribution of a (top) carbon steel coupon surface corroded for 96 h contact in a 20% hexane in [P₁₄₆₆₆] [Br] solution in argon. Also shown in (bottom) is the cross-sectional image of the coupon surface128

Figure 6.11 A schematic illustration of corrosion reactions in the presence of a surface film. The key reaction steps include: (1a) metal oxidation coupled with (1b) reduction of solution species (in this case H₂O and O₂), (2) net metal cation transport across the solid oxide film, (3) growth of the surface film, and (4) dissolution of a metal cation into the electrolyte solution131

Chapter 1

Introduction

1.1 THESIS OBJECTIVE AND ORGANIZATION

The main objective of this thesis research was to develop a mechanistic understanding of the effect of ionizing radiation on ionic liquids (ILs) and how will this influence the corrosion of carbon steel in contact with an IL. Ionic liquids have drawn the attentions of many researchers around the world because of their excellent physicochemical properties, such as high thermal and chemical stability, non-flammability, negligible vapour pressure, and low melting points. Such versatility makes ILs potential engineering fluids for industrial application such as spent nuclear fuel reprocessing and high performance lubricants under severe conditions where most conventional oils and greases fail. However before they can be utilized for such applications, their stability, reactivity and compatibility with other materials has to be fully understood. This is special concern for the spent fuel application where ionizing radiation is present, since this may lead to IL radiolytic decomposition and affect its listed properties.

Exposed to ionizing radiation, water decomposes to a range of reducing ($\bullet e_{aq}^-$, $\bullet O_2^-$, $\bullet H$) and oxidizing (O_2 , $\bullet OH$, $HO_2\bullet$, H_2O_2) species. Likewise, when exposed to ionizing radiation, ILs undergo radiolysis, forming excited species and radiolytic fragments. The presence of these decomposition products (which can be redox active

species too) in the IL can have an effect on the physicochemical properties of the IL and may alter the corrosivity of ILs.

The work covered in this thesis includes a theoretical investigation of IL molecular structure and property relationships, tests on the effect of ionizing radiation on the chemical stability of ILs and corrosion tests with carbon steel. The corrosion behaviour of carbon steel in a non-aqueous environment such as an IL has been rarely studied. There have been other theoretical studies of ILs, mainly focused on imidazolium ILs and very few studies on the radiation stability of ILs. This work studied the properties and behaviour of phosphonium-based ILs which have not been examined by others.

Eight phosphonium-based ILs which possess various physical and chemical properties were investigated theoretically and/or experimentally. The studied ILs are listed in Table 1.1 followed by the groups of experiments performed in the order in which they are presented in this thesis.

Table 1.1 Ionic liquids used in this thesis with their given full names, short names and Cytec IL number.

Cytec IL No.	Full Name	Short Name
IL 101	tetradecyl(trihexyl)phosphonium chloride	[P ₁₄₆₆₆] [Cl]
IL 102	tetradecyl(trihexyl)phosphonium bromide	[P ₁₄₆₆₆] [Br]
IL 105	tetradecyl(trihexyl)phosphonium dicyanamide	[P ₁₄₆₆₆] [DCA]
IL 106	triisobutylmethylphosphonium tosylate	[PTiBMe] [TsO]
IL 108	tributylmethylphosphonium methyl sulfate	[P ₄₁₁₁] [MeSO ₄]
IL 109	tetradecyl(trihexyl)phosphonium bis(trifluoromethylsulfonyl) imide	[P ₁₄₆₆₆] [NTf ₂]
IL 110	tetradecyl(trihexyl)phosphonium hexafluorophosphate	[P ₁₄₆₆₆] [PF ₆]
IL 111	tetradecyl(trihexyl)phosphonium tetrafluoroborate	[P ₁₄₆₆₆] [BF ₄]

- Computational study of the molecular structures of phosphonium-based ILs to acquire a better understanding on the exhibited physicochemical properties of ILs. The quantum parameters that were obtained were correlated with the observed physicochemical properties of the ILs.
- The effect of ionizing radiation on the stability and decomposition of ILs as a function of irradiation time was examined. Characterization using chromatographic, spectroscopic and electrochemical techniques was carried out to study the changes in the ILs.

- The corrosion behaviour of carbon steel in one IL ([P₁₄₆₆₆] [Br]) when subjected to gamma irradiation and contact with oxidizing and non-oxidizing atmospheres was investigated. A range of surface analytical techniques were utilized to study the carbon steel surface. A mechanism to explain the dependence of observed corrosion on the test conditions is presented.

Chapter 2

Background and Literature Review

2.1 MATERIALS BACKGROUND

2.1.1 Ionic liquids

Room temperature ionic liquids (RTILs) are composed of distinct ion pairs that remain in the liquid state below 100 °C. They usually contain a bulky, long-chained organic cation that is weakly coordinated to a smaller organic or inorganic anion. Recently interest in RTILs has grown due to their many desirable physical and chemical properties. These include: good conductivity, negligible vapour pressure, high chemical and thermal stability and a wide electrochemical window [1-5]. Ionic liquids are often termed 'designer solvents' because their properties can be easily tuned by varying the structure of the component ions [4-6]. These desirable properties make this class of liquids particularly interesting to study as potential replacements for traditional volatile organic solvents for use in a wide range of applications [3, 7, 8] such as for synthesis [4, 9], catalysis [4, 10], polymers [11], separations [12], electrochemistry [13, 14], energy storage [15, 16], supercritical fluid [17].

There is an enormous number of possible ILs; Rogers and Seddon [3] estimated the number to exceed one trillion. This figure was estimated more than a decade ago and this number was expected to rise to a quintillion if all the known cation and anion combinations could be paired [1, 18].

The structure of the cation and anion in a given IL dictates the properties that the particular IL possesses. Melting points, for example, are greatly influenced by the size and shape of the cation [5]. The large sizes of the IL components as well as the asymmetric nature of the cations tends to lower the melting point of the IL [18]. Lower melting points result from a reduction in the magnitude of the Coulombic attraction between the components and a decrease in their packing efficiency. The polarity of the ILs is influenced by the size of their side alkyl chains. Increasing the length of an alkyl chain in the cation tends to decrease water solubility by increasing the hydrophobicity of the cation [2, 19]. Also, the choice of the anion can change the water miscibility of an IL as shown in 0 [18]. There are many possible variations in properties for different ILs for these reasons. Even ILs containing the same cation and different anions can possess dramatically different physical and chemical properties [5, 6, 20]. In this thesis, trends in the physicochemical properties of ionic liquids with the same cation but different anion are presented.

The most commonly used ionic liquid pairs are illustrated in 0. Despite the numerous IL cations and anions available, most research so far has focused on only a few commonly used IL types. The cations largely studied are: imidazolium, pyridinium, piperidinium, ammonium, phosphonium, pyrrolidinium, pyrazolium, thiazolium, and sulfonium. Their structures are shown in Figure 2.1.

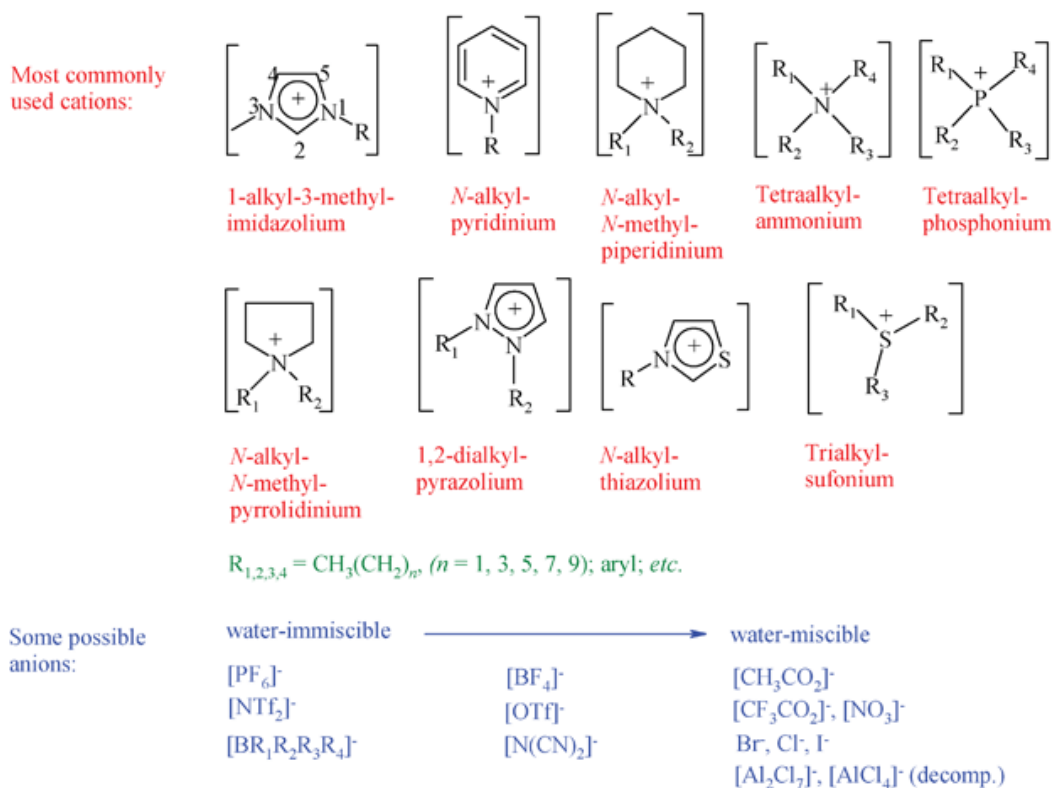


Figure 2.1 Most commonly used cations and anions in ILs [18].

2.1.2 Physical and chemical properties of ionic liquids

The physical and chemical properties of ILs depend on the nature and size of both their cation and anion components. Generalizations regarding the properties of ILs are simply not true for all the IL ion combinations. For example, studies by various authors have revealed no correlation between an IL structure and its melting point, and generalities on trends in IL properties can only sometimes be made for related ILs, where the related ILs, or ILs in a series, contain the same cation type [5, 21-23].

Ionic liquids have a low melting point and many of them are liquids at room temperature. The melting point of an IL can be varied with the choice of cation and

anion. The melting point can be significantly influenced by the size and type of its component ions which control the strength of the Coulombic interaction between ion pairs and their packing efficiency. If the size or shape of either a cation or anion changes, it can affect its ability to closely pack, which then significantly affects the melting point [1, 5]. Aside from the size and shape of the component ions, symmetry also has a significant role in determining the melting point of an IL, because the symmetry dictates how well the ions will efficiently pack into a crystal lattice. The lengths of the alkyl chains on the cation can also have an impact on the melting point. Longer alkyl chains normally interact with the neighbouring molecules through the van der Waals interaction which helps to dictate inter-component binding and the melting points [2, 5].

Ionic liquids are generally more viscous than conventional solvents, with viscosities ranging from 10 centipoise (cP) to well above 500 cP [5]. Compared to molecular solvents, the viscosity of an IL is closer to that of motor oil [2, 5]. As a point of reference, at room temperature the viscosities of water, ethylene glycol, and glycerol are 0.890 cP, 16.1 cP, and 934 cP respectively [24]. Although generalities can be found for the trend in viscosity of ILs in a given series of related ILs, these generalities are not applicable to other combinations of cation and anion. One of the largest problems plaguing viscosity measurements of ILs is the presence of variable amounts of contaminants in an IL. Small amounts of impurities are known to dramatically influence the viscosity of a given IL [5, 25, 26]. Even with considerable purification efforts, small amounts of impurities are normally present in an IL. Thus, for example, although the IL glass transition temperature is known to be related to the IL viscosity, the results from

various studies have shown that generalities in this relationship between different series do not exist [2].

The majority of ILs have a density that is higher than that of water [2]. Generally, longer alkyl chains on the IL result in a decrease in its density. Though impurities strongly affect many physical properties, the density is the least affected by their presence [27]. Since the densities of ILs are not particularly sensitive to temperature variations, density is one of the more reliable properties that can be measured.

Most of the measured IL polarities fall within the range comparable to those of the short- to medium-chain alcohols [9]. The size of the alkyl chain greatly influences the IL polarity. A longer side alkyl chain in the cation induces hydrophobicity making the IL insoluble in water [2, 19]. Various combinations of cations and anions lead to ILs with different polarities. For example, the choice of anion allows us to change the water miscibility of an IL as illustrated in 0 [18].

The conductivity of an IL is a very important consideration in its pre-selection for an electrochemical application. The conductivity value of an IL gives an insight into the mobility of ions in the IL. In general ILs have reasonably good conductivities compared to the best alternative non-aqueous solvent/electrolyte systems. However their conductivities are significantly lower than those of concentrated salt aqueous electrolytes [23]. This lower conductivity is mainly attributed to the high degree of ion pairing and/or ion aggregation in an IL (compared to a dissociated salt in water) that results in a reduction in the number of free ions or available charge carriers [23]. As well large cations also tend to have reduced mobility. There is no established relationship between

the anion size and conductivity in ILs. Some ILs containing large anions have higher conductivities than the conductivities of related ILs with smaller anions [23]. Again, this has been attributed to different amounts of strong ion pairing that may occur in the different ILs [6, 28]. As for viscosity, the presence of contaminants and impurities in an IL can severely affect its conductivity, particularly by decreasing the viscosity of the IL and increasing the mobility of ions through the IL [23].

Several groups have used theoretical calculations and simulations as an approach to understand and predict the different properties exhibited by ILs [6, 29-37]. These studies provided insights on the molecular structures and bulk phase property relationships, but can be limited in scope; some relationships only apply to ILs with the same cation with different anions or vice versa. The molecular properties determined by some DFT calculations of a single IL molecule have been correlated to transport properties of the IL, such as viscosity and conductivity. This is both interesting and a bit puzzling, because transport properties tend to be greatly influenced by the intermolecular interaction with the other IL molecules and not just on the interionic forces associated with a single pair. However, we would like to take advantage of such correlations because the DFT calculations are much less expensive than large-scale molecular dynamics (MD) calculations that would involve multiple IL molecules.

2.1.3 Phosphonium-based ionic liquids

While nitrogen-based ILs are the most frequent type of IL that have been studied (seven of the nine most common cation structures are nitrogen-based, 0), less well studied phosphonium-based ILs have progressively become exciting prospects for use in

industrial applications due to their high thermodynamic stability, lower toxicity (compared to imidazolium ILs), higher thermal stability and cost-effectiveness [20, 38, 39].

Because they are less expensive to manufacture, phosphonium ILs are already available on a multi-ton commercial scale [20, 40] and this is an additional reason why they are being considered for industrial processes [20]. Aside from this, phosphonium ILs possess many physical properties making them attractive. The phosphonium cation has a number of features which differentiate it from other commonly used groups of cations. For example, the phosphonium cation has four locations for ligand substitution and this increases the number of possible combinations of alkyl and aryl side chains on the cation (compared to nitrogen-based cations). This gives phosphonium ILs a greater range of “tunability” [39]. Another advantage of phosphonium ILs compared to the common imidazolium ILs is that they lack weakly acidic ring protons. These acidic protons and cyclic rings are able to interact with solutes through aromatic bonding or hydrogen bonding and make the ILs less inert. This can be an issue for many applications [20, 39, 40]. Phosphonium ILs have higher viscosities compared to nitrogen-based ILs at room temperature. This is probably due to the typically larger cation that has been used with mostly alkyl substituted cation chains where van der Waal’s interaction between the alkyl chains is significant. The electrochemical potential windows in phosphonium ILs are wider than in imidazolium ILs [41]. Although both phosphonium and ammonium ILs can decompose by internal displacement at high temperatures, phosphonium ILs are generally more stable in this respect [20]. There are a number of quaternary phosphonium ILs that have been synthesized and nearly all are

liquid at well below room temperature and are stable up to 400 °C in some cases [39].

This offers greater practicality and scope than the nitrogen-based ILs.

2.2 RADIATION BACKGROUND

2.2.1 Ionizing Radiation

The electromagnetic spectrum of light has two major divisions. These are the non-ionizing and ionizing radiation. The former type of radiation has longer wavelength and has insufficient energy to remove electrons (induce ionization). Examples of this type of radiation are the radiofrequency waves, infrared, microwaves and visible light. Ionizing radiation has a shorter wavelength and the greater photon energy is sufficient to break chemical bonds and eject tightly bound electrons to create charged particles or ions. The most common examples of these are the α -particles, β -particles and γ -rays [42]. These high-energy particles are typically in the range of 10 keV to 10 MeV [43]. While ultraviolet light meets this criteria, the most important sources of ionizing radiation come from naturally occurring radioactive materials or from artificial sources of radiation, such as in X-ray tubes and particle accelerators. This radiation has photon energies which are orders of magnitude greater than the ionization energy of an atom or molecule and is able to create multiple ions.

An α -particle is a high energy (or fast) helium nucleus ${}^4_2\text{He}^{2+}$ and a β -particle is a fast moving electron and both particles can be emitted from decaying radionuclides [43]. The α -particles emitted from radionuclide decay have a discrete energy that is characteristic of the radionuclide. The energy of a β -particle likewise depends on the

decay of a particular radioactive isotope. However, instead of having a discrete energy, the energy of β -particles ranges from near zero up to a maximum energy, which is characteristic of the radionuclide. Particle emission during radioactive decay is also accompanied by the emission of X-rays and γ -rays. The characteristic energy of a γ -photon emitted from a decaying radionuclide is also discrete and there can be multiple photons with different energies. As an example, the β -decay of cobalt-60 emits γ -rays that have energies of 1.332 MeV and 1.173 MeV [43].

2.2.2 Radiation Interaction to Matter

The high-energy charged particles and photons emitted during radioactive decay are also termed ionizing radiation because of their ability to ionize atoms and molecules. When passing through a medium, a fast moving particle continuously loses energy through a series of inelastic collisions with electrons in the interacting medium located along the radiation path. The rate of energy transfer per penetration length through a medium is referred to as the linear energy transfer (LET) rate. In a given medium, the LET is highest for α -particles, followed by β -particles, and it is the lowest for γ -photons [43]. Accordingly, penetration depths of 20 – 25 μm are typical for α -particles, 0.5 – 1.0 cm for β -particles, and tens of cm for γ -rays in water at room temperature [42, 43], as shown in 0. Because of its large collision cross section with electrons (or short mean free path), the heavy charged α -particle loses its energy completely within a short distance. This results in a very dense collection of excited and ionized particles along a short radiation track, 0. Due to a much lower particle mass and smaller size, the inelastic mean free path of a β -particle is much shorter and its penetration range is much deeper.

Gamma rays have energies on the order of 40 keV to 10 MeV and lose their energy by Compton scattering and the photoelectric effect. Compton scattering is the process where a γ -photon interacts with an electron attached to an atom or molecule, causing the electron to accelerate while the photon is deflected with reduced energy [42, 43]. The electron ejected from a high-energy Compton event also has high energy and it then acts as a β -particle and has ionizing collisions. The initial γ -photon generates an electron cascade until it loses all of its energy. Hence both β - and γ -radiation induce similar chemical effects in the interacting medium per unit of absorbed radiation energy [43]. For photons with energies below about 60 keV, the photoelectric effect becomes the most important process [42].

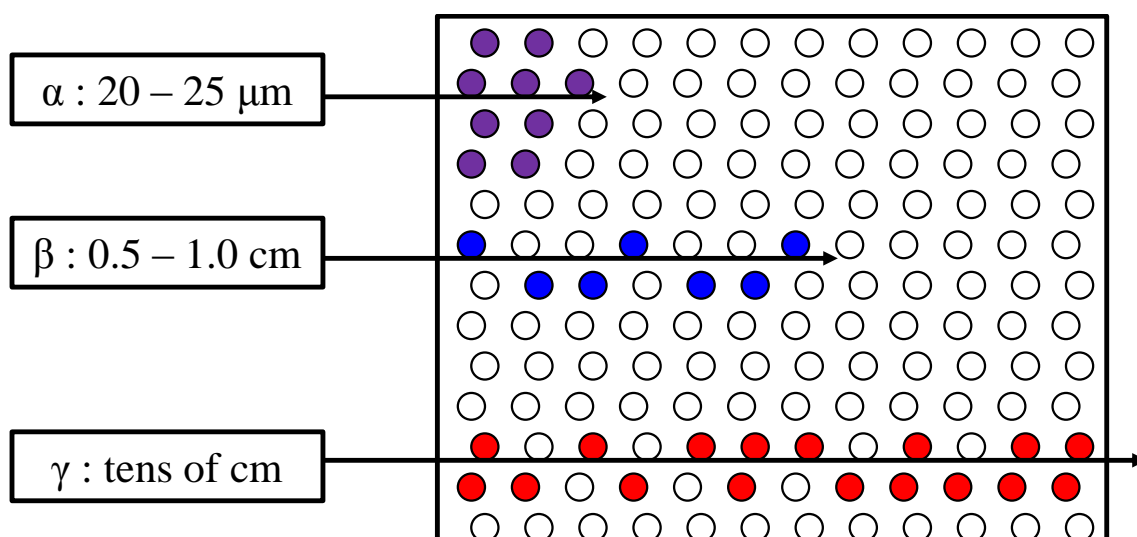


Figure 2.2 Penetration depth of ionizing radiation and density of excited species in water.

The amount of energy absorbed by the medium, rather than radiation source strength is the controlling parameter in determining the consequences of exposure to radiation. The absorbed dose (or the total energy absorbed) by the interacting matter is expressed in units of Gray (Gy), where $1 \text{ Gy} = 1 \text{ J}\cdot\text{kg}^{-1}$. The rate of energy transfer from radiation to the medium and the radiation source strength dictates the absorbed dose rate. The rate of energy transfer from radiation to matter depends on the type of radiation as well as the density of electrons (or mass) of the interacting matter as described above.

2.2.3 Radiation-induced chemistry

Radiation chemistry examines the chemical effects produced in a system that is exposed to ionizing radiation. Radiation chemistry differs from photochemistry. In photochemistry, atoms or molecules are exposed to relatively low energy electromagnetic radiation such as visible light and ultraviolet (UV). These low energy sources (in a several eV range) provide sufficient energy to induce vibrational or electronic excitations in target molecules and may break bonds (for the higher energy sources). This excitation happens in a one-to-one manner; a single photon interacts with a single molecule and the frequency of the radiation that can be absorbed is highly specific to a particular atom or molecular group. Due to the high specificity of the interaction, photochemistry can be described as a solute-oriented process in which the bulk solution in which the target species resides remains unaffected by the presence of the radiation [43].

In contrast, radiation chemistry involves high energy ionizing radiation (in the keV to MeV range) that excites or ionizes a large number of molecules randomly distributed along a radiation track. This means that all molecules present in the path are

equally likely to interact with the radiation. For a dilute species located in a solution, this means that the bulk solution molecules are most affected and the dilute species cannot be specifically targeted. Hence, radiation chemistry can be described as a solvent-oriented process [43].

2.2.3.1 Water Radiolysis

When exposed to ionizing radiation, water decomposes to form a range of chemically reactive species. The initial interaction of a radiation particle or photon with water produces an electron and a positively charged water ion or an excited water molecule. Each radiation particle (or photon) can undergo many such interactions before it loses its energy. The secondary electrons ejected from water molecules also have high kinetic energies (tens of eV) and can ionize or excite one or two other water molecules. Thus, each collision between a radiation particle/photon with water creates 2-3 ions/excited molecules referred to as a spur (0). As the spurs expand, the species in the spur recombine, undergo ion-molecule reactions to form radicals or molecular products, or solvate, as illustrated in 0 [43-46]. How fast the initial radiolysis products are thermalized before these reactions take place is very important in determining how effectively the absorbed radiation energy is used in producing chemical decomposition products versus heat.

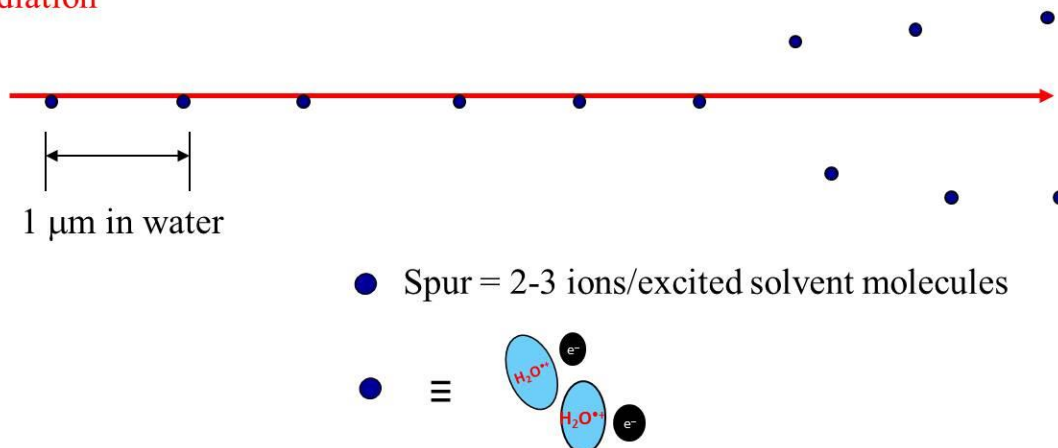
γ -radiation

Figure 2.3 The radiation track resulting from a γ -photon [43].

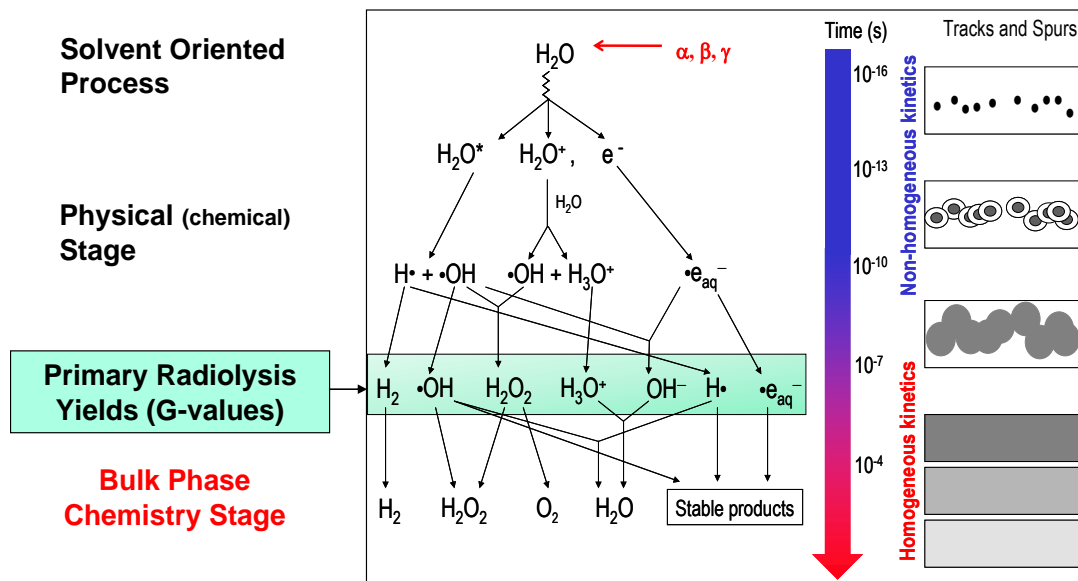
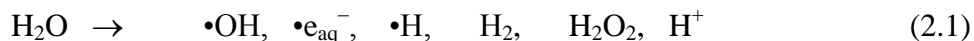


Figure 2.4 Schematic of the initial reactions and the approximate time scales that occur in water to generate the primary radiolysis products during absorption of ionizing radiation [44].

The distribution of the water radiolysis products reaches homogeneity along the radiation track within 10^{-9} to 10^{-6} s. The chemical species formed at the end of this time scale are referred to as primary radiolysis products and their yields are expressed in G-values [44, 47]. The G-value is defined as the number of molecules produced per unit of absorbed energy and has standard units of $\mu\text{mol}\cdot\text{J}^{-1}$. The G-values depend strongly on the type of radiation (α -, β -, γ -, etc.) and solvent properties. For gamma-radiolysis of water, the primary radiolysis products and corresponding G-values at 25 °C ($\mu\text{mol}\cdot\text{J}^{-1}$) are given below:



G-values: -0.42 $0.27, 0.26, 0.06, 0.045, 0.07, 0.26$

The primary (or homogeneous) radiolysis yields are achieved in a very short time scale ($< \mu\text{s}$) when solute concentration is less than 10^{-2} M. Since chemical reactions in condensed phases (liquid or solid) are slow we can take the yields multiplied by the radiation dose rate ($\text{J}/\text{kg H}_2\text{O}/\text{s} = \text{Gy}/\text{s}$) as the initial production rate of these species. Homogeneous aqueous phase chemical kinetics in a radiation field is concerned with the reactions of these primary radiolysis products with each other, with water molecules, and, if present, with solute species. Detailed kinetic analyses of the events occurring on a time scales less than μs are not necessary to follow the chemical kinetics occurring later in the aqueous phase or condensed phase.

2.2.3.2 Ionic Liquid/Organic Liquid Radiolysis

Interaction of ionizing radiation with ionic liquids or an organic liquid follows a process similar to that which occurs in water radiolysis. The initial interaction of a molecule with radiation induces ionization and excitation of the solvent molecule. However, the probability of the charged or excited species that are initially created in the spur along the radiation track escaping geminate recombination to become free ions or free radicals is lower in a low dielectric medium like an organic solvent or IL. The reason for this is that the escape probability, P_{esc} , depends on the ratio of the distance created between the ion and an electron, (r), and the Onsager radius (r_c), which is the distance at which the energy of the Coulomb interaction between the ions in a dielectric continuum becomes equal to the thermal energy (k_bT) and the dielectric constant (ϵ_r) of the solvent medium:

$$P_{esc} = \exp\left(\frac{r}{r_c}\right) \quad (2.2)$$

$$r_c = \frac{e^2}{4\pi\epsilon_r\epsilon_o k_b T} \quad (2.3)$$

where e is the charge of electron or counter ion, ϵ_o is the permittivity in the vacuum, k_b is the Boltzmann constant and T is the temperature (K). These equations state that the absorbed radiation energy in a liquid with a lower dielectric medium is less effective in producing chemical decomposition products versus kinetic energy (i.e., heat).

Ionic liquids have relatively low dielectric constants, typically < 15 , that are comparable to those of organic solvents [48, 49]. In comparison, water has a high

dielectric constant (80.1 at room temperature [48]). This explains the low radiolytic decomposition yields of ILs and organic solvents [48-51].

2.3 CORROSION BACKGROUND

Aqueous corrosion is an electrochemical process involving oxidation of a metal species, M , coupled with reduction of an aqueous species, Ox :



where Ox represents the oxidant and Red the reduced form of the oxidant. Since the metal and water phases are conductive, the two half-reactions do not need to occur at the same site, but corrosion does involve an interfacial charge transfer.

The driving force for an electrochemical reaction is a difference in the electrochemical potentials of the two interacting phases. The electrochemical potential of each component in the reaction can be represented by the Nernst redox potential for each half-reaction:

$$E_{EQ} = E^{\circ} - \left(\frac{RT}{nF} \right) \cdot \ln \left(\frac{[red]}{[ox]} \right) \quad (2.6)$$

where E_{EQ} is the equilibrium potential, E° is the standard electrode potential, R is the gas constant ($8.3145 \text{ J}\cdot\text{K}^{-1}\cdot\text{mol}^{-1}$), T the temperature in Kelvin, n the number of electrons transferred in the reaction, and F the Faraday constant ($96\,485 \text{ C}\cdot\text{mol}^{-1}$).

The oxidized metal of reaction (2.4) either combines with O^{2-} or OH^- to form a solid oxide layer or it dissolves into the water. The rate of metal dissolution depends on the solubility of the oxide(s) that can form on the metal at the water interface. This solubility is a function of pH and temperature. With an oxide layer on the metal, the rate of metal oxidation and the type of oxide that can be formed depend on the electrochemical potential differences that exist at both the metal/metal oxide interface and the metal oxide/water interface, and the potential gradient through the oxide layer. For these reasons the type of oxide that forms on the surface can be important in controlling corrosion behaviour.

Aqueous corrosion of carbon steel has been studied extensively [52-56]. Studies on the electrochemical corrosion in non-aqueous electrolyte media are very rare, primarily due to a lack of appropriate electrolytes other than alcohol/water mixtures, and have been limited to studies of molten salts at high temperature [57-60]. However, recent development of room temperature ILs with wide electrochemical windows has provided non-aqueous electrolytes that can be used for electrochemical processes at low temperatures. Studies on the electrochemical processes in IL electrolytes are still in an infant stage and, furthermore, are limited to those occurring on inert surfaces. Studies on electrochemical corrosion of electrodes or alloys in contact with ILs are very rare. To date, only studies on carbon steel corrosion in imidazolium ILs have been reported [61, 62]. For example, Uerdingen et al. studied the corrosion resistance of carbon steel in imidazolium ILs with different anions in water-free and water diluted ILs [61]. They reported that carbon steel may undergo severe corrosion in diluted IL media and that the corrosion is dependent on the IL composition.

Gamma-irradiation can decompose the IL molecules, albeit at a slow rate. Thus, the radiolytic decomposition products of ILs may influence the electrolytic properties of the IL solvent and the corrosion of metals in the degraded IL.

2.4 IONIC LIQUIDS, RADIATION AND CORROSION

The stability of ionic liquids and their extraction capabilities make them an attractive alternative for use in radioactive separation processes in the nuclear industry (such as spent fuel reprocessing). Currently such separations are done using organic phases such as kerosene and dodecane (e.g., in the PUREX process for spent nuclear fuel) [63]. Prior to use in nuclear applications, the radiation stability of the ionic liquids must be understood. Ionic liquids when exposed to radiation may undergo radiolytic decomposition that may alter their physical and chemical properties. Radiolytic decomposition products may be chemically reactive or redox active species which can affect interfacial charge transfer reactions. There are few studies on the radiation stability of ILs with various cation and anion combinations and most work has used pulse radiolysis and has been confined to ammonium and imidazolium-based ILs. These studies have reported a relatively high radiation resistance of ILs compared to water or organic solvents. This resistance is due to the lower probability of 'dry' electrons escaping geminate or recombination reactions before they are solvated in an IL [3, 48, 50]. Gamma-radiation stability studies of some ILs are also available, but they too are confined to imidazolium-based ILs [64-69]. Phosphonium-based ILs have not been studied as well. Previous work performed by our research group with tetradecyl(trihexyl)phosphonium bis(trifluoromethylsulfonyl) imide [P₁₄₆₆₆] [NTf₂] ionic

liquid interfaced with water has shown that micelles naturally form in this system due to charge transfer across the phase interface. This effect was accelerated by exposure to γ -radiation due to the generation of small quantities of radiolytic decomposition products that increase the rate of charge transport across the phase interface [50].

The interfacial reactions of an IL with a metal surface are not well studied and there are no reported studies on the effect of γ -radiation on such reactions. There are a few studies on the interaction of ILs with metal surfaces for applications such as lubricants and corrosion inhibitors [70]. These studies have reported only an enhancement in the tribological properties of the IL and have not addressed the chemistry happening at the ionic liquid-metal interface. They do not address how a change in electrolytic properties of an IL may influence interfacial charge transfer. There is one group who studied carbon steel corrosion in ILs with altered electrolytic properties (in water-free and water diluted IL); they only focused on the corrosion weight loss [61]. There is considerable scope for additional work to determine the efficacy of IL as a lubricant or corrosion inhibitor and to fully understand the corrosion behaviour of ILs in high radiation environments.

2.5 REFERENCES

- [1] E.W. Castner, J.F. Wishart, *J. Chem. Phys.*, 132 (2010) 120901.
- [2] K.N. Marsh, J.A. Boxall, R. Lichtenthaler, *Fluid Phase Equilib.*, 219 (2004) 93.
- [3] R.D. Rogers, K.R. Seddon, Editors, *Ionic Liquids as Green Solvents: Progress and Prospects*, ACS, Washington, DC (2003).
- [4] T. Welton, *Chem. Rev.*, 99 (1999) 2071.
- [5] J.D. Holbrey, R.D. Rogers, *Physicochemical Properties of Ionic Liquids: Melting Points and Phase Diagrams*, in: *Ionic Liquids in Synthesis*, P. Wasserscheid, T. Welton, Editors, Wiley-VCH Verlag, Weinheim, Germany (2008).
- [6] R.P. Morco, A.Y. Musa, J.C. Wren, *Solid State Ionics*, 258 (2014) 74.

- [7] A. Heintz, *J. Chem. Thermodyn.*, 37 (2005) 525.
- [8] H. Zhao, S.Q. Xia, P.S. Ma, *J. Chem. Technol. Biotechnol.*, 80 (2005) 1089.
- [9] P. Wasserscheid, T. Welton, *Ionic Liquids in Synthesis*, Wiley-VCH Verlag, Weinheim, Germany (2008).
- [10] P.J. Dyson, T.J. Geldbach, *Metal Catalyzed Reactions in Ionic Liquids*, Springer, New York (2006).
- [11] C.S. Brazel, R.D. Rogers, Editors, *Ionic Liquids in Polymer Systems*, Oxford University Press, New York (2005).
- [12] X. Han, D.W. Armstrong, *Accounts Chem. Res.*, 40 (2007) 1079.
- [13] H. Ohno, *Electrochemical Aspects of Ionic Liquids*, Wiley-Interscience, New York (2005).
- [14] M. Maase, *Industrial Applications of Ionic Liquids*, in: *Ionic Liquids in Synthesis*, P. Wasserscheid, T. Welton, Editors, Wiley-VCH Verlag, Weinheim, Germany (2008).
- [15] J.F. Wishart, *Energy Environ. Sci.*, 2 (2009) 956.
- [16] D.R. MacFarlane, N. Tachikawa, M. Forsyth, J.M. Pringle, P.C. Howlett, G.D. Elliott, J.H. Davis, M. Watanabe, P. Simon, C.A. Angell, *Energy Environ. Sci.*, 7 (2014) 232.
- [17] S. Keskin, D. Kayrak-Talay, U. Akman, Ö. Hortaçsu, *J. Supercrit. Fluid.*, 43 (2007) 150.
- [18] N.V. Plechkova, K.R. Seddon, *Chem. Soc. Rev.*, 37 (2008) 123.
- [19] J.F. Brennecke, E.J. Maginn, *AIChE J.*, 47 (2001) 2384.
- [20] K.J. Fraser, D.R. MacFarlane, *Aust. J. Chem.*, 62 (2009) 309.
- [21] P. Bonhote, A.P. Dias, N. Papageorgiou, K. Kalyanasundaram, M. Gratzel, *Inorg. Chem.*, 35 (1996) 1168.
- [22] R. Hagiwara, Y. Ito, *J. Fluorine Chem.*, 105 (2000) 221.
- [23] P.C. Trulove, R.A. Mantz, *Electrochemical Properties of Ionic Liquids*, in: *Ionic Liquids in Synthesis*, P. Wasserscheid, T. Welton, Editors, Wiley-VCH Verlag, Weinheim, Germany (2008).
- [24] D.R. Lide, *CRC Handbook of Chemistry and Physics*, CRC Press, Boca Raton, FL (2011).
- [25] K.R. Seddon, A. Stark, M.J. Torres, *Pure Appl. Chem.*, 72 (2000) 2275.
- [26] J.A. Widegren, A. Laesecke, J.W. Magee, *Chem. Commun.*, 12 (2005) 1610.
- [27] L. Berthon, S.I. Nikitenko, I. Bisel, C. Berthon, M. Faucon, B. Saucerotte, N. Zorz, P. Moisy, *Dalton Trans.*, 21 (2006) 2526.
- [28] K.J. Fraser, E.I. Izgorodina, M. Forsyth, J.L. Scott, D.R. MacFarlane, *Chem. Commun.*, 37 (2007) 3817.
- [29] D.R. MacFarlane, K.R. Seddon, *Aust. J. Chem.*, 60 (2007) 3.
- [30] S. Tsuzuki, W. Shinoda, H. Saito, M. Mikami, H. Tokuda, M. Watanabe, *J. Phys. Chem. B*, 113 (2009) 10641.
- [31] P.A. Hunt, *J. Phys. Chem. B*, 111 (2007) 4844.
- [32] P.A. Hunt, B. Kirchner, T. Welton, *Chem. Eur. J.*, 12 (2006) 6762.
- [33] X. Liu, G. Zhou, S. Zhang, G. Yu, *Mol. Simulat.*, 36 (2010) 79.
- [34] W. Li, X. Wu, C. Qi, H. Rong, L. Gong, *J. Mol. Struct.-Theochem*, 942 (2010) 19.
- [35] R. Lü, H. Tangbo, Z. Cao, *J. Nat. Gas Chem.*, 16 (2007) 70.

- [36] R. Lü, S. Wang, Y. Lu, *Chem. Phys. Lett.*, 505 (2011) 87.
- [37] C.E.R. Prado, L.C.G. Freitas, *J. Mol. Struct.-Theochem*, 847 (2007) 93.
- [38] C.M.S.S. Neves, P.J. Carvalho, M.G. Freire, J.A.P. Coutinho, *J. Chem. Thermodyn.*, 43 (2011) 948.
- [39] R.E. Del Sesto, C. Corley, A. Robertson, J.S. Wilkes, *J. Organomet. Chem.*, 690 (2005) 2536.
- [40] C.J. Bradaric, A. Downard, C. Kennedy, A.J. Robertson, Y. Zhou, *Green Chem.*, 5 (2003) 143.
- [41] A.M. O'Mahony, D.S. Silvester, L. Aldous, C. Hardacre, R.G. Compton, *J. Chem. Eng. Data*, 53 (2008) 2884.
- [42] J.H. O'Donnell, D.F. Sangster, *Principles of Radiation Chemistry*, American Elsevier Publishing Company, New York, NY (1970).
- [43] J.W.T. Spinks, R.J. Woods, *An Introduction to Radiation Chemistry*, Wiley, New York (1990).
- [44] J.C. Wren, *Steady-State Radiolysis: Effects of Dissolved Additives*, in: ACS Symposium Series: Nuclear Energy and the Environment, C.M. Wai, B.J. Mincher, Editors, Oxford University Press, Washington, DC (2010), p.271-295.
- [45] P.A. Yakabuskie, J.M. Joseph, P. Keech, G.A. Botton, D. Guzonas, J.C. Wren, *Phys. Chem. Chem. Phys.*, 13 (2011) 7167.
- [46] A.O. Allen, *The Radiation Chemistry of Water and Aqueous Solutions*, Van Nostrand, New York (1961).
- [47] J.C. Wren, J.M. Ball, *Radiat. Phys. Chem.*, 60 (2001) 577.
- [48] J. Grodkowski, P. Neta, J.F. Wishart, *J. Phys. Chem. A*, 107 (2003) 9794.
- [49] J.F. Wishart, *Radiation Chemistry of Ionic Liquids: Reactivity of Primary Species*, in: *Ionic Liquids as Green Solvents: Progress and Prospects*, R.D. Rogers, K.R. Seddon, Editors, ACS, Washington, DC (2003).
- [50] S.E. Howett, J.M. Joseph, J.J. Noël, J.C. Wren, *J. Colloid Interface Sci.*, 361 (2011) 338.
- [51] T. Singh, A. Kumar, *J. Phys. Chem. B*, 112 (2008) 12968.
- [52] K. Daub, X. Zhang, J.J. Noel, J.C. Wren, *Electrochim. Acta*, 55 (2010) 2767.
- [53] C.T. Lee, M.S. Odziemkowski, D.W. Shoesmith, *J. Electrochem. Soc.*, 153 (2006) B33.
- [54] L.J. Oblonsky, S. Virtanen, V. Schroeder, T.M. Devine, *J. Electrochem. Soc.*, 144 (1997) 1604.
- [55] S. Virtanen, P. Schmuki, A.J. Davenport, C.M. Vitus, *J. Electrochem. Soc.*, 144 (1997) 198.
- [56] K. Yazdanfar, X. Zhang, P.G. Keech, D.W. Shoesmith, J.C. Wren, *Corros. Sci.*, 52 (2010) 1297.
- [57] A. Nishikata, S. Haruyama, *Corrosion*, 42 (1986) 578.
- [58] L.C. Olson, J.W. Ambrosek, K. Sridharan, M.H. Anderson, T.R. Allen, *J. Fluorine Chem.*, 130 (2009) 67.
- [59] M. Kondo, T. Nagasaka, Q. Xu, T. Muroga, A. Sagara, N. Noda, D. Ninomiya, M. Nagura, A. Suzuki, T. Terai, N. Fujii, *Fusion Eng. Des.*, 84 (2009) 1081.
- [60] S.H. Cho, J.M. Hur, C.S. Seo, S.W. Park, *J. Alloy. Compd.*, 452 (2008) 11.
- [61] M. Uerdingen, C. Treber, M. Balsler, G. Schmitt, C. Werner, *Green Chem.*, 7 (2005) 321.

- [62] A.B. Tolstoguzov, U. Bardi, S.P. Chenakin, B. Russ. Acad. Sci. Phys., 72 (2008) 605.
- [63] S.H. Ha, R.N. Menchavez, Y.-M. Koo, Korean J. Chem. Eng., 27 (2010) 1360.
- [64] M.Y. Qi, G.Z. Wu, Q.M. Li, Y.S. Luo, Radiat. Phys. Chem., 77 (2008) 877.
- [65] C. Jagadeeswara Rao, K.A. Venkatesan, B.V.R. Tata, K. Nagarajan, T.G. Srinivasan, P.R. Vasudeva Rao, Radiat. Phys. Chem., 80 (2011) 643.
- [66] N.J. Bridges, A.E. Visser, M.J. Williamson, J.I. Mickalonis, T.M. Adams, Radiochim. Acta, 98 (2010) 243.
- [67] M.Y. Qi, G.Z. Wu, S.M. Chen, Y.D. Liu, Radiat. Res., 167 (2007) 508.
- [68] L.Y. Yuan, J. Peng, L. Xu, M.L. Zhai, J.Q. Li, G.S. Wei, Radiat. Phys. Chem., 78 (2009) 1133.
- [69] L.Y. Yuan, J. Peng, M.L. Zhai, J.Q. Li, G.S. Wei, Radiat. Phys. Chem., 78 (2009) 737.
- [70] N.V. Likhanova, O. Olivares-Xometl, D. Guzman-Lucero, M.A. Dominguez-Aguilar, N. Nava, M. Corrales-Luna, M.C. Mendoza, Int. J. Electrochem. Sc., 6 (2011) 4514.

Chapter 3

Experimental Principles and Details

In this chapter, the principles of the experimental techniques used in this thesis are briefly reviewed. Experimental procedures that are common to all experiments are described. As necessary, more detailed information on sample preparation and experimental parameters is provided in the experimental sections of the subsequent chapters.

3.1 SAMPLE ANALYSIS TECHNIQUES

3.1.1 Gas Chromatography-Mass Spectrometry

The gas phase that lies above the ionic liquid sample in a test vial is referred to as headspace gas. This gas can contain volatile species that have partitioned from the ionic liquid phase to the gas phase. Gas chromatography-mass spectrometry (GC/MS) was used to study the headspace gas above the ionic liquid (IL). The technique is particularly useful for determining airborne radiolytic decomposition products. Gas chromatography-mass spectroscopy is a combination of two techniques for analyzing gases. Gas chromatography separates the components of a mixture and mass spectroscopy characterizes each of the isolated components. By combining the two techniques, both qualitative and quantitative evaluation of a mixture of chemicals can be made. In common with all chromatography techniques, separation is achieved by differential partitioning between the mobile (gas) phase and the stationary phase on the walls of the

gas chromatograph column. When a gas sample is introduced into a mobile phase (also called a carrier gas, usually an inert gas such as helium or nitrogen gas) the carrier gas drives the sample along a column containing a stationary phase. The column is usually made of a glass or steel tube. The stationary phase is a chemical that has selective affinity to attract components in a sample mixture. As the mixture of compounds passes through the column, it interacts with the stationary phase at different rates depending on a component molecule's affinity. The rate of separation is also controlled by applying a temperature gradient in the column or by changing the pressure and flow rate of the carrier gas [1]. The output of a common gas chromatograph contains peaks that represent species eluting at a specific time as presented in 0.

As the individual molecules leave the GC column they enter the mass spectrometer detector. Here they are ionized and broken apart into fragments by a stream of electrons. The fragments are charged ions with a characteristic mass with a mass to charge ratio of m/z (where m is the molecular weight of the fragment and z is its total positive charge). Most of the fragments have only +1 charge and their m/z ratios then correspond to their molecular weights. The ionized fragments are accelerated into a quadrupole where the fragments are selectively directed onto a detector slit according to their m/z ratio. The output of the mass spectrometer is a graph composed of the fragment weights and their corresponding abundancies (insets in 0).

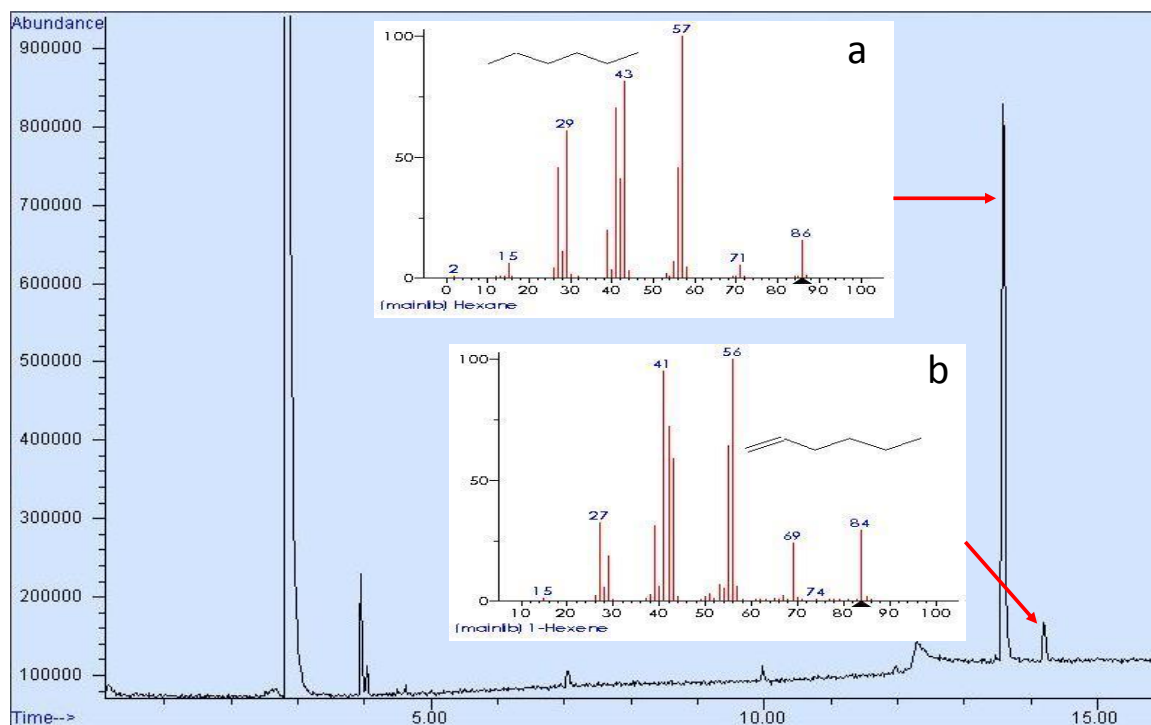


Figure 3.1 Gas chromatogram of the headspace gas from a test with a pure IL irradiated for 192 hours. Insets are the mass spectra from the a) hexane and b) hexene peaks.

3.1.2 UV-Visible Spectrophotometry

Ultraviolet and visible (UV-Vis) absorption spectroscopy is the measurement of the attenuation of a beam of light after passage through a sample or after reflection from a sample surface. This absorption spectroscopy uses electromagnetic radiation between 200 nm and 800 nm and is divided into the ultraviolet (UV, 200-400 nm) and visible (Vis, 400-800 nm) regions.

A UV-Vis spectrophotometer consists of a light source, a sample cell, and a diode array detector which allows the instrument to simultaneously detect the absorbance at all source wavelengths, θ . The intensity of a beam of light is measured before (incident) and

after passing through a transparent sample cell (cuvette) containing the analyte (transmitted). The amount of light absorbed is the difference between the intensities of the incident radiation (I_o) and the transmitted radiation (I) and is expressed as either transmittance or absorbance [2]. Transmittance usually is described in terms of a fraction of 1 or as a percentage and is defined as:

$$\mathbf{T} = \frac{I}{I_o} \text{ or } \% \mathbf{T} = \left(\frac{I}{I_o}\right) \times \mathbf{100} \quad (3.1)$$

Absorbance is the negative logarithm of the transmittance,

$$\mathbf{A} = -\mathbf{log} \frac{I}{I_o} \quad (3.2)$$

Most applications use absorbance values since the relationship between absorbance and both analyte concentration and cell path length is normally linear. The concentration of an absorbing species is quantitatively determined using the Beer-Lambert law which gives the relationship between absorbance and concentration.

$$\mathbf{A} = \mathbf{log} \frac{I_o}{I} = \boldsymbol{\varepsilon} \mathbf{c} \mathbf{l} \quad (3.3)$$

where ε is the molar absorptivity or extinction coefficient of the analyte, expressed in units of $\text{L}\cdot\text{mol}^{-1}\cdot\text{cm}^{-1}$, l is the optical path length of the cuvette (usually in centimeters), and c is the concentration of the sample, expressed as $\text{mol}\cdot\text{L}^{-1}$. The amount of light absorbed is proportional to the number of absorbing molecules through which the light passes [2].

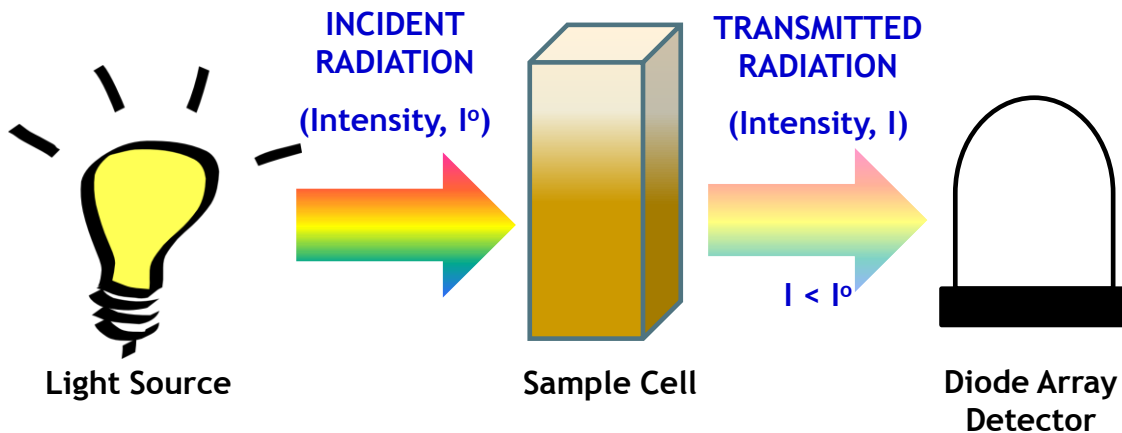


Figure 3.2 Illustration of a diode array UV-Vis spectrophotometer.

3.1.3 Raman Spectroscopy

Raman spectroscopy is an analytical method used to probe the chemical composition of materials that are Raman active. The Raman spectrometer instrumentation consists of a narrow wavelength laser light source with a frequency in the visible spectrum, a sample illumination and scattered light collection system, and a light detection system. Raman spectroscopy detects induced changes in the polarizability of the electron cloud around a molecule after interaction with light [3, 4].

When a sample is irradiated by an intense laser beam in the UV-visible region two types of scattered radiation are produced. These are Rayleigh scattering (elastic), which dominates and has the same frequency (ν_i) as the incident beam, and Raman scattering (inelastic) which is very weak (approximately 1 in 10^7 incident photons) and has frequencies

$$\nu = \nu_i \pm \nu_{vib} \quad (3.4)$$

where ν_{vib} is one of the vibrational frequencies of an analyte molecule. In Raman spectroscopy the vibrational frequency is measured as a shift from the incident beam frequency that occurs when a molecule absorbs the incident photon to form a virtual high electronic energy state and then immediately relaxes to a lower level energy state with a different vibrational energy state. The scattering of photons with a lower energy than the energy of the incident photon ($\nu_i - \nu_{vib}$) is called Stokes scattering as schematically shown in 0. A frequency shift $\nu_i + \nu_{vib}$ is observed when the molecule initially in a high vibrational energy state is excited and relaxes to a lower vibrational energy state. This results in scattered photons with a higher frequency than that of the incident light and is called anti-Stokes scattering. Anti-Stokes scattering has a lower intensity (0) because fewer molecules are initially in excited vibration states than in the ground state (for molecules in thermal equilibrium where the Boltzmann distribution for population of vibration energy states will apply).

Vibrational spectra of a molecule correspond to stretching and bending motions involving the various bonds in the molecules. Since the vibrational energy levels are characteristic of the bonds between atoms, they are chemical compound specific and can be associated with specific wavelength shifts [5]. A measurement of these shifts is a means of identification of scattering compounds. Raman spectroscopy is a particularly useful tool because spectra can be measured in an aqueous phase without interference since water is not Raman active. A Raman spectrum is normally reported as Raman shifts in terms of wavenumbers ($1/\lambda$) in units of cm^{-1} .

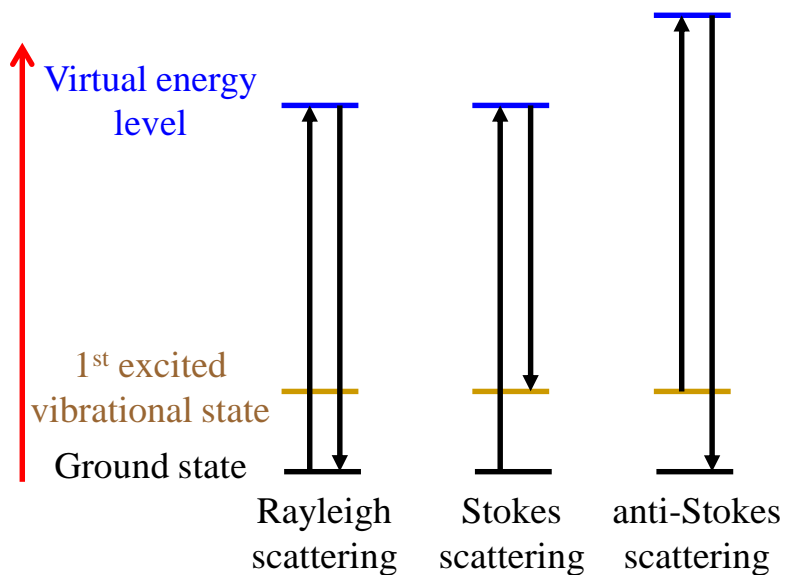


Figure 3.3 Illustration showing Rayleigh scattering, Stokes (Raman) scattering, and Anti-Stokes (Raman) scattering.

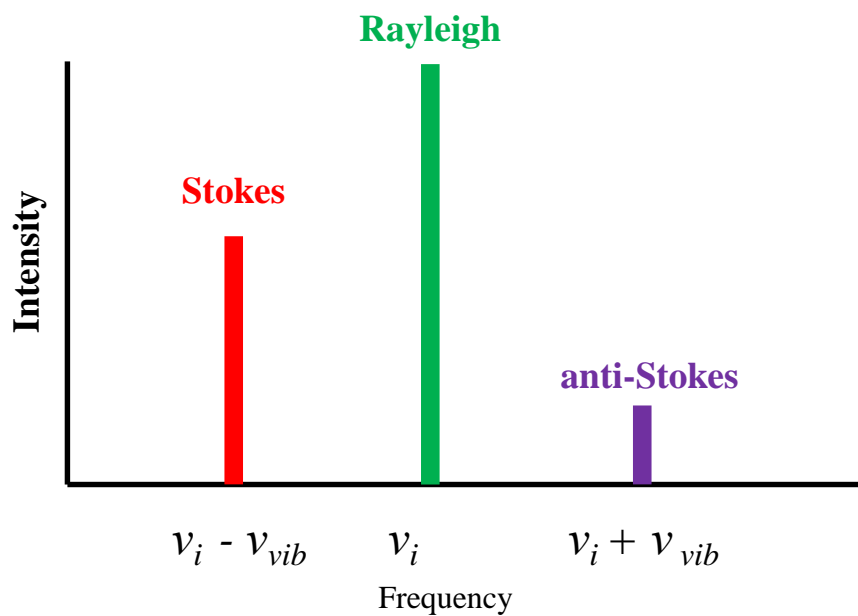


Figure 3.4 Illustration of the relative peak intensities of Rayleigh scattering, Stokes (Raman) scattering, and Anti-Stokes (Raman) scattering.

3.1.4 Fourier Transform Infrared Spectroscopy (FTIR)

The infrared region of the electromagnetic spectrum extends from a wavelength of about 800 nm to longer wavelengths (or shorter wavenumbers). Infrared spectroscopy is an analytical technique that is based on the characteristic vibrational energy levels of a molecule and these are dependent on the characteristics of the molecular bonds of a molecule. An infrared spectrum is commonly obtained by passing infrared radiation through a sample and determining what fraction of the incident radiation is absorbed as a function of photon energy. In a condensed medium, the vibrational energy frequencies of a molecule depend generally on the molecular environment, including the presence of neighbouring groups. An FTIR provides information about the types of bonds present in a material and can be used to characterize or fingerprint these bonds to determine the various molecular structures present in a sample [6]. An FTIR spectrum in the wavenumber range 1500 to 500 cm^{-1} contains peaks characteristic of specific bonds and allows for differentiation between similar structures [7].

One of the great advantages of FTIR spectroscopy is that it can be used to study many different types of samples. Liquids, solutions, pastes, powders, films, fibres, gases and surfaces can all be examined with a careful choice of sampling technique [8]. Even though the radiation used in FTIR is absorbed by water the technique has advantages with respect to Raman spectroscopy; it is easier to use and does not cause fluorescence of a sample.

The FTIR instrument contains four components: a light source, a beam splitter, a sample, and a detector. Light from the source is split and reflected by a stationary mirror

and a moving mirror. The two light beams are combined again to form an interferogram [7]. Following interaction of this light with the sample (either scattering or absorbance), the variation in light energy versus time is measured using the detector. This signal is then converted into a readable spectrum by Fourier transformation of the measured signal intensities.

3.1.5 Nuclear Magnetic Resonance Spectroscopy (NMR)

Nuclear magnetic resonance is a phenomenon that occurs when certain nuclei under a constant magnetic field absorb and re-emit electromagnetic radiation (usually an oscillating radio frequency). Not all nuclei experience this phenomenon since it depends on whether they possess a property called spin. An NMR spectrum is produced by exposing a sample in a magnetic field to a scan of energy in the radio frequency region and causing the spins of appropriate nuclei to flip. The energy at which this occurs is characteristic of the nucleus involved (the type of atom) and the chemical environment in which the atom is located (its near neighbour atoms). The output of an NMR scan is different resonance signals or groups of resonance signals that are scaled in what are called chemical shifts [9]. They can be interpreted to determine the chemical structure of a molecule.

3.1.6 Electrochemical Impedance Spectroscopy (EIS)

Changes in the chemical structure and composition of ILs can be studied using electrochemical impedance spectroscopy (EIS). A change in chemical structure can induce a change in the conductivity of a substance and EIS is used to measure this effect.

Electrochemical impedance spectroscopy was used in this thesis to examine the changes in conductivity of ionic liquid samples when exposed to γ -radiation.

An impedance system can be constructed with any number of ‘electrical’ elements, including resistors and capacitors, in series or in parallel [10]. A resistor is an element that slows the flow of the current. The magnitude of its resistance is generally proportional to its length and the resistance is inversely proportional to its conductivity and cross-sectional area (with respect to the direction of current flow). Ohm’s law links the current that is passing through a resistor, with its resistance (R)

$$I = \frac{\Delta E}{R} \quad (3.5)$$

where I is the current and ΔE is the change in potential across the resistor. A capacitance (C) element can be defined as the derivative of the charge on the element with respect to the applied potential,

$$C = \frac{dQ}{dE} \quad (3.6)$$

where Q is the charge and E is the potential. The derivative of the charge moving through the system with respect to time defines the current, I.

$$I(t) = \frac{dQ(t)}{dt} \quad (3.7)$$

The combination of equations 3.6 and 3.7 provides a relationship between the current and the potential for a capacitor,

$$I(t) = C \frac{dE(t)}{dt} \quad (3.8)$$

In electrochemical impedance spectroscopy a sinusoidally varying potential is applied to a system using a frequency generator and the resulting frequency dependent current in the system is measured [11, 12]. Normally the potential is varied sinusoidally over several orders of magnitude of frequencies, ω , which, in our work, was typically 1 Hz to 10^6 Hz. This applied potential generates a sinusoidal current response,

$$\mathbf{I(t) = I_{amp} \sin(\omega t + \theta)} \quad (3.9)$$

where I_{amp} is the maximum current amplitude and θ is a phase shift. The impedance (Z) of a system is given by the ratio of the applied potential to the resulting current.

$$\mathbf{Z(\omega t) = \frac{E_{amp} \sin(\omega t)}{I_{amp} \sin(\omega t + \theta)}} \quad (3.10)$$

The impedance is purely resistive when the current is in-phase with the applied potential (the phase shift $\theta = 0$). Alternatively, if the phase shift is 90° out of phase the impedance is a purely capacitive response of the system, as shown in Figure 3.5..

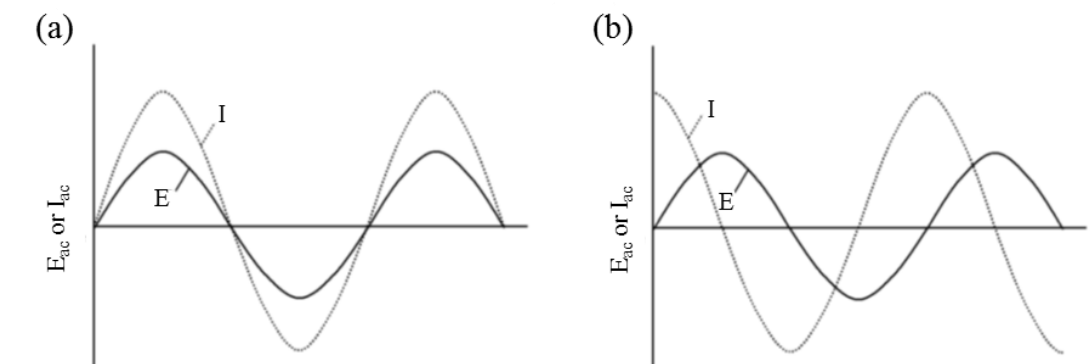


Figure 3.5 The (a) purely resistive and (b) purely capacitive impedance response arising from a given electrochemical impedance experiment [13].

Equation 3.10 can be rewritten to define a complex impedance with real and imaginary components,

$$\mathbf{Z}(\omega t) = \frac{E_{\text{amp}} \sin(\omega t)}{I_{\text{amp}} \sin(\omega t + \theta)} = \mathbf{Z}_r(\omega t) + \mathbf{jZ}_{\text{im}}(\omega t) \quad (3.11)$$

where Z_r and Z_{im} are the real and imaginary components of the impedance, and j is the imaginary unit. The resistance of a system is the real component of the total impedance and the capacitance is contained in the imaginary component, as

$$\mathbf{Z} = \mathbf{R} - \mathbf{j} \frac{1}{\omega C} \quad (3.12)$$

where R is the resistance, ω is the frequency of the applied potential, and C is the capacitance.

Impedance spectra can be presented as either a Nyquist or a Bode plot. A Bode plot consists of two graphs, one with the real part of the impedance (Z_r) as a function of frequency and the second with the phase angle as a function of frequency. For a Nyquist plot the real impedance component is plotted against the imaginary component and is usually extrapolated to a semicircle. The Nyquist and Bode plots are used to compare experimental data to modeling results obtained with an equivalent circuit model that consists of resistive and capacitive components. The fit of the modeling results to the measured data is used to extract a value for the resistance of the system and also to identify the number of different resistance and capacitance components required to fit the data. The latter is normally a characteristic of the number of different physical elements in the system (e.g., the number of different phases).

The electrical conductivity, or specific conductance, can be calculated from the following equation,

$$\sigma = \frac{1}{R} \cdot \frac{\ell}{A} \quad (3.13)$$

where σ is the specific conductance, R is the resistance, and $\frac{\ell}{A}$ is the cell constant defined as the ratio of the gap ℓ to the area of the electrodes A . A cell constant is experimentally determined using standard solutions of KCl (for which the theoretical conductivities are known).

3.2 SURFACE ANALYSES

3.2.1 X-Ray Photoelectron Spectroscopy (XPS)

X-ray photoelectron spectroscopy (XPS) is an atomic spectroscopic technique, which is capable of providing atomic and molecular information regarding the surface of a material. Information such as elemental composition, empirical formula, structure thickness, chemical state, and electronic state of the elements that exist within a material can be obtained through XPS. Photoelectron spectroscopy is based on a single photon/electron ejection process as illustrated in 0. Spectra are obtained by irradiating the material's surface with X-rays and measuring the number of electrons that are ejected as a result of X-ray adsorption and their corresponding kinetic energy (KE). Adsorption of an X-ray, of known energy, by an atom on the sample surface leads to the ejection of a single electron from the inner shell of the atom. The electron's kinetic energy is

measured and the emitting atom is identified from its characteristic electron binding energy [14],

$$KE = h\nu - BE - \phi \quad (3.14)$$

where BE is the binding energy of the electron in the atom that is ionized, $h\nu$ is the energy of the incident X-ray, KE is the kinetic energy of the emitted electron and ϕ is the work function [14]. The work function is a combination of a sample work function and the work function induced by the spectrometer. The sample work function is the minimum amount of energy required to move an electron from the Fermi level of the sample into vacuum, see 0. By directly measuring the kinetic energy of the ejected electron, the binding energy of the emitted electron can be calculated using equation 3.14 (and knowing $h\nu$ and ϕ) [15].

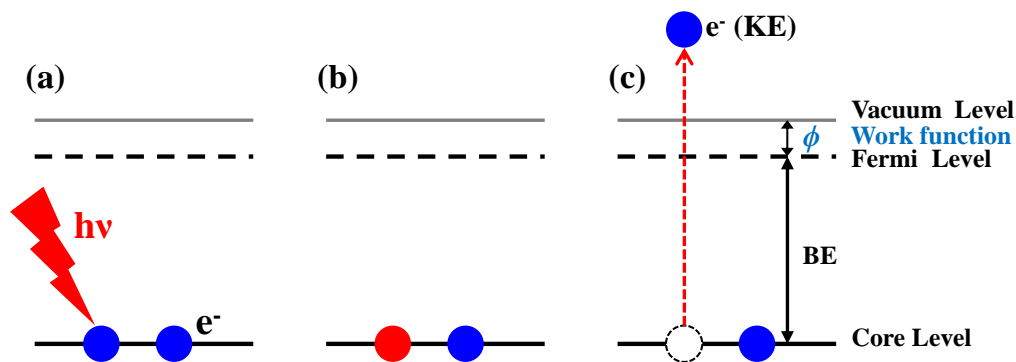


Figure 3.6 Schematic representation of a single photon/electron ejection process.

A typical XPS spectrum is generated by plotting the measured photoelectron intensity as a function of the binding energy of the electrons detected. Each element

produces a set of XPS peaks or lines at characteristic binding energy values. For a given element, small variations in the binding energies can be used to determine the chemical environment of the element and particularly its oxidation state. The intensities of the peaks are directly related to the amount of a particular element within the sample volume that is irradiated.

3.2.2 Scanning Electron Microscopy/ Energy Dispersive X-ray Spectroscopy (SEM/EDX)

Scanning electron microscopy (SEM) is one of the most versatile tools used for the examination and analysis of the structure (including surface topography and composition) of various materials on the micrometer scale [16]. It has many advantages over conventional optical microscopy, such as the ability to attain higher magnification and to obtain better depth resolution. SEM can also be combined with techniques that provide quantitative elemental composition of materials, such as energy dispersive X-ray spectroscopy (EDX).

In SEM a highly-focused primary electron beam with an energy of 0.5 to 30 keV is directed onto a sample surface and this results in the production of secondary electrons, backscattered electrons, characteristic X-rays, and continuum X-rays. The surface topography of a sample is mainly derived from the intensities of the low energy secondary electrons (< 50 eV) that are generated during the process. By measuring the intensity of these secondary electrons as a function of the position of the primary electron beam, an image of a sample surface can be created. Samples are located in a high vacuum chamber (< 10^{-6} Torr) to provide an absorption free path for the electron beam

and the resulting secondary electrons. A schematic of a typical SEM system is illustrated in 0. High spatial resolution with high sensitivity to topographic features on the outermost surface is possible with SEM. It can be attained when the primary electron beam is focused to a very fine spot (0.4 to 5 nm) and when using a primary electron beam with an energy of < 1 kV [17].

Quantitative elemental characterization can be obtained from the sample by employing EDX in combination with SEM. In EDX, as the primary electrons interact with the material surface, the innermost electrons in the atoms are ejected resulting in a vacancy. An electron from a higher orbital can drop down and fill the vacancy. In doing so, it emits a photon that is uniquely characteristic of the element's atomic structure. By measuring the intensity and energy of these photons the elemental composition of the sample can be determined.

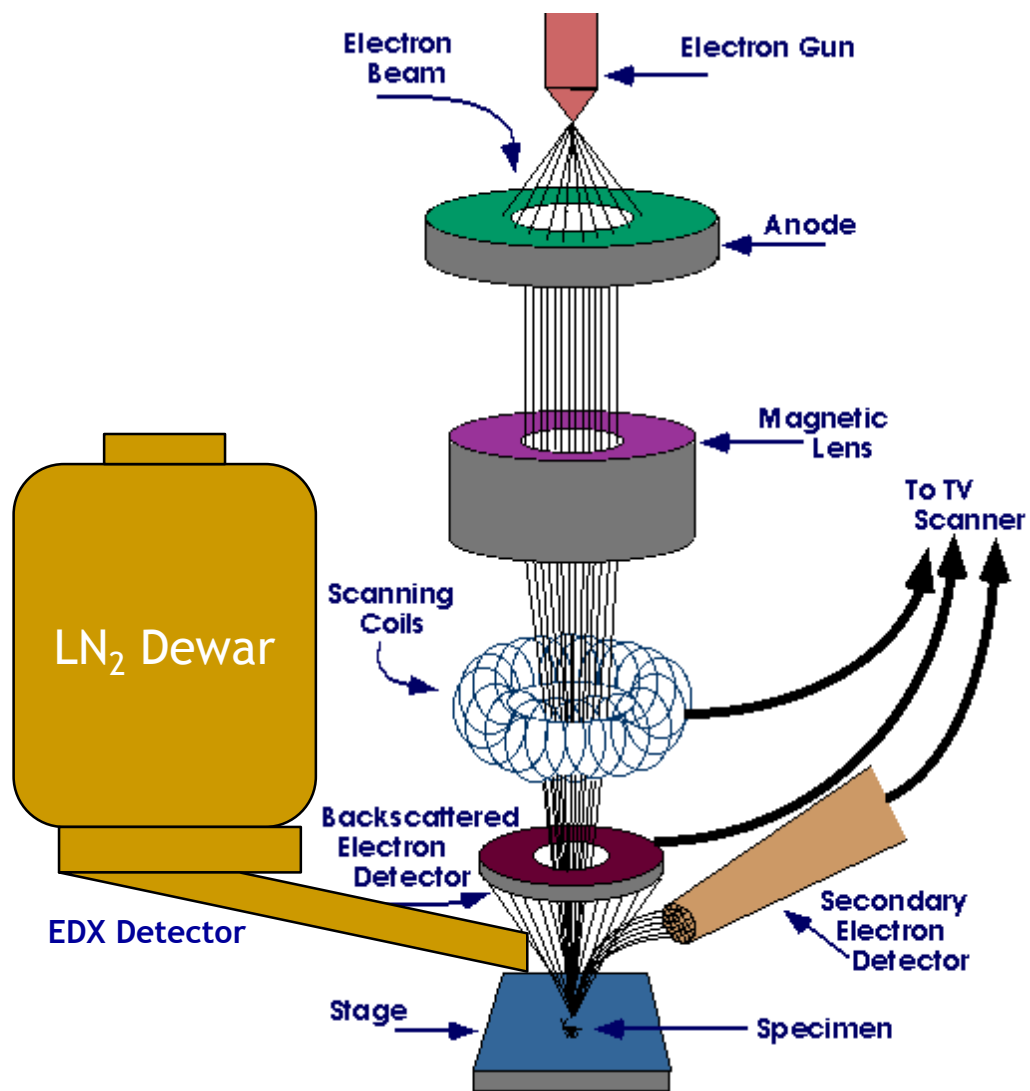


Figure 3.7 Schematic diagram of a scanning electron microscope with an energy dispersive X-ray detector. Image source: <http://www.purdue.edu/rem/rs/sem.htm>

3.3 EXPERIMENTAL PROCEDURES

3.3.1 Sample Preparation

All ionic liquids used in this work were purchased from Sigma-Aldrich, were of the highest purity available ($\geq 95\%$), and were used as received. The purities of the ILs were verified using proton nuclear magnetic resonance spectrometry (^1H NMR).

3.3.1.1 Ionic Liquid Radiolysis Test

In IL radiolysis tests, samples were prepared by placing 0.5 or 2 ml of IL inside a 10 ml pyrex vial (Agilent Technologies). The test vials were prepared inside an argon-purged glove box (Praxair, 99.99% purity) to create a deaerated IL system and were sealed with aluminum crimp caps with PTFE/silicone septa. Multiple vials were prepared for use in trials with different irradiation times.

3.3.1.2 Ionic Liquid Corrosivity Test

Test coupons were fabricated from cylindrical discs cut from an A516Gr70 (Goodfellow) carbon steel (CS) rod, with a composition of C 0.28%, Mn 1.3%, P 0.035%, S 0.035%, Si 0.45% and Fe balance by weight. The carbon steel disc was mounted inside a threaded polytetrafluoroethylene (PTFE) tube using epoxy resin. This PTFE assembly was screwed into the bottom of a glass vial with the carbon steel facing upward as shown in 0. The carbon steel contact with an IL in the vial was limited to a flat surface having an area of 0.385 cm^2 . Prior to a test the carbon steel coupon was abraded sequentially with 400, 800 and 1200 grit silicon carbide papers and finally polished with Texmetmicrocloth (Buehler) using $1\text{ }\mu\text{m}$ MetaDi Supreme diamond paste

suspension (Buehler). The coupon was then rinsed with NANOpure water (Barnstead International) that had a consistent resistivity of $18.2 \text{ M}\Omega\cdot\text{cm}$, sonicated in an acetone/methanol mixture for five minutes to remove polishing residue and dried in flowing Ar. The carbon steel coupon was assembled as illustrated in 0 with 0.5 ml of the desired IL added to the vial to fully immerse the carbon steel surface.

Preparation of the corrosion test vials was performed inside an argon-purged glove box, or in ambient air for deaerated or aerated tests respectively. The carbon steel coupons were exposed to ionic liquid samples for 96 h with or without exposure to γ -radiation. After exposure, the coupon assembly was removed from the test vial and rinsed with acetone to remove any ionic liquid residues. This provided a clean coupon for surface analyses.

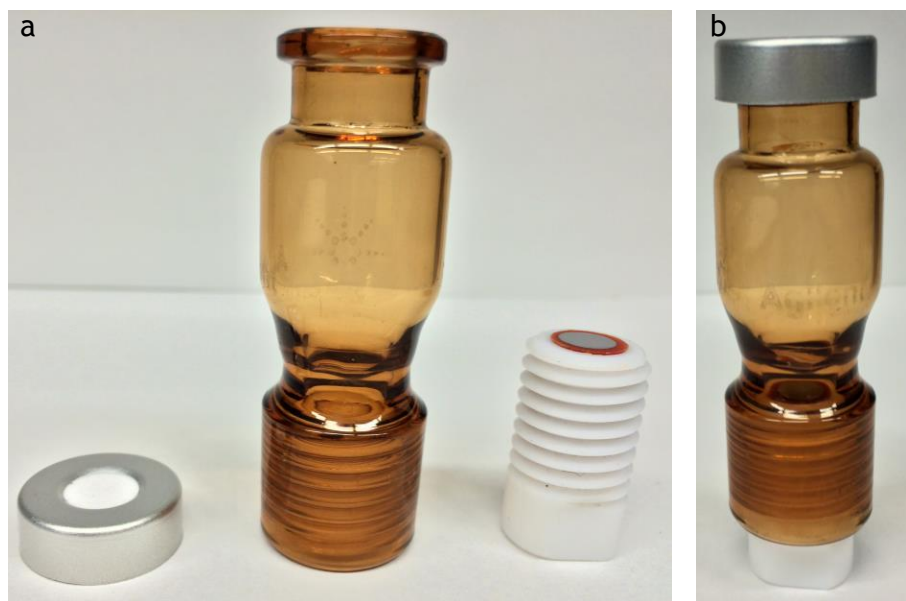


Figure 3.8 Photographs of the vial and carbon steel mount assembly.

3.3.2 Sample Irradiation

Irradiation experiments were carried out in a MDS Nordion Gammacell 220 Excel Cobalt-60 irradiator which emits photons with energy at 1.332 MeV and 1.173 MeV. Test vials containing solutions were placed inside the gamma cell sample chamber and then lowered into the gamma cell irradiation zone to initiate a test. The irradiation zone consisted of 11 tubular pencils containing ^{60}Co arranged in a circle around the sample chamber and provided a uniform absorption dose rate. The dose rate of the gamma cell during the time when these experiments were performed varied from $\sim 4.5 \text{ kGy}\cdot\text{h}^{-1}$ to $3.6 \text{ kGy}\cdot\text{h}^{-1}$ (depending on the date of the experiments, the half-life for decay of ^{60}Co is 5.27 years). Test vials with no exposure to γ -radiation were prepared, treated, handled and analyzed in the same manner as test vials that were exposed to γ -radiation.

3.3.3 Sample Analysis

3.3.3.1 Ionic Liquid Radiolysis Test

Ionic liquid and gas samples were extracted from the test vials after completion of an irradiation period (normally as soon as reasonably possible). Gas analysis was performed using gas chromatography (GC). Gas samples were extracted from the vial's headspace using a gas-tight syringe with a Luer lock valve (Agilent Technologies) and were injected into the gas sampling port of the GC. The GC system consisted of a GS-GASPRO column (0.32-mm I.D. and 60-m long) connected to three detectors: a thermal conductivity detector (TCD), a μ -electron capture detector (μ -ECD), and a mass selective detector (MSD). Measurement of H_2 in the headspace was conducted using the TCD

detector with nitrogen as the carrier gas at a flow rate of $4.6 \text{ ml}\cdot\text{min}^{-1}$ as described in detail by Joseph et al. [18]. Using this method, the detection limit for the gaseous concentration of hydrogen $[\text{H}_2(\text{g})]$ was $4.0\times 10^{-7} \text{ mol}\cdot\text{L}^{-1}$ and the uncertainties in the measurement arising from sampling and instrumental errors were estimated to be $\pm 50\%$ at the low end of the measured concentration range and $\pm 0.005\%$ at the high end of the concentration range. Volatile organic molecules in the headspace were analyzed using the MSD with helium as the carrier gas at a flow rate of $4.6 \text{ ml}\cdot\text{min}^{-1}$.

The UV-Visible spectrophotometry was performed using a diode array spectrophotometer (BioLogic Science Instruments Modular Optical System 450 and ALX 250 lamp with J&M TIDAS NMC 301 detector). Prior to collecting the UV-Vis spectra of samples, a background spectrum of a blank cuvette was recorded first and then automatically subtracted from the subsequent spectra. FTIR analysis was carried out on the IL phase using an attenuated total reflectance (ATR) accessory, where the IL sample was put drop-wise on top of the ATR crystal. The spectra were collected in the frequency range of $4000 - 600 \text{ cm}^{-1}$ using a Bruker Vertex 70v FTIR spectrometer. Raman spectroscopy analysis was performed using a Renishaw model 2000 Raman spectrometer with a laser excitation wavelength of 633 nm. The IL samples were analyzed using a set up with the laser focused perpendicular to the side of the sample vial. For NMR spectroscopy ionic liquid samples were diluted in deuterated acetone and ^1H , ^{13}C , ^{31}P and ^{19}F NMR spectra were collected using a Varian INOVA 400 MHz or INOVA 600 MHz spectrometer. The chemical shifts were referenced to a residual acetone peak (2.03 ppm and 28.90 ppm) for ^1H and ^{13}C , respectively.

The conductivities of the ILs were measured using EIS. The EI spectra were acquired using a Solartron potentiostat model 1287 and a 1250 Solartron frequency response analyzer. The frequencies used for the EIS measurement were in the range of 0.1 Hz to 65 kHz. Data acquisition and analysis were controlled using the Zplot and Zview software packages, respectively. The conductivity cell constant was determined prior to each set of analyses using KCl solutions for which the conductivity is known and was 8.6 cm^{-1} .

3.3.3.2 Ionic Liquid Corrosivity Test

After a test with the desired contact time between ionic liquid and carbon steel, test vials were disassembled and the CS coupons were rinsed, dried, and stored under vacuum until instrument time was available for surface analysis at Surface Science Western or Western Nanofabrication Facility. Focused ion beam, Scanning electron microscopy, energy dispersive X-ray spectroscopy, X-ray photoelectron spectroscopy, and Raman spectroscopy were performed to study the composition and morphology of any oxide films that had formed on the carbon steel surfaces. The ionic liquid samples rinsed from the coupon were kept and analyze for iron content using inductively-coupled plasma mass spectrometry.

3.4 REFERENCES

- [1] M.C. McMaster, *GC/MS. A Practical User's Guide*, Wiley-InterScience, John Wiley & Sons, Hoboken, NJ, (2008).
- [2] T. Owen, *Fundamentals of Modern UV-Visible Spectroscopy*, Agilent Technologies, Germany (2000).
- [3] R.L. McCreery, *Raman Spectroscopy for Chemical Analysis*, John Wiley & Sons, New York, NY (2000).

- [4] J.R. Ferraro, K. Nakamoto, *Introductory Raman Spectroscopy*, Academic Press, San Diego, CA (1994).
- [5] W.A. England, M.J. Bennett, D.A. Greenhalgh, S.N. Jenny, C.F. Knights, *Corros. Sci.*, 26 (1986) 537.
- [6] M.J. Walzak, R. Davidson, M. Biesinger, *J. Mater. Eng. Perform.*, 7 (1998) 317.
- [7] N. Jaggi, D.R. Vij, *Fourier Transform Infrared Spectroscopy*, in: *Handbook of Applied Solid State Spectroscopy*, D.R. Vij, Editor, Springer Science + Business Media, New York, NY (2006).
- [8] B. Stuart, *Infrared Spectroscopy: Fundamentals and Applications*, John Wiley & Sons, England, (2004).
- [9] H. Günther, *NMR Spectroscopy: Basic Principles, Concepts and Applications in Chemistry*, Wiley-VCH Verlag, Weinheim, Germany (2013).
- [10] M.E. Orazem, B. Tribollet, *Electrochemical Impedance Spectroscopy*, John Wiley & Sons, New York, NY (2008).
- [11] P. Monk, *Fundamentals of Electroanalytical Chemistry*, John Wiley & Sons, Chichester, UK (2001).
- [12] P. Wasserscheid, T. Welton, Editors, *Ionic Liquids in Synthesis*, Wiley-VCH Verlag, Weinheim, Germany (2008).
- [13] K.J. Daub, *A Study of Gamma Radiation Induced Carbon Steel Corrosion*, Ph.D. Thesis, Department of Chemistry, University of Western Ontario, London, Ontario (2013).
- [14] H.R. Verma, *Atomic and Nuclear Analytical Methods: XRF, Mossbauer, XPS, NAA and Ion-Beam Spectroscopic Techniques*, Springer-Verlag, Berlin, Germany (2007).
- [15] D.J. O'Connor, B.A. Sexton, *Surface Analysis Methods in Materials Science*, Springer-Verlag, Berlin, Germany (1992).
- [16] F. Adams, L. Van Vaeck, R. Barrett, *Spectrochim. Acta Part B*, 60 (2005) 13.
- [17] R.F. Egerton, *Physical Properties of Electron Microscopy: An Introduction to TEM, SEM and AEM*, Springer, New York, NY (2005).
- [18] J.M. Joseph, B. S. Choi, P.A. Yakabuskie, J.C. Wren, *Radiat. Phys. Chem.*, 77 (2008) 1009.

Chapter 4

The Molecular Structures and the Relationships between the Calculated and Observed Bulk Phase Properties of Phosphonium-Based Ionic Liquids

4.1 INTRODUCTION

Interest in ionic liquids has recently grown due to their many desirable physical and chemical properties. One of their interesting features is their tunability [1-10]. There are an enormous number of possible ion pair combinations that have different physical and chemical properties. Rogers and Seddon [10] estimated the number to exceed one trillion. Given this sumptuous banquet of choice, we need an efficient methodology for pre-determining the physicochemical properties of any particular ion pair. A versatile method for predicting the properties of a molecule is the use of quantum chemical calculations. Such computations allow us to simultaneously predict the values of multiple parameters (such as dipole moment, bond lengths, atomic charges, etc.) that are related to a molecule's kinetic, thermodynamic and physicochemical properties.

Computational quantum chemical calculations using density functional theory have been used extensively to obtain molecular properties of ILs such as hydrogen (H-) bond strengths [11-16], cation-anion interaction energies [16, 17], electron affinities and ionization energies [18]. The results have been used to elucidate relationships between molecular properties and macroscopic, bulk-phase properties of ILs [11-29]. Due to their high conductivity (ca. 10 mS/cm) and wide window of electrochemical stability (ca. 4 V),

imidazolium-based ILs are excellent candidates for a range of applications including, but not limited to, catalysis, super-capacitors, and photovoltaics [30]. Thus, imidazolium-based ILs have been extensively investigated using quantum chemical calculations [11-19, 22-28]. Phosphonium-based ILs have been less well studied. These ILs have shown higher thermal stability and lower toxicity, compared to imidazolium-based ILs, and there are exciting prospects for their use in industrial applications [7-9, 29].

This chapter presents quantum chemical calculations performed using density functional theory (DFT) on six tetradecyl(trihexyl)phosphonium [P₁₄₆₆₆] cation-based ILs that had different anions: chloride [Cl], bromide [Br], dicyanamide [DCA], tetrafluoroborate [BF₄], hexafluorophosphate [PF₆] and bis(trifluoromethylsulfonyl)imide [NTf₂], 0. Quantum chemical parameters of the ILs that were obtained include the inter-ionic H-bond length and angle, the energies of various molecular orbitals including those of the highest occupied and the lowest unoccupied molecular orbitals (HOMO and LUMO), the dipole moment (μ), the cation-anion interaction energy, and the electrostatic potential. Trends in the calculated dipole moments (μ) and interaction energies (ΔE) were compared to trends in some of the observed bulk properties of the ILs (conductivity, melting point and viscosity).

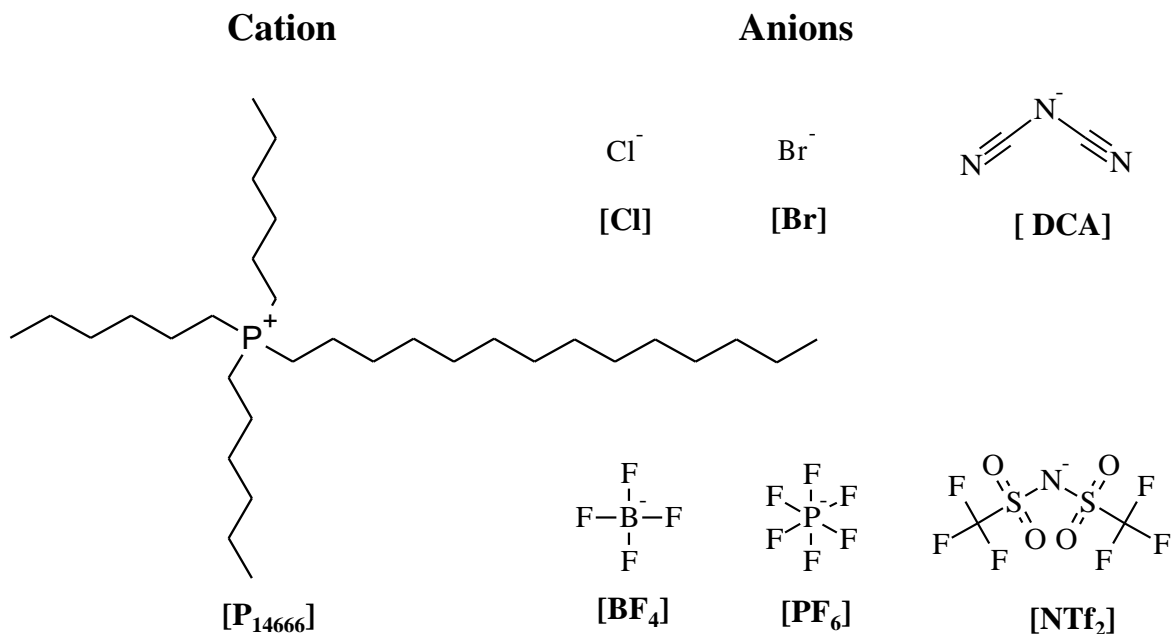


Figure 4.1 Chemical structures of the phosphonium cation and the anions of the ILs used in this study.

4.2 METHODOLOGY

4.2.1 Computational Details

Quantum chemical calculations were performed using a quantum mechanics computer program, Materials Studio version 5.5 software (Accelrys Inc., San Diego, CA) [31]. The geometrical structures of the ILs were sketched using tools available in the Materials Visualizer module of the Materials Studio program. The DMol³ module was then used to optimize the geometries of the IL molecules and to obtain quantum chemical parameters. The DMol³ module performs DFT calculations using *ab initio*, generalized gradient approximations (GGA) with a double numerical plus polarization (DNP) basis set and two different exchange-correlation functionals. These functionals are labelled

Becke-Lee-Yang-Parr (BLYP) [32, 33] and Perdew-Wang (PW91) [34]. The BLYP and PW91 functionals were chosen because both belong to a group of the most frequently used density functionals and because their exchange-correlations represent two extreme behaviours at large density gradients. The BLYP functional is a strongly divergent exchange functional while PW91 is an exchange functional that converges as the enhancement factor approaches asymptotically to zero when the reduced density gradient approaches infinity [35]. These functionals are both known to deliver reliable results for covalent, ionic, metallic and hydrogen bridge bonds. However they typically fail to take into account the contributions from van der Waals interactions [36]. Nevertheless, these functionals have been shown to provide accurate geometries and electronic structures for a range of ILs [15, 37, 38].

To find the most stable molecular conformation, multiple calculations with each functional were performed with different initial guess geometries. This gives us high confidence that the optimized geometries determined were not false minima due to an unknown bias in the initial molecular conformation.

The DMol³ module was also used to calculate the energies of various molecular orbitals (including HOMO and LUMO), the dipole moment (μ) and the electrostatic potential of the ILs. The energies of the optimized ion pair and the isolated anion and cation (E_{AC} , E_A , and E_C , respectively) were also calculated in order to obtain the cation-anion interaction energy (ΔE). This is the energy required to separate the ion-pair into its ion fragments and is calculated from:

$$\Delta E = E_{AC} - (E_A + E_C) \quad (4.1)$$

Spectroscopic information was obtained for three selected ILs, ($[P_{14666}] [Br]$, $[P_{14666}] [DCA]$ and $[P_{14666}] [NTf_2]$). Using the same DFT methodology, the vibrational frequencies of these ILs were calculated. From these vibrational frequencies, theoretical IR spectra were generated. Time-dependent DFT (TD-DFT) calculations with the same functionals and the GGA-DNP basis set were also used to obtain the wavelengths and oscillator strengths of various electronic transition lines.

4.2.2 Spectroscopic Measurements

The infrared spectra of the selected ILs ($[P_{14666}] [Br]$, $[P_{14666}] [DCA]$ and $[P_{14666}] [NTf_2]$) were recorded in the 4000 to 400 cm^{-1} frequency range. The ILs were pressed into a KBr pellet for these measurements. The UV-Visible spectra obtained for the ILs were placed in a quartz cuvette with 1.5 mm path length.

4.3 RESULTS AND DISCUSSION

4.3.1 Optimized Geometries

The most stable molecular conformations were obtained following the procedure described above. For simplicity, only one stable configuration for each IL is shown in 0. The DFT calculation results show the existence of inter-ionic H-bonds in all of the ILs studied. An H-bond is considered to be present if the distance between a hydrogen atom and a neighbouring atom, X, is less than sum of their van der Waals radii [39]. These distances are 2.95 Å, 3.05 Å, 2.67 Å, and 2.75 Å for C—H...Cl, C—H...Br, C—H...F and C—H...N, respectively. An additional criterion for hydrogen bonding is used for the C—H...O association. According to Jeffrey, an H-bond in a C—H...O structure is

present if the H...O distance is less than 2.72 Å and if the angle created by the three atoms is greater than 90° [40]. The inter-ionic H-bond lengths and angles of the phosphonium ILs studied are listed in 0. Although the results show a small dependence on the exchange functional used, the calculated H...X distances in some C_n—H_n ... X_n groups (*n* is the index number for an atom in the molecule) are less than sum of their van der Waals radii.

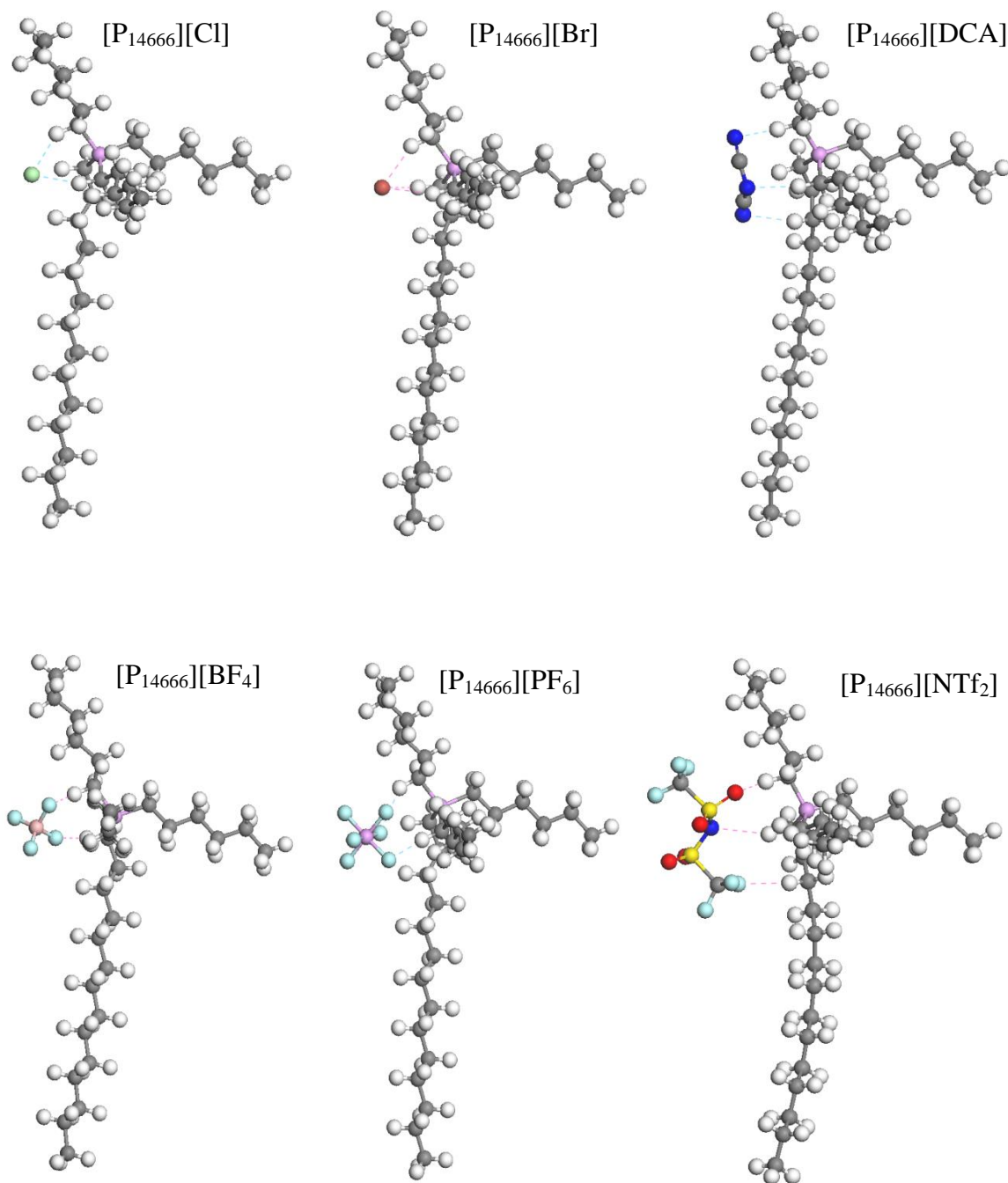


Figure 4.2 The equilibrium geometries of phosphonium ILs. Dashed lines represent the hydrogen bonds between the atoms. The colour assignments for the atoms are: purple - P, maroon - Br, blue - N, red - O, yellow - S, light-blue - F, peach - B, dark-gray - C atoms, and light-gray - H.

The calculated electrostatic potential maps for the optimized structures of the ILs are presented in 0. Different colours represent different electrostatic potentials, going from the most negative to most positive electrostatic potential, red < orange < yellow < green < blue. As expected, the anions are located close to the most positively charged region of the cation. The negative charge is localized on the anions; for the polyatomic anions, the most negative regions are the nitrogen atoms in the anion [DCA], the fluorine atoms in both anions [BF₄] and [PF₆], and the oxygen and nitrogen atoms in the anion [NTf₂]. The most positively charged region in the cation is the phosphorus atom. However, the region around one of the three short aliphatic chains is also partially charged. This can be attributed to the electron-withdrawing effect of the aliphatic chain close to the counter anion.

Table 4.1 Hydrogen bond lengths (Å) and angles for phosphonium-based ILs.

Hydrogen bonds	BLYP		PW91	
	(Å)	angle (°)	(Å)	angle (°)
[P₁₄₆₆₆] [Cl]				
C ₆ —H ₄₆ ¹ ... Cl	2.38	141	2.46	134
C ₁₃ —H ₆₁ ... Cl	2.44	143	2.39	139
[P₁₄₆₆₆] [Br]				
C ₆ —H ₄₆ ... Br	2.57	142	2.49	143
C ₁₃ —H ₆₁ ... Br	2.59	147	2.51	147
C ₁₉ —H ₇₃ ... Br	2.81	139	2.73	137
[P₁₄₆₆₆] [DCA]				
C ₆ —H ₄₆ ... N ₁₀₅	2.39	150	2.35	144
C ₁₃ —H ₆₁ ... N ₁₀₂	2.44	159	2.45	158
C ₂₁ —H ₇₂ ... N ₁₀₆	2.50	149	2.39	150
[P₁₄₆₆₆] [BF₄]				
C ₆ —H ₄₆ ... F ₁₀₆	2.27	139	2.17	124
C ₁₃ —H ₇₃ ... F ₁₀₅	2.26	133	2.16	136
[P₁₄₆₆₆] [PF₆]				
C ₆ —H ₄₆ ... F ₁₀₅	2.27	140	2.17	141
C ₁₃ —H ₆₁ ... F ₁₀₈	2.19	166	2.43	166
[P₁₄₆₆₆] [NTf₂]				
C ₆ —H ₆₁ ... O ₃₆	2.26	172	2.23	171
C ₆ —H ₆₀ ... F ₄₂	2.55	139	2.49	139
C ₁₉ —H ₈₈ ... N ₄₈	2.38	153	2.23	153

¹ The subscripts on the elements indicate the location of the atom in the IL molecule (detail not shown in 0).

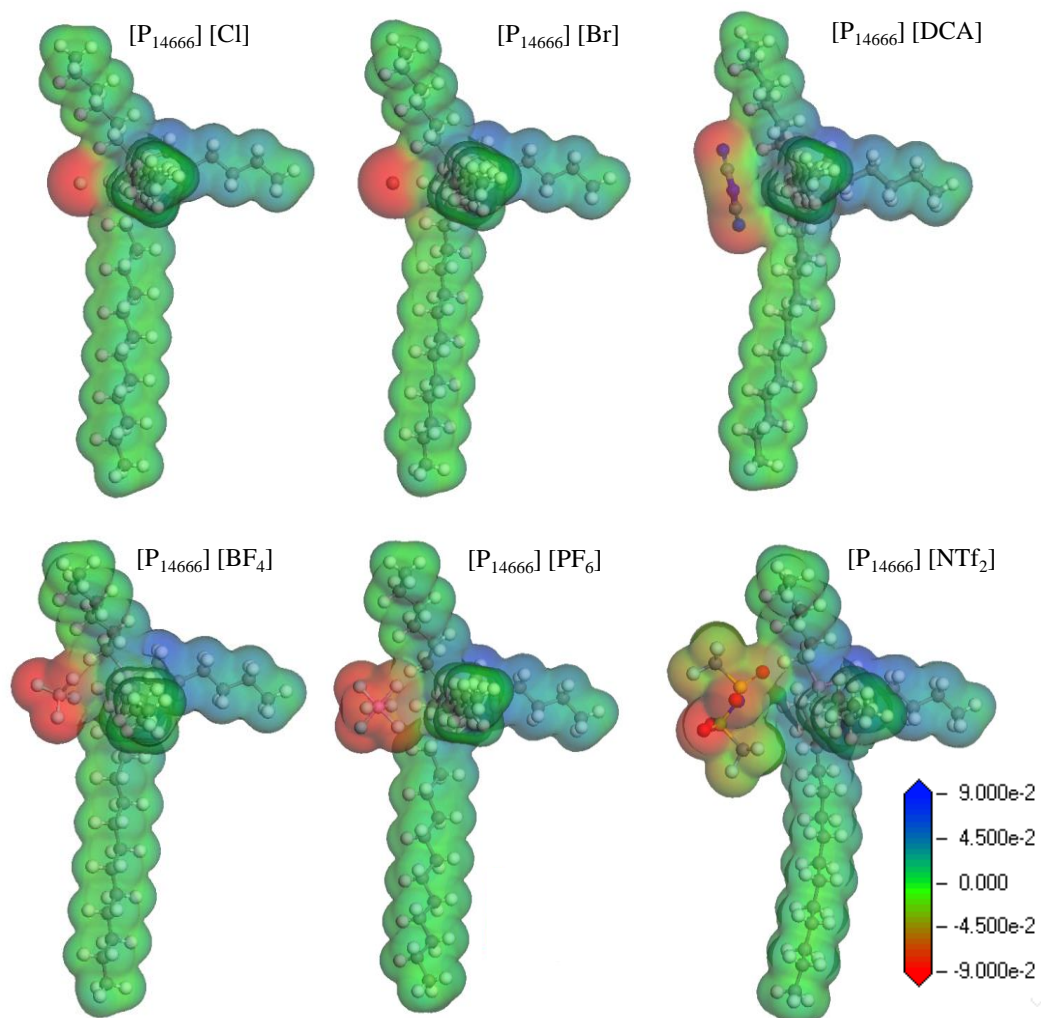


Figure 4.3 Electrostatic potentials of phosphonium ILs mapped onto an electron density isosurface of 0.017 e/au^3 . The electron density scale spans -0.09 (red) through 0.0 (green) to $+0.09$ (blue).

The calculated molecular parameters (energies of the HOMO and LUMO, the energy gap (ΔE_{H-L}) between E_{HOMO} and E_{LUMO} , dipole moment (μ), and the cation-anion interaction energy (ΔE)) are listed in 0. As for the inter-ionic H-bond lengths and angles, small differences were observed between the values calculated using the BLYP and PW91 functionals. The largest difference is observed for the anion containing the largest atom, Br, possibly due to less accurate density functions for such a large atom. The ΔE_{H-L} and ΔE values from the two functionals are comparable; their values agree within 7% variance. The ΔE_{H-L} values determined for the phosphonium ILs range from 3.37 eV to 6.44 eV. Since electron transfer from HOMO to LUMO is more energetic for a larger ΔE_{H-L} , a large ΔE_{H-L} is generally associated with low chemical and thermal reactivity [41-46]. The relatively large ΔE_{H-L} values calculated are consistent with the thermal and chemical stabilities reported for phosphonium-based ILs [20].

Table 4.2 Calculated properties for the phosphonium-based ILs.

IL	E_{HOMO} (eV)		E_{LUMO} (eV)		$\Delta E_{\text{H-L}} = E_{\text{HOMO}} - E_{\text{LUMO}}$ (eV)		Dipole moment (Debye)		ΔE (kJ/mol)	
	BLYP	PW91	BLYP	PW91	BLYP	PW91	BLYP	PW91	BLYP	PW91
[P ₁₄₆₆₆] [Cl]	-3.53	-3.95	0.18	0.16	-3.71	-4.11	10.4	9.5	-534.8	-551.9
[P ₁₄₆₆₆] [Br]	-3.48	-3.85	-0.11	-0.11	-3.37	-3.74	11.7	11.1	-475.2	-525.1
[P ₁₄₆₆₆] [DCA]	-4.10	-4.37	-0.42	-0.50	-3.68	-3.87	15.9	15.8	-496.5	-503.6
[P ₁₄₆₆₆] [BF ₄]	-6.13	-6.33	-0.25	-0.34	-5.88	-5.99	14.2	13.2	-741.2	-768.7
[P ₁₄₆₆₆] [PF ₆]	-6.77	-6.94	-0.33	-0.51	-6.44	-6.43	14.4	13.9	-823.9	-829.1
[P ₁₄₆₆₆] [NTf ₂]	-5.82	-6.05	-0.61	-0.64	-5.21	-5.41	17.3	16.5	-381.4	-383.4

4.3.2 IR and UV-Vis Spectra

To determine how well the DFT calculations performed, theoretically constructed spectral bands or normal modes are compared to experimentally obtained IR and UV-Vis spectra for the ILs. The theoretical IR spectra were constructed from the calculated vibrational frequencies of the optimized structures of three selected ILs, [P₁₄₆₆₆] [Br], [P₁₄₆₆₆] [DCA] and [P₁₄₆₆₆] [NTf₂] and these spectra are compared with observed IR spectra in 0. The theoretical IR spectra obtained using the two different functionals are very similar for all three ILs. The calculations reproduce the peak positions and the relative intensities of most of the IR peaks for all ILs, except for the peaks near 3000 cm⁻¹. Those peaks show slight blue shifts compared to the observed peaks. The peaks at this wavenumber correspond to the CH₂ bending frequencies of the alkyl chain of the [P₁₄₆₆₆] cation. There could be two main reasons for the slight shift in the observed spectra. First, is that the functional used (even reported to be accurate) were not exact and is based on many approximations and parameterized factors. Therefore solving for an exact vibrational energy is may be not possible and will always leave room for uncertainty. The other reason is that the vibrational energies were calculated for an isolated molecule while the measured IR spectra were taken with ILs in a condensed phase. Thus, the small differences between experimental and theoretical spectra could also be possibly due to the fact that intermolecular forces and interactions were not taken into account in constructing the theoretical IR spectra. Many other theoretical IR calculations reported in the literature show significant differences in the spectral positions of vibrational modes compared to experimental observations for the same reason [19, 47, 48]. In the case of our ILs, the CH₂ bending mode will be particularly affected by

intermolecular interactions. The excellent agreement between the theoretical and measured spectra elsewhere gave us confidence in the utility of the chosen functionals for calculation of other IL properties and the acceptability of the level of numerical accuracy that we applied in our calculations.

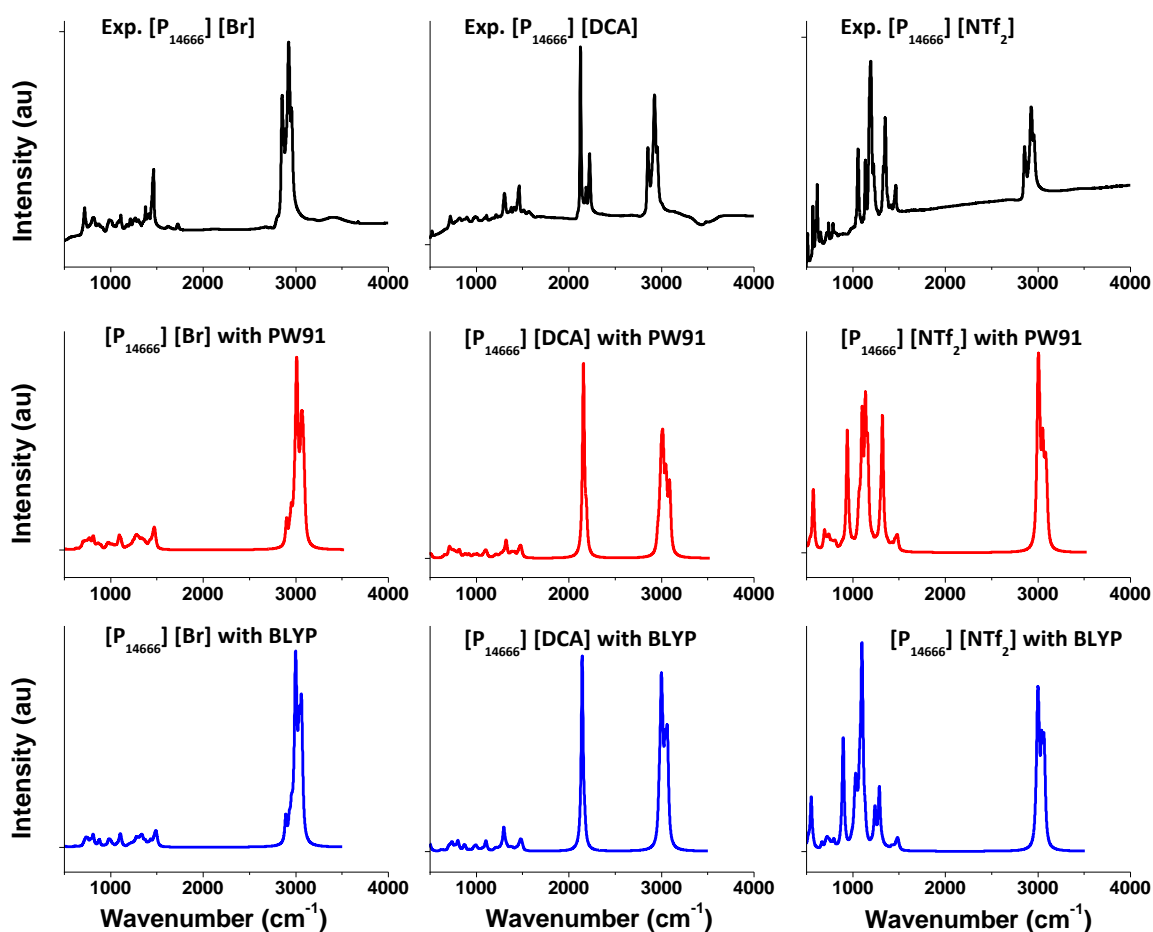


Figure 4.5 Measured (the top panel) and calculated (the lower two panels) IR spectra of selected ILs. The calculated results were obtained using two functionals, BLYP and PW91.

The measured UV-Visible absorption spectra are compared with Franck-Condon electronic transition energies between calculated energy states (shown as vertical lines in 0). The calculations considered transitions between low-lying excited states (up to 25 states were considered). The wavelengths of the main calculated transitions in the range of 275 nm and 450 nm are compared with the measured peak maxima, λ_{max} in 0. The transition from the ground state to the first excited state (HOMO \rightarrow LUMO) should correspond to the longest wavelength. The calculated wavelength corresponding to this transition is close to the measured λ_{max} of the peak appearing at the longest wavelength, 0. The wavelengths of other calculated transition lines having strong oscillator strengths are also close to the λ_{max} of other measured peaks, 0. The calculated transition wavelengths are, in general, blue shifted compared to the measured λ_{max} . This shift may be again attributed to the fact that intermolecular forces and interactions were not taken into account in the calculations. Such shifts are known. An electronic transition spectral shift due to the influence of surrounding molecules or a solvent (that is more noticeable in the electronic transitions) is labelled a solvatochromic shift. The solvatochromic shift depends on solvent polarity [49, 50]. The change in absorption or emission line positions arises from the fact that polarities of the ground and excited state of a chromophore are different. A polar solvent then differentially stabilizes the ground and excited states and hence, can change the energy gap between these electronic states [50]. The presence of neighbouring IL molecules also affects the electronic transition probabilities, due to the Franck-Condon vertical transitions principle. The differences between the calculated and observed electronic transition energies in the case of our ILs are small, less than 10%. This indicates that the electronic stabilizing forces of the ILs act similarly on both ground

and excited states and do not significantly influence their electronic state energies. This evidence for only a small solvent effect may explain the strength of the correlations found between the molecular properties determined by the DFT calculations of isolated ion pairs and the bulk phase properties of the ILs, as discussed below.

Table 4.3 Calculated electronic transition parameters and experimental UV-Vis absorption parameters for selected phosphonium-based ILs.

IL	Theoretical*				Experimental	
	λ (nm)	MO Transition**	<i>oscillator</i> <i>strength (f)</i>	E (eV)	λ_{max} (nm)	E (eV)
[P ₁₄₆₆₆] [Br]***	370	H → L	0.0002	3.35	297	4.17
	361	H+2 → L	0.0020	3.43		
	358	H+2 → L-1	0.0029	3.46		
	356	H+2 → L-2	0.0056	3.48		
	297	H → L-5	0.0018	4.18		
	293	H+1 → L-5	0.0036	4.23		
	291	H+2 → L-5	0.0020	4.25		
[P ₁₄₆₆₆] [DCA]	323	H → L	0.0024	3.84	314	3.95
	298	H → L-2	0.0006	4.16		
	291	H → L-3	0.0015	4.25		
	281	H → L-4	0.0005	4.41		
[P ₁₄₆₆₆] [NTf ₂]	279	H → L	0.0006	4.45	300	4.13

* Calculated values using the BLYP/GGA/DNP methodology.

** H; HOMO, H+1; next HOMO, H+2; 2nd next HOMO etc.

L; LUMO, L-1; next LUMO, L-2; 2nd next LUMO etc.

*** The transitions listed for [P₁₄₆₆₆] [Br] are only those with more than 5% contribution.

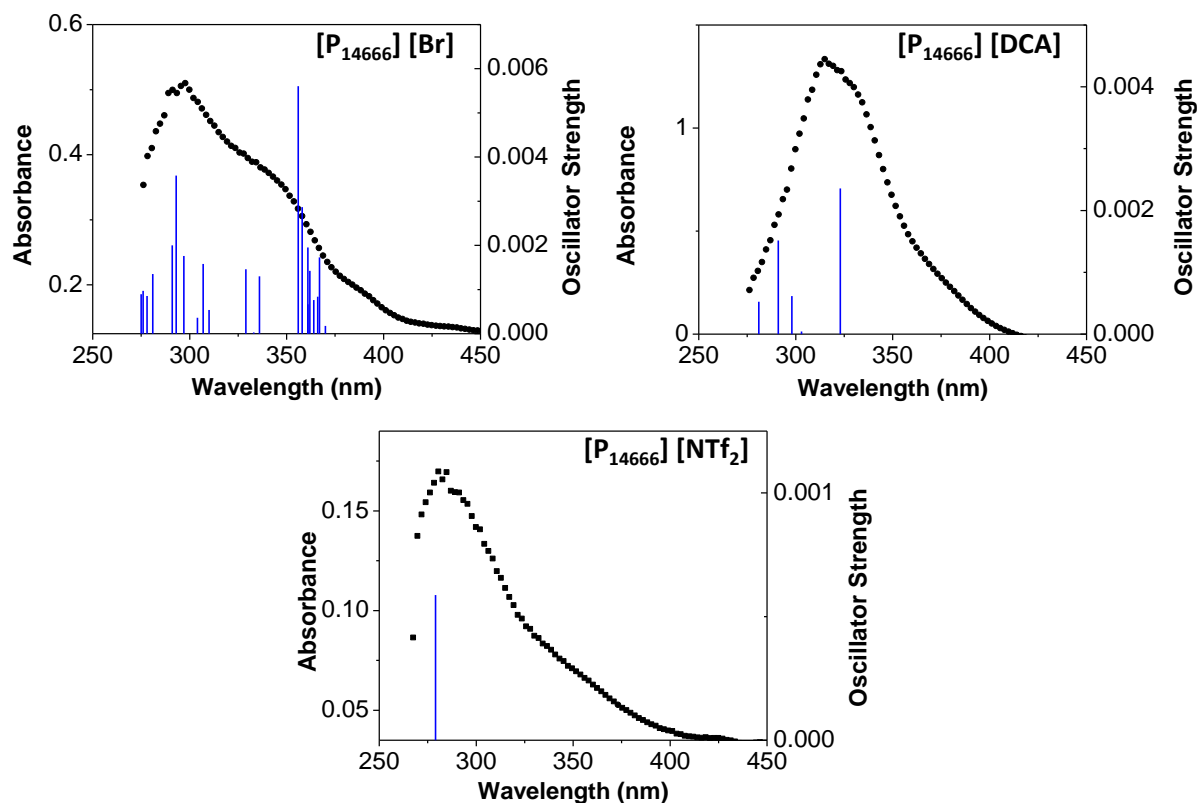


Figure 4.5 Calculated electronic transition lines overlaid on the measured UV-Visible spectra of selected ILs. The calculated results were obtained using the BLYP functional.

4.3.3 Correlations between Molecular and Bulk Properties

Various studies have shown that correlations exist between the physicochemical properties of an IL and the molecular parameters obtained from DFT calculations for an isolated molecule. All six ILs studied here have large calculated dipole moments, consistent with their reported high conductivities [6, 20, 51, 52]. It has been suggested that the conductivity of an IL may be derived from the dipole moment of the IL. In their study on tetra-alkyl phosphonium iodide ILs, Benavides-Garcia and Monroe have found that a high ionic conductivity is associated with a large dipole moment value [20, 51].

We have also found such a correlation for the six phosphonium-based ILs studied. 0 shows that the measured molar conductivity increases exponentially with the calculated dipole moment (the molar conductivity values were taken from reference [52]). A small deviation from the exponential dependence was observed for [P₁₄₆₆₆] [Cl], suggesting that the size of the anion may be an additional, albeit minor, factor in determining the conductivity of an IL.

Tsuzuki et al. [53] have reported that the cation-anion interaction energy, ΔE , is an important factor in determining viscosity, the larger the anion-cation interaction (the more $-\Delta E$), the higher the viscosity. However, we do not see a good correlation between viscosity and ΔE (see 0). This may be due to stronger influences of molecular size and shape on viscosity. Instead, we have found a strong correlation between viscosity and dipole moment (see 0) with viscosity decreasing exponentially with dipole moment. As for the relationship between molar conductivity and dipole moment, a small deviation is observed for the small anion IL, [P₁₄₆₆₆] [Cl]. The observation that conductivity increases while the viscosity decreases exponentially with dipole moment is also consistent with Walden's rule. This rule states that, for ions in solution, the product of the viscosity and molar conductivity at infinite dilution in an electrolytic solution is constant, independent of the solvent [1]. That the viscosities and conductivities of the phosphonium ILs follow Walden's rule suggests that diffusion of an IL molecule within bulk IL is primarily controlled by the ion moieties of the IL molecule. If this is the case, the dipole moment may be the main factor to consider in determining the viscosity and conductivity of the IL. The [P₁₄₆₆₆] [PF₆] IL, which has been reported to exhibit an exception to Walden's rule [52], also shows a small deviation from the exponential

dependence of viscosity on dipole moment. Our calculations show that this IL has the strongest H-bond (0) and the largest cation-anion interaction energy (ΔE) (0). Thus, there is a higher probability of $[P_{14666}] [PF_6]$ diffusing as an ion-pair, rather than as separate ions. One of the factors that can lead to an exception to Walden's rule is a higher ion-pair density in an IL [1-3].

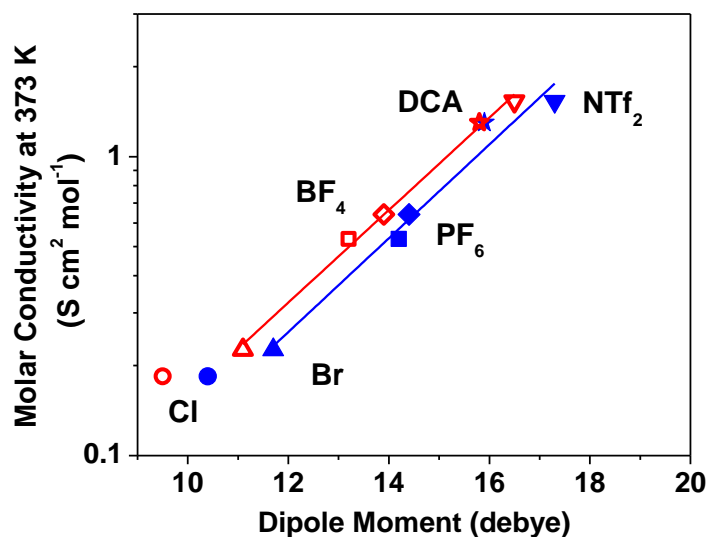


Figure 4.6 Relationship between the calculated dipole moments and the molar conductivity of the phosphonium ILs. The conductivity values were taken from ref. [52]. The solid and open symbols are the calculated values using the BLYP and PW91 functionals, respectively.

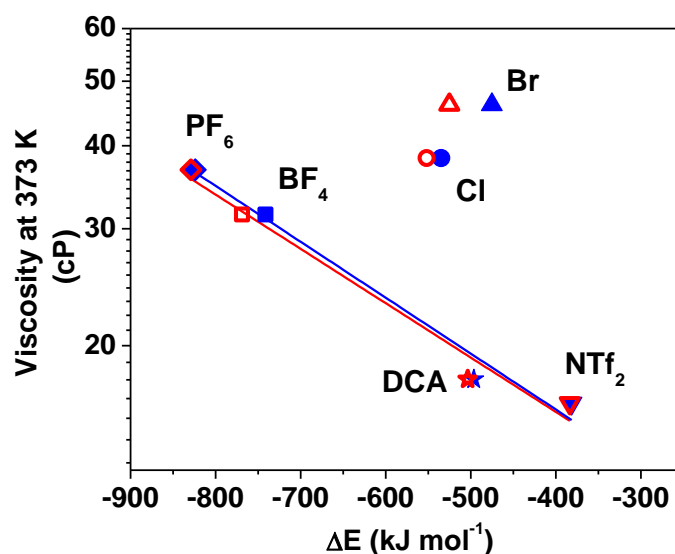


Figure 4.7 Relationship between the calculated interaction energy (ΔE) and the viscosity of the phosphonium ILs. The viscosity values were taken from ref. [52]. The solid and open symbols are the calculated values using the BLYP and PW91 functionals, respectively.

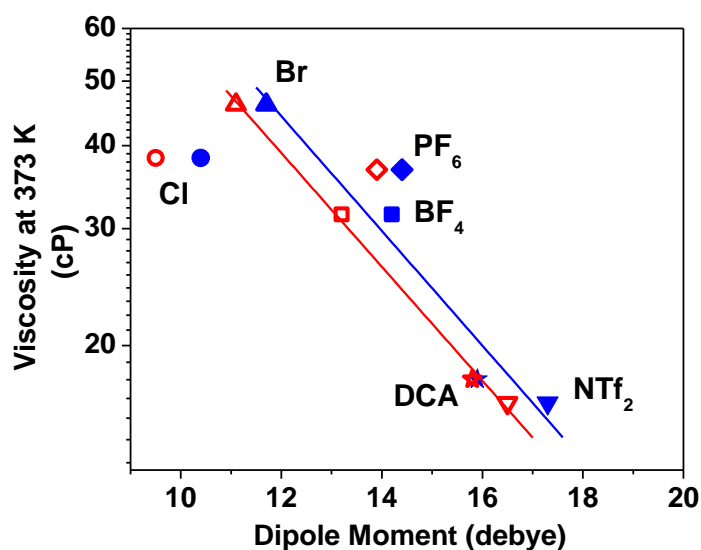


Figure 4.8 Relationship between the calculated dipole moment and the viscosity of the phosphonium ILs. The viscosity values were taken from ref. [52]. The solid and open symbols are the calculated values using the BLYP and PW91 functionals, respectively.

It has been reported that a more negative ΔE is correlated with a higher melting point [14]. The phosphonium ILs studied here have large negative values of ΔE (0) as a result of the strong Coulombic interaction between the anion and the cation within the IL. Many long-range intermolecular interactions contribute to the melting point of an IL and knowledge of the interaction energy of an isolated ion-pair alone should not be sufficient to predict this property of the condensed IL phase. Nevertheless, for the phosphonium ILs studied, the ΔE does correlate well with melting point, 0. (The melting points shown in 0 were taken from ref. [54]. No melting points have been reported for $[P_{14666}] [Cl]$ and $[P_{14666}] [DCA]$ and hence these ILs are not included in 0). The strong correlation found between the melting point and ΔE is somewhat surprising since the melting point is mainly governed by intermolecular interactions. It may be that the strength of intermolecular interactions is proportional to the intramolecular Coulombic interaction in the bulky and viscous phosphonium ILs. This question can be addressed by molecular dynamic calculations on IL clusters of different sizes, an activity that is beyond the scope of this thesis.

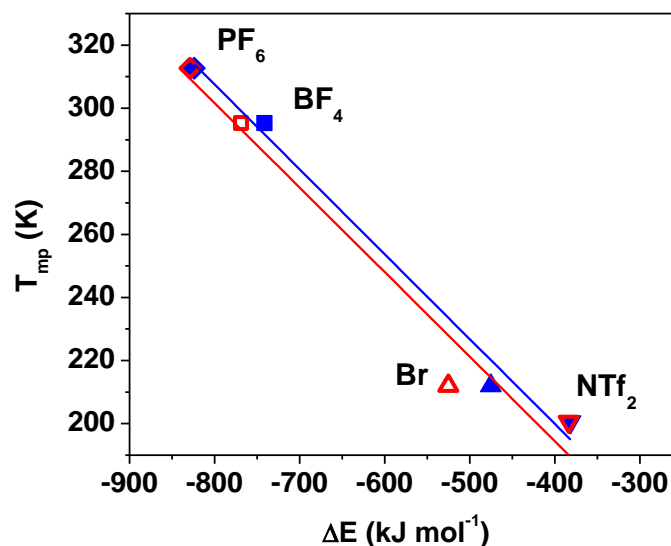


Figure 4.9 Relationship between the calculated interaction energy (ΔE) and the melting point (T_{mp}) of the phosphonium ILs. The melting points were taken from ref. [54]. The solid and open symbols are the calculated values using the BLYP and PW91 functionals, respectively.

4.4 CONCLUSIONS

We have carried out DFT calculations to obtain the electronic and molecular structures of six phosphonium-based ILs with a [P₁₄₆₆₆] cation paired to [Cl], [Br], [DCA], [BF₄], [PF₆] and [NTf₂] anions. The inter-ionic H-bond length and angle, the energy gap between HOMO and LUMO, the dipole moment (μ), the cation-anion interaction energy ($-\Delta E$), and the electrostatic potential were calculated for each IL. The wavelengths and oscillator strengths of vibrational and electronic transition lines of the ILs were also calculated and compared with measured IR and UV-Vis absorption spectra. The calculated spectral lines are in good agreement with those of the measured spectra.

We have found strong correlations between the calculated quantum chemical parameters and the measured physical and chemical properties of the phosphonium ILs. We have established that the molar conductivity increases, whereas the viscosity decreases, exponentially with dipole moment for the ILs, and the melting point increases linearly with $-\Delta E$.

4.5 REFERENCES

- [1] P. Wasserscheid, T. Welton, *Ionic Liquids in Synthesis*, Wiley-VCH, Weinheim (2003).
- [2] T. Welton, *Chem. Rev.*, 99 (1999) 2071.
- [3] D.R. MacFarlane, K.R. Seddon, *Aust. J. Chem.*, 60 (2007) 3.
- [4] H. Olivier-Bourbigou, L. Magna, D. Morvan, *Appl. Catal., A* 373 (2010) 1.
- [5] M.J. Earle, K.R. Seddon, *Pure Appl. Chem.*, 72 (2000) 1391.
- [6] S.E. Howett, J.M. Joseph, J.J. Noël, J.C. Wren, *J. Colloid and Interface Sci.*, 361 (2011) 338.
- [7] C.M.S.S. Neves, P.J. Carvalho, M.G. Freire, J.A.P. Coutinho, *J. Chem. Thermodyn.*, 43 (2011) 948.
- [8] K.J. Fraser, D.R. MacFarlane, *Aust. J. Chem.*, 62 (2009) 309.
- [9] R.E. Del Sesto, C. Corley, A. Robertson, J.S. Wilkes, *J. Organomet. Chem.*, 690 (2005) 2536.
- [10] R.D. Rogers, K.R. Seddon, Editors, *Ionic Liquids as Green Solvents: Progress and Prospects*, American Chemical Society, Washington, DC (2003).
- [11] P.A. Hunt, B. Kirchner, T. Welton, *Chem. Eur. J.*, 12 (2006) 6762.
- [12] P.A. Hunt, *J. Phys. Chem. B*, 111 (2007) 4844.
- [13] E.I. Izgorodina, U.L. Bernard, D.R. MacFarlane, *J. Phys. Chem. A*, 113 (2009) 7064.
- [14] R. Lü, H. Tangbo, Z. Cao, *J. Nat. Gas Chem.*, 16 (2007) 70.
- [15] R. Lü, S. Wang, Y. Lu, *Chem. Phys. Lett.*, 505 (2011) 87.
- [16] K.H. Liu, M. Pu, B.H. Chen, *Chinese J. Struct. Chem.*, 24 (2005) 576.
- [17] W. Li, X. Wu, C. Qi, H. Rong, L. Gong, *J. Mol. Struct.*, 942 (2010) 19.
- [18] S.P. Ong, G. Ceder, *Electrochim. Acta*, 55 (2010) 3804.
- [19] M. Shukla, N. Srivastava, S. Saha, *J. Mol. Struct.*, 975 (2010) 349.
- [20] M.G. Benavides-Garcia, M. Monroe, *Chem. Phys. Lett.*, 479 (2009) 238.
- [21] T. Fujimori, K. Fujii, R. Kanzaki, K. Chiba, H. Yamamoto, Y. Umebayashi, S. Ishiguro, *J. Mol. Liq.*, 131-132 (2007) 216.
- [22] S.A. Katsyuba, E.E. Zvereva, A. Vidiš, P.J. Dyson, *J. Phys. Chem. A*, 111 (2007) 352.
- [23] Y. Danten, M.I. Cabaço, M. Besnard, *J. Mol. Liq.*, 153 (2010) 57.
- [24] V.K. Verma, T. Banerjee, *J. Chem. Thermodyn.*, 42 (2010) 909.

- [25] A. Bagno, F. D'Amico, G. Saielli, *J. Mol. Liq.*, 131-132 (2007) 17.
- [26] C.E.R. Prado, L.C.G. Freitas, *J. Mol. Struct.*, 847 (2007) 93.
- [27] B.L. Bhargava, S. Balasubramanian, *J. Chem. Phys.*, 123 (2005) 144505.
- [28] C.J. Margulis, H.A. Stern, B.J. Berne, *J. Phys. Chem. B*, 106 (2002) 12017.
- [29] X. Liu, G. Zhou, S. Zhang, G. Yu, *Mol. Simul.*, 36 (2010) 79.
- [30] H.L. Ngo, K. LeCompte, L. Hargens, A.B. McEwen, *Thermochim. Acta*, 357-358 (2000) 97.
- [31] M.S.R.N. Accelrys Software Inc., Release 5.5, San Diego: Accelrys Software Inc., 2010.
- [32] A.D. Becke, *Phys. Rev. A*, 38 (1988) 3098.
- [33] C.T. Lee, W.T. Yang, R.G. Parr, *Phys. Rev. B*, 37 (1988) 785.
- [34] J.P. Perdew, Y. Wang, *Phys. Rev. B*, 45 (1992) 13244.
- [35] M. Ernzerhof, J.P. Perdew, K. Burke, *Top. Curr. Chem.*, 180 (1996) 1.
- [36] S.F. Sousa, P.A. Fernandes, M.J. Ramos, *J. Phys. Chem. A*, 111 (2007) 10439.
- [37] K.C. Lethesh, K. Van Hecke, L. Van Meervelt, P. Nockemann, B. Kirchner, S. Zahn, T.N. Parac-Vogt, W. Dehaen, K. Binnemans, *J. Phys. Chem. B*, 115 (2011) 8424.
- [38] R. Lü, Z. Qu, H. Yu, F. Wang, S. Wang, *Chem. Phys. Lett.*, 532 (2012) 13.
- [39] A. Bondi, *J. Phys. Chem.*, 68 (1964) 441.
- [40] G.A. Jeffrey, *J. Mol. Struct.*, 485 (1999) 293.
- [41] J. Aihara, *Phys. Chem. Chem. Phys.*, 2 (2000) 3121.
- [42] K. Fukui, T. Yonezawa, H. Shingu, *J. Chem. Phys.*, 20 (1952) 722.
- [43] D.K. Hazra, A.K. Mukherjee, M. Helliwell, M. Mukherjee, *Cryst. Eng. Comm.*, 14 (2012) 993.
- [44] G. Klopman, *J. Am. Chem. Soc.*, 90 (1968) 223.
- [45] H.J. Singh, U. Mukherjee, *J. Mol. Model.*, 19 (2013) 2317.
- [46] Z.X. Zhou, R.G. Parr, *J. Am. Chem. Soc.*, 112 (1990) 5720.
- [47] J. Kiefer, J. Fries, A. Leipertz, *Appl. Spectrosc.*, 61 (2007) 1306.
- [48] X.P. Xuan, M. Guo, Y.C. Pei, Y. Zheng, *Spectrochim. Acta A*, 78 (2011) 1492.
- [49] B.G. Evale, S.M. Hanagodimath, I.A. Khan, M. Kulkarni, *Spectrochim. Acta A*, 73 (2009) 694.
- [50] M.J. vanderBurgt, L.M.G. Jansen, A.H. Huizer, C.A.G.O. Varma, *Chem. Phys.*, 201 (1995) 525.
- [51] R.E. Ramirez, E.M. Sanchez, *Sol. Energ. Mat. Sol. C*, 90 (2006) 2384.
- [52] J.W. Vaughan, D. Dreisinger, J. Haggins, *ECS Trans.*, 2 (2006) 381.
- [53] S. Tsuzuki, W. Shinoda, H. Saito, M. Mikami, H. Tokuda, M. Watanabe, *J. Phys. Chem. B*, 113 (2009) 10641.
- [54] Cytec product sheet CYPHOS® IL 101, IL 102, IL 105, IL 109, IL 110, IL 111, <https://www.cytec.com/specialty-chemicals/ionicliquidstable.htm> <Accessed: February 26, 2013>.

Chapter 5

The Chemical Stability of Phosphonium-based Ionic liquids under Gamma Irradiation

5.1 INTRODUCTION

Ionic liquids have diverse physicochemical properties that make them candidates for use in many industrial applications including separation technologies [1-4]. Many ILs are known to be stable in high energy environments and they can be tailored to possess unique solvation properties for coordination and extraction of metal ions from aqueous solutions [5]. The stability of ionic liquids and their extraction capabilities thus make them attractive alternatives for use in separation processes in the nuclear industry (such as fuel processing and waste treatment). Currently such separations are done using organic solvents and organic extractants. For example, kerosene and dodecane are used in the PUREX process for nuclear fuel processing [6]. Prior to use in nuclear applications where high ionizing radiation fields are present, the radiation stability of candidate ionic liquids must be understood.

This chapter presents a study on the effects of γ -radiation on the physicochemical and ion transport properties of phosphonium-based ILs. Five phosphonium ILs that have different physical properties, such as hydrophobicity, viscosity, and conductivity (Table 5.1), were studied. Three of these ILs were the subject of the DFT calculations presented in Chapter 4. They are hydrophobic ILs with a long alkyl organic chain cation (tetradecyl(trihexyl)phosphonium or $[P_{14666}]$) paired with a different anion: bromide $[Br]$,

bis(trifluoromethylsulfonyl) imide [NTf₂], or dicyanamide [DCA], Figure 5.1. The two other ILs studied were water soluble ILs containing a cation with a shorter alkyl chain (tributylmethylphosphonium or [P₄₄₄₁]) or a short branched alkyl chain (triisobutylmethylphosphonium or [PTiBMe]). For these ILs the paired anions are polyoxygenated ions, methy sulfate [MeSO₄] and tosylate [TsO] respectively.

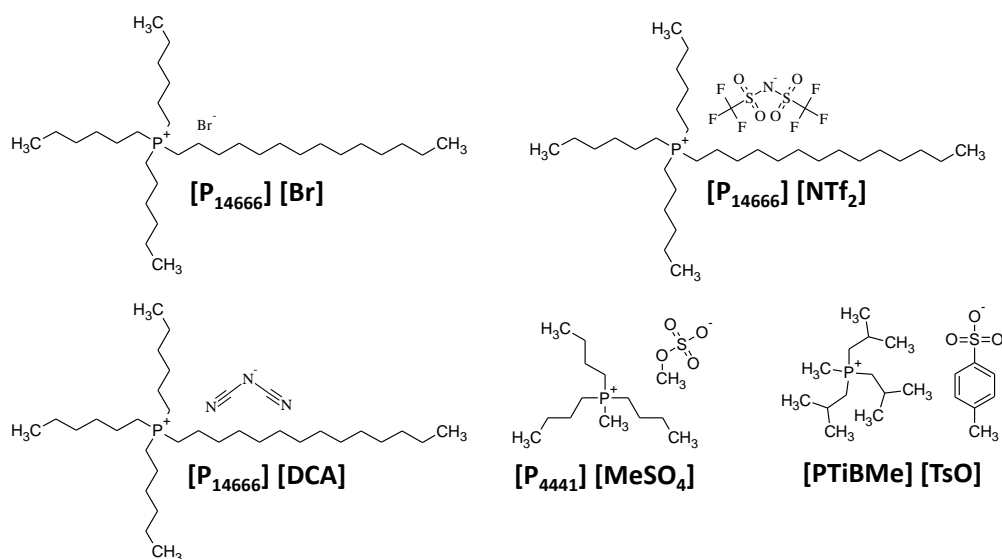


Figure 5.1 Structures of the phosphonium ionic liquids used in this study.

Table 5.1 The physical properties of the ionic liquids investigated (T = 25 °C).

Ionic Liquid	[P ₁₄₆₆₆] [Br]	[P ₁₄₆₆₆] [NTf ₂]	[P ₁₄₆₆₆] [DCA]	[P ₄₄₄₁] [MeSO ₄]	[PTiBMe] [TsO]
Density (g/ml) [7]	0.9546	1.0652	0.8985	1.0662	1.07
Viscosity (cP) [7]	2094	292.5	280.4	409.3	Not available
Conductivity (μS/cm)	9	108	216	862	92
Miscible with Water [7]	No	No	No	Yes	Yes
Melting Point (°C) [7]	-61	-72	Not available	Not available	45
Solubility of H ₂ O (wt.%) [8]	6.720	0.225	3.407	highly soluble	highly soluble

5.2 EXPERIMENTAL

5.2.1 Materials and Sample Preparation

All five ILs used in this study were purchased from Sigma-Aldrich, were of the highest purity available (> 95%) and were used as received. Ionic liquid samples for irradiation were prepared by placing 2 ml of IL inside a 10 ml pyrex vial (Agilent Technologies). The test vials were prepared inside an argon (Praxair, 99.99% purity) purged glove box to create a deaerated IL system and were sealed with aluminum crimp caps with PTFE/silicone septa. Multiple vials were prepared for tests with different irradiation times.

5.2.2 Test Vial Irradiation and Analysis

Irradiation was carried out in a ^{60}Co gamma cell (MDS Nordion) which provided the irradiation chamber with uniform absorption dose rate of $4.0 \text{ kGy}\cdot\text{h}^{-1}$ (in water) within the vial volume. The samples were irradiated for 96 and 192 h providing a total dose of 384 and 768 kGy, respectively.

After the radiation exposure the gas in the headspace of the sample vials was analyzed using gas chromatography with a mass spectrometer detector (GC-MS). The IL phase was analyzed for optical and structural changes by UV-Vis, Fourier transform infrared (FTIR) and Raman spectroscopy. The conductivity of the IL was also measured using electrochemical impedance spectroscopy (EIS). Full details on the analyses conducted are discussed in Section 3.3 of the experimental chapter.

5.3 RESULTS AND DISCUSSION

5.3.1 Background on the Interaction of a γ -Photon with an IL

The interaction of ionizing radiation with a liquid medium, in particular water, has been described by various authors [9-16]. Briefly, the initial interaction of a γ -photon with a molecule or an atom in the medium causes Compton scattering which ejects an energetic electron from a molecule. The most probable Compton scattering yields near 100 % energy transfer from the photon to the electron. Thus, the Compton scattered electron has a kinetic energy similar to that of the γ -photon (1.173 and 1.332 MeV from the ^{60}Co decay). This high-energy electron (or the primary electron) undergoes a series of inelastic collisions with the electrons bound in molecules or atoms on its track before it loses most its energy (the probability of the high energy electron colliding with nuclei is negligible). The collision of the primary electron is indiscriminant, i.e., the collisional cross section does not depend on the atomic and chemical structure of the interacting matter, but only on the density of electrons in the matter. (Since the number of bound electrons in a molecule is nearly proportional to the mass of the molecule (except for the H atom), the radiation energy absorption by a medium is nearly proportional to its density.) Each inelastic collision induces ionization or electronic excitation of the target atom/molecule. The secondary electron ejected from an ionization event may have enough energy to ionize or excite a neighbouring molecule and hence two or three electron-ion pairs and/or excited molecules can cluster around each collision site (these clusters are referred to as spurs).

The charged or excited species formed in a spur have sufficient kinetic energy to permit the ejected electrons to move away from the Coulombic influence of their counter

ions and the spur expands. The chemical effect that ionizing radiation induces in an interacting medium depends not only on the energy transfer rate from the primary electron to the medium described above, but, more importantly, on the inter- and intramolecular energy transfer processes of the ions and excited species. The molecular energy transfer determines the fraction of the absorbed radiation energy that is used for bond dissociation. The larger the molecule, the higher its density of rotational and vibrational energy states and the lower the probability of bond dissociation the molecule has. Furthermore, as the spurs expand the electrons and ions and the dissociated products can undergo geminate recombination due to the Coulombic attraction described above. The probability of escaping geminate recombination to become free ions or free radicals (free from the counter ions and radicals) is low in a low dielectric medium such as an organic solvent or an IL compared to high-dielectric medium like water [17, 18]. The molecular energy transfer and geminate recombination processes that occur while the spur is expanding depend strongly on the molecular mass and the charge transport properties of the medium.

Once escaping a spur into the bulk phase the free radicals and free ions are available to undergo the homogeneous chemical reactions with whatever species are present in solution. Under continuous irradiation, the free radicals (and ions) are continuously formed but, the homogeneous reactions in the bulk-phase lead to the formation of more stable molecular products. The rate of formation of the stable products may increase linearly with absorbed radiation dose, or may reach steady state. The latter occurs if the free radicals and ions created react to reform the original solvent molecules [14]. The liquid-phase chemical reaction rate not only depends strongly on the

concentrations of reactants but also the transport properties (such as diffusion and ion mobility) of the reactants in the medium. Since the processes occurring during the spur expansion and the subsequent bulk phase reactions depend on the molecular and transport properties of the medium, the net radiolytic decomposition yield of an IL following irradiation will be very different from that of water and it will vary from one IL to another.

5.3.2 Airborne Radiolysis Products

The airborne radiolysis products observed in the headspace after irradiation for different times for the five ILs are listed in Table 5.2. The table includes previously reported products observed after 8 h irradiation [19, 20]. In addition to the products listed in the table, there were a few minor peaks in the GC-MS spectra that were not identified. Note that the 8-h irradiation of [P₁₄₆₆₆] [DCA] resulted in dichloromethane in the gas phase. We attribute the presence of this species not to the radiolytic decomposition of the IL, but to the presence of dichloromethane solvent residue used in the synthesis of the IL [21, 22] (the ILs were used as received). This species was not observed in longer irradiation experiments. It was difficult to quantify the concentrations of the organic species observed in the headspace in our study. However, the concentrations of the airborne species generally increased with irradiation time. It should be emphasized that non-volatile radiolytic decomposition products, if formed, would not be detected in the headspace.

Most of the airborne decomposition products are small organic molecules having carbon chain length less than 8-C. The absence of longer carbon-chain compounds in the

headspace may be due to either their low radiolytic yield or their low volatility.

Interestingly we did not observe any 1-C or 2-C compounds, except for CHF_3 and C_2F_6 from $[\text{P}_{14666}] [\text{NTf}_2]$.

Table 5.2 The major radiolytic decomposition products of ionic liquids detected in the gas phase using GC-MS.

Ionic Liquids	8 h Rad from reference [19, 20]	92 h Rad	192 h Rad
$[\text{P}_{14666}] [\text{Br}]$	hexane (C_6H_{14}) hexene (C_6H_{12})	hexane (C_6H_{14})	hexane (C_6H_{14}) hexene (C_6H_{12}) propane (C_3H_8)
$[\text{P}_{14666}] [\text{NTf}_2]$	ethane (C_2H_6) hexane (C_6H_{14}) hexafluoroethane (C_2F_6) fluoroform (CHF_3)	hexane (C_6H_{14}) fluoroform (CHF_3) propane (C_3H_8)	hexane (C_6H_{14}) fluoroform (CHF_3) hexafluoroethane (C_2F_6)
$[\text{P}_{14666}] [\text{DCA}]$	dichloromethane (CH_2Cl_2)	hexane (C_6H_{14})	hexane (C_6H_{14}) hexene (C_6H_{12})
$[\text{P}_{4441}] [\text{MeSO}_4]$	No Data	butane (C_4H_{10}) pentane (C_5H_{12}) propane (C_3H_8)	butane (C_4H_{10}) pentane (C_5H_{12}) propane (C_3H_8) octane (C_8H_{18})
$[\text{PTiBMe}] [\text{TsO}]$	isobutylene (C_4H_8) toluene ($\text{C}_6\text{H}_5\text{CH}_3$)	isobutane (C_4H_{10}) isobutylene (C_4H_8) propane (C_3H_8) propene (C_3H_6)	isobutane (C_4H_{10}) isobutylene (C_4H_8) toluene ($\text{C}_6\text{H}_5\text{CH}_3$) propane (C_3H_8) propene (C_3H_6)

These observations are consistent with the expectations arising from the bond strengths and the stabilities of the free radicals produced from the radiolytic dissociation of the ILs. In the cation moiety $[\text{P}_{14666}]$ the P – C bond is weaker than the C – C bond,

and the cation dissociation product is an organic carbon radical. The organic radical stability increases in the order: methyl < primary < secondary < tertiary [23-25]. Thus, the net radiolytic decomposition of [P₁₄₆₆₆] mainly leads to the formation of hexane radical, •C₆H₁₃, which then either abstracts or donates •H to a neighbouring molecule and forms stable hexane (C₆H₁₄) or hexene (C₆H₁₂) and H₂.

On the other hand, the radiolytic decomposition of [P₄₄₄₁] and [PTiBMe] mainly lead to the formation of butyl and isobutyl radicals (•C₄H₉), respectively. For [P₄₄₄₁] which contains normal alkyl chains, the butyl radical undergoes •H abstraction to form butane, dimerizes to form octane (C₈H₁₈), or disproportionates to form pentane (C₅H₁₂) and propane (C₃H₈). However, no significant formation of butene was observed since the formation of a double C = C bond is less favourable for short normal alkyl chains. For [PTiBMe], the isobutyl radicals form isobutylene (C₄H₈) as well as isobutane (C₄H₁₀). The [P₄₄₄₁] and [PTiBMe] moieties also have a 1-C branch attached to the phosphonium ion. However, the formation of methyl radical (•CH₃) is less likely due to the lower stability of the primary carbon radical compared to that of the secondary carbon radical. We did not observe any 1-C and 2-C compounds, confirming that the C – C bond cleavage is effective.

In all of the ILs studied a higher concentration of propane was observed with a longer irradiation time, indicating that the organic products continue to undergo further radiolytic decomposition. Although the production of propane in the IL phase may be lower than the production rates of 4-C or 6-C products, propane has a higher vapour pressure and hence is easier to become airborne [26] (we may not have full equilibrium between the gas and liquid phases in our vials).

Gamma-irradiation also induces dissociation of polyatomic anions: the fluoroform radical ($\bullet\text{CF}_3$) is formed from $[\text{NTf}_2]$ and the toluene radical ($\bullet\text{C}_6\text{H}_4\text{CH}_3$) is formed from $[\text{TsO}]$. These radicals then further react to form CHF_3 and C_2F_6 , and toluene ($\text{C}_6\text{H}_5\text{CH}_3$), respectively. No airborne products from the anions were observed following irradiation of the ILs containing $[\text{Br}]$, $[\text{DCA}]$ and $[\text{MeSO}_4]$. Again these observations are consistent with the stabilities of the potential radical products of the anions. The stability of a free radical decreases when the hybridization of the carbon goes from sp^3 to sp^2 to sp [24]. Thus, it is harder to induce cleavage of the C – N bond of $[\text{DCA}]$ and form $\bullet\text{C} \equiv \text{N}$, and no airborne products associated with this radical was observed. On the other hand, the cleavage of C – S bond of $[\text{TsO}]$ that leads to the formation of $\bullet\text{C}_6\text{H}_4\text{CH}_3$ is more favourable due to the stabilization of that radical by resonance [24, 25, 27]. The radiolysis products, CHF_3 and C_2F_6 , from $[\text{P}_{14666}] [\text{NTf}_2]$ are also observed by Le Rouzo et al. following irradiation of butylmethylimidazolium ILs containing the $[\text{NTf}_2]$ anion [28].

5.3.3 Spectroscopic Analyses of the IL Phases

The changes in the ILs due to γ -radiation were examined by a range of spectroscopic analyses and conductivity measurements. The UV-Vis absorption, FTIR and Raman spectroscopic analysis results are presented in Figures 5.2 to 5.6 in this section. The conductivity results are discussed in Section 5.3.4. In presenting the spectroscopic analysis results, the ILs are grouped: (1) the ILs containing the $[\text{P}_{14666}]$ cation but different anions and (2) the ILs containing cations with shorter alkyl chains, $[\text{P}_{4441}] [\text{MeSO}_4]$ and $[\text{PTiBMe}] [\text{TsO}]$.

5.3.3.1 The $[P_{14666}]$ ILs

The colour of $[P_{14666}]$ [Br] changed from pale yellow to a darker yellow with increasing irradiation time (Figure 5.2). The corresponding UV-Vis, FTIR and Raman spectra of the IL are shown in Figure 5.2. The UV-Vis spectrum of the un-irradiated $[P_{14666}]$ [Br] shows a main peak near 290 nm with two minor peaks near 350 nm and 475 nm. Since this IL does not have a polyatomic anion, it is safe to assign these absorption

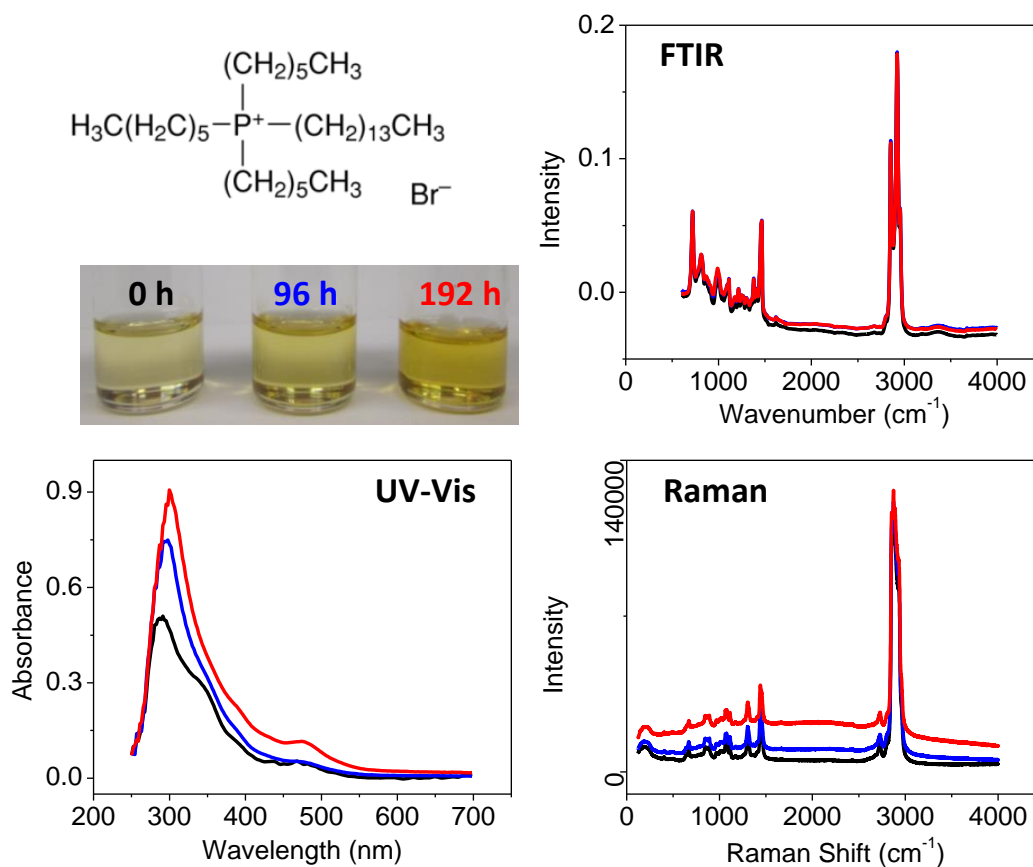


Figure 5.2 Photographs of irradiated $[P_{14666}]$ [Br] and the corresponding UV-Vis, FTIR and Raman spectra as a function of irradiation time. Black, blue and red lines are at 0, 96 and 192 h, respectively.

bands to electronic transitions of the IL cation moiety although the anion can affect the transition probabilities. The main absorption band with a peak at 290 nm shows an increase in absorption intensity with irradiation time, but no significant broadening of the band or red shift of the peak was observed. (When the peak intensity was normalized with respect to the peak height, the absorption band with a peak at 290 nm shows the same profile for irradiated and un-irradiated samples.) This absorption band is also observed for [P₁₄₆₆₆] [NTf₂] (see Figure 5.3 later). We have not been able to assign this band to any specific electronic transition, but suspect that the probability of this transition is increased due to change in the cation configuration around the radiolytically-formed small organic molecules, see further discussion later.

The corresponding FTIR and Raman spectra did not show any new peaks or relative changes in their intensities, except for small increase in the broad background band intensity in the Raman spectrum. This broad background band was present and its intensity increased with irradiation in the Raman spectra of the all three [P₁₄₆₆₆] ILs studied, albeit with different intensities, see below.

The [P₁₄₆₆₆] [NTf₂] IL is colourless prior to irradiation but slowly become yellowish with irradiation (Figure 5.3). The UV-Vis spectrum of the un-irradiated IL shows only a single, small absorption band near to 290 nm, the same location as a band observed for [P₁₄₆₆₆] [Br] (Figure 5.2). The presence of only one band is consistent with the DFT analysis presented in Chapter 4. That calculation predicts that there is a smaller number of allowed electronic transitions in this wavelength range for [P₁₄₆₆₆] [NTf₂] compared to [P₁₄₆₆₆] [Br] [29]. As observed for [P₁₄₆₆₆] [Br], the intensity of the 290 nm absorption band increased with irradiation time. Although we see the radiolytic

decomposition products, CHF_3 and C_2F_6 , from the anion moiety $[\text{NTf}_2]$ in the headspace, these molecules do not absorb light at wavelengths > 250 nm and hence we did not see any UV absorption corresponding to these products.

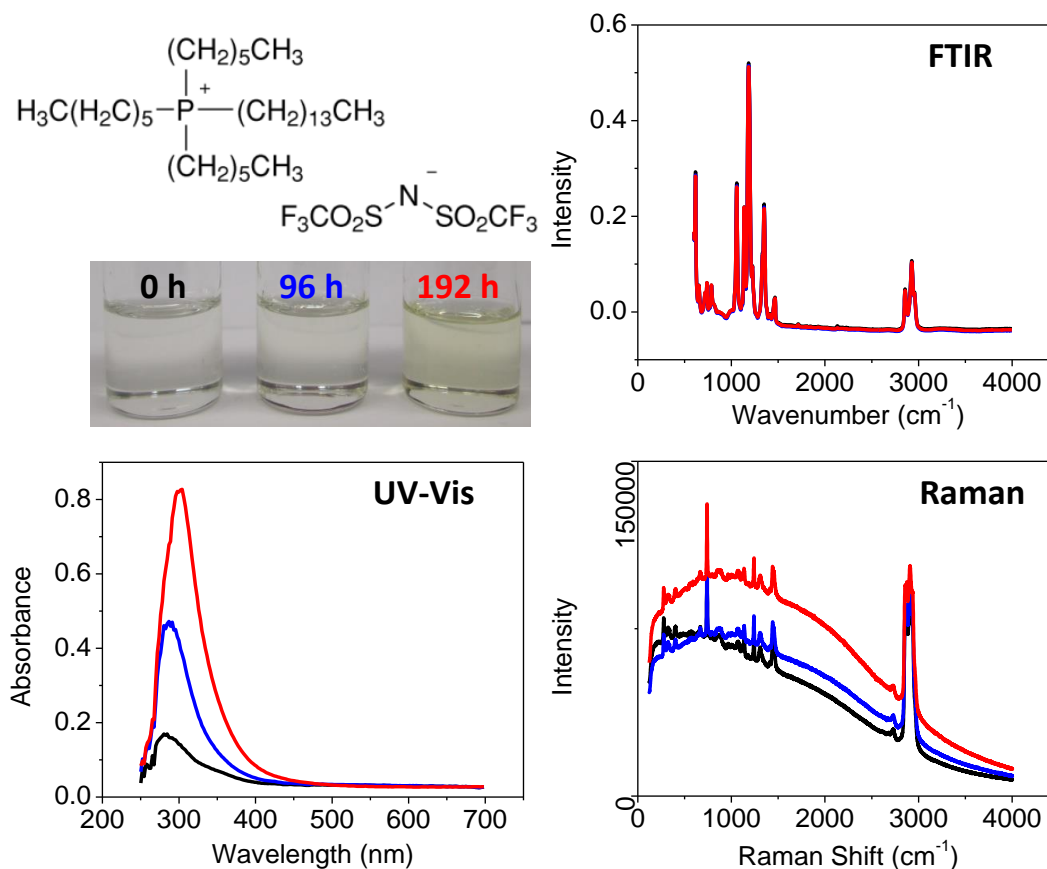


Figure 5.3 Photographs of irradiated $[\text{P}_{14666}] [\text{NTf}_2]$ and the corresponding UV-Vis, FTIR and Raman spectra as a function of irradiation time. Black, blue and red lines are at 0, 96 and 192 h, respectively.

The observed increase in the intensity of the 290 nm band with irradiation time for both $[\text{P}_{14666}] [\text{NTf}_2]$ and $[\text{P}_{14666}] [\text{Br}]$ is consistent with the suggestion that the probability of this transition may be increased due to change in the configuration of the IL molecules around the radiolytically formed small organic molecules.

No changes in the rotational-vibrational transition peaks in the corresponding FTIR and Raman spectra were observed for either IL as a function of irradiation time. The main difference observed between the two ILs is that the scattering background is higher in the Raman spectrum of [P₁₄₆₆₆] [NTf₂] compared to the spectrum of [P₁₄₆₆₆] [Br]. The viscosity of [P₁₄₆₆₆] [NTf₂] is significantly smaller than that of [P₁₄₆₆₆] [Br] and a change in the cation configuration may be easier in [P₁₄₆₆₆] [NTf₂] than in [P₁₄₆₆₆] [Br].

The [P₁₄₆₆₆] [DCA] IL shows the most colour change when irradiated, going from pale yellow to yellow and then to dark orange (Figure 5.4). The main UV-Vis absorption band for this IL has a peak at ~305 nm, a slightly longer wavelength compared to the main absorption bands observed for [P₁₄₆₆₆] [Br] and [P₁₄₆₆₆] [NTf₂]. This shift was predicted by the DFT calculations presented in Chapter 4. The UV-Vis spectra of [P₁₄₆₆₆] [DCA] also show an additional absorption band near 370 nm whose intensity is very small for the un-irradiated IL. While the intensity of the 305 nm band does not change significantly, the intensity of the 370 nm band increases dramatically after 96 h and 192 h irradiation. As for the other ILs, no additional peaks or changes in the relative intensities of the sharp, well-defined FTIR peaks were observed after irradiation. However, the intensity of the broad Raman scattering band increased the greatly with irradiation for [P₁₄₆₆₆] [DCA] compared to the other two ILs.

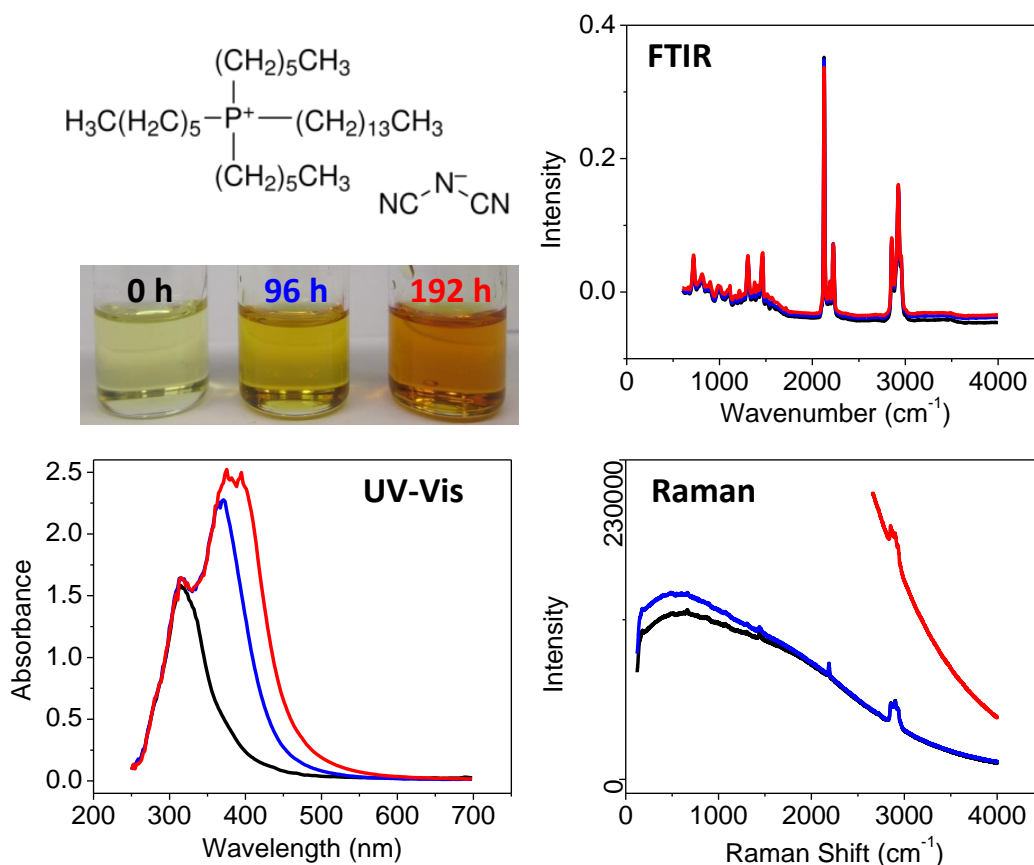


Figure 5.4 Photographs of irradiated $[P_{14666}] [DCA]$ and the corresponding UV-Vis, FTIR and Raman spectra as a function of irradiation time. Black, blue and red lines are at 0, 96 and 192 h, respectively.

The airborne radiolytic decomposition products observed for this IL are the same as those for $[P_{14666}] [Br]$. No obvious radiolytic decomposition products from the $[DCA]$ anion were observed (Table 5.2). Nevertheless, the growth of the UV-Vis absorption band near 370 nm suggests that the probability of this transition has been greatly altered as a result of irradiation. Again, we suspect that this is due to a change in the configuration of the IL molecules around radiolytically-formed small organic molecules.

All of the three [P₁₄₆₆₆] ILs studied show increases in the intensity of one of the UV-Vis bands, the 290 nm band for [P₁₄₆₆₆] [Br] and [P₁₄₆₆₆] [NTf₂] and the 370 nm band for [P₁₄₆₆₆] [DCA]. Accompanying these changes are the changes in the broad band Raman scattering intensity. Comparison of these band intensities of the three [P₁₄₆₆₆] ILs provides an interesting observation. In Raman spectra of the un-irradiated ILs the scattering intensity of the broad band is larger in the order; [P₁₄₆₆₆] [Br] (negligible) < [P₁₄₆₆₆] [NTf₂] < [P₁₄₆₆₆] [DCA] (largest), whereas the UV-Vis absorbance is larger in the order; [P₁₄₆₆₆] [NTf₂] < [P₁₄₆₆₆] [Br] < [P₁₄₆₆₆] [DCA] (largest). For the un-irradiated samples, the order of the UV-Vis absorbance near 350 nm (blue) is more closely associated with the order of the intensity of the colour change, [P₁₄₆₆₆] [NTf₂] (colourless) < [P₁₄₆₆₆] [Br] < [P₁₄₆₆₆] [DCA] (most yellowish). This change is consistent with an increase in the absorbance in the blue wavelength range (< 400 nm) should result in the solution having a more intense yellow colour.

The Raman scattering intensity of the broad band increases with irradiation for all three ILs. However, the increase is more pronounced near 2000 cm⁻¹ for the [Br] and [NTf₂] ILs, whereas it is more pronounced near 500 cm⁻¹ for the [DCA] IL. The increase in the broad band Raman scattering is modest after 96 h irradiation but is more pronounced after 192 h irradiation; the effect is not linear with irradiation dose. On the other hand, the UV-Vis absorbance appears to increase nearly proportionally with irradiation time. (Note that in some cases the absorbance measured was so high (> 2.0) that the absorbance was no longer proportional to the concentration of the chromophore.) Nevertheless, the increases in the intensities of both the UV-Vis and the Raman bands are in the order:



This is the same order as the intensities of the Raman broad band of the un-irradiated samples. Comparison of the physical properties of the ILs (Table 5.1) shows that the order follows the order for the conductivity and the inverse order for the viscosity of the ILs.

These observations are consistent with the increasing numbers of IL molecules with configurational changes (or aggregation) as the small organic radiolysis products accumulate. These small organic molecules can provide hydrophobic sites that promote aggregation of the long organic chains and for the centres of micelles [19]. This can strengthen the ionic bond (or the Coulombic attraction) between the cation and anion centres. Light scattering is enhanced with the increase in the concentration of the aggregates or micelles, increasing the broad band Raman scattering intensity. The aggregation of IL molecules occurs more easily in a less viscous IL. The configurational changes can have a strong effect on the electronic transition probabilities between different energy states. The net radiolytic decomposition of IL is small because the quantity of small organic species that is produced is too small to be observed in the FTIR and Raman spectra of irradiated ILs. But the effect of small numbers of such species is magnified by their ability to cause the aggregation of large numbers of IL molecules and change the UV absorbance quite noticeably.

5.3.3.2 Short Carbon Chain ILs

Gamma-irradiation of $[\text{P}_{4441}] [\text{MeSO}_4]$ shows no significant colour change (Figure 5.5). The UV-Vis spectra show a band at 250 nm that increases in intensity after

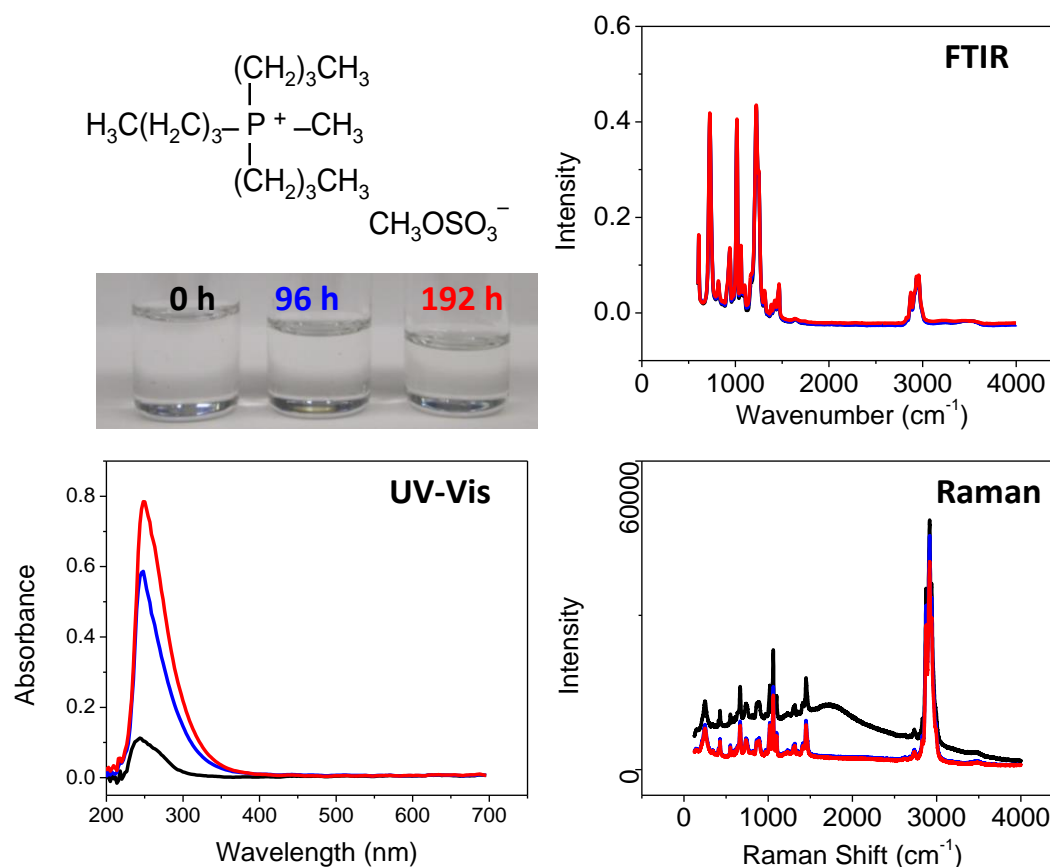


Figure 5.5 Photographs of irradiated [P₄₄₄₁] [MeSO₄] and the corresponding UV-Vis, FTIR and Raman spectra as a function of irradiation time. Black, blue and red lines are at 0, 96 and 192 h, respectively. The blue and red lines are heavily overlapping for the Raman and FTIR spectra.

irradiation. However, this IL has no significant absorbance at wavelengths longer than 350 nm and hence it remains colourless, even after irradiation. Like the [P₁₄₆₆₆] ILs the FTIR and Raman spectra of this IL also show no additional peaks or changes in the relative intensities of the sharp and distinct peaks. Unlike the [P₁₄₆₆₆] ILs where irradiation increases the Raman broad band scattering, the [P₄₄₄₁] [MeSO₄] initially has a broad peak at $\sim 1700\text{ cm}^{-1}$ which disappeared after 96 h of irradiation. This peak is attributed to water impurities in the IL [19, 30, 31]. This IL is miscible with water so the

presence of dissolved water as an impurity is very likely. The water absorbed in the IL may have evaporated during long-term irradiation.

The absence of a broad Raman scattering band for this IL can be explained by the much shorter hydrocarbon chains in the cation of this IL. Aggregation of the cations with short organic chains around the radiolytically-produced small organic molecules is less likely to occur compared to the [P₁₄₆₆₆] ILs. The absence of these aggregates (or micelles) leads to an absence of the Raman band.

The colour of un-irradiated [PTiBMe] [TsO] is colourless; it changes to pale yellow with exposure to radiation (Figure 5.6). The UV-Vis absorption spectrum of the un-irradiated IL has peaks at 250 nm and 275 nm, like the 250 nm peak of the [P₄₄₄₁] IL and shorter in wavelength than the peaks observed for the [P₁₄₆₆₆] ILs. The shorter wavelengths for the peaks of the [P₄₄₄₁] and [PTiBMe] ILs are consistent with the expectation of larger HOMO-LUMO energy gaps for the shorter carbon chained compounds. The UV-Vis absorption spectra of the irradiated [PTiBMe] IL show small increases in the bands at 250 nm and 275 nm with increased irradiation and the appearance of an additional peak at around 300 nm. Like all of the other ILs, the FTIR and Raman spectra of this IL show no significant difference with irradiation time. Like the [P₄₄₄₁] IL, there is a broad Raman scattering band with intensity that disappeared with irradiation. As for [P₄₄₄₁] [MeSO₄] this IL is also miscible with water and a microemulsion of water impurities could have produced the scattering background.

The reason for the appearance of the new UV-Vis absorption band in the spectra of irradiated [PTiBMe] IL is not known. The reason for the appearance of additional

bands in the UV-Vis spectra of the [P₁₄₆₆₆] ILs due to configurational changes around small organic molecules does not appear to be valid for this IL because of the absence of a broad Raman band. As discussed for the [P₄₄₄₁] [MeSO₄] IL, aggregation of [PTiBMe] around radiolytically-produced small organic molecules is not favoured.

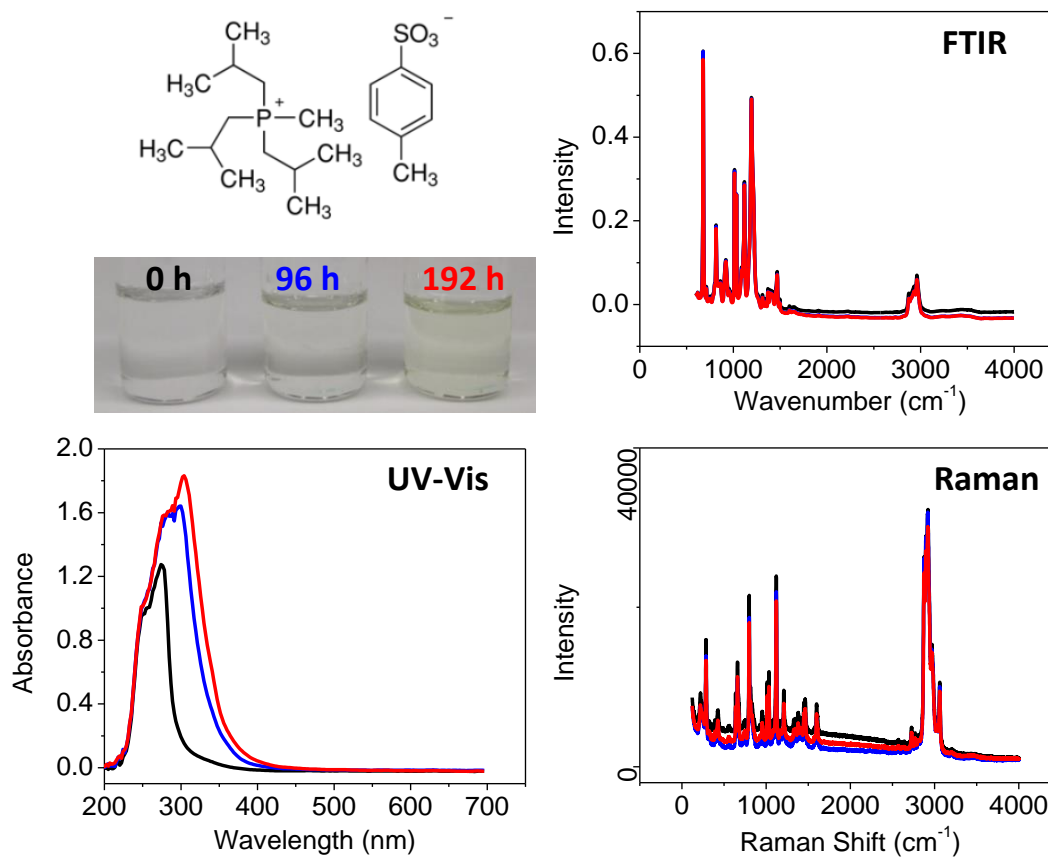


Figure 5.6 Photographs of irradiated [PTiBMe] [TsO] and the corresponding UV-Vis, FTIR and Raman spectra as a function of irradiation time. Black, blue and red lines are at 0, 96 and 192 h, respectively.

5.3.4 Conductivity

The changes in the conductivities of the ILs as a function of irradiation time are shown in Figure 5.7. The conductivity of an IL with an initially low conductivity or a higher viscosity, such as [P₁₄₆₆₆] [Br] and [PTiBMe] [TsO], showed no significant changes with irradiation time. On the other hand, the conductivity of an IL with an initially high conductivity decreases with irradiation time constantly. After 192 h irradiation, the conductivity of the water soluble [P₄₄₄₁] [MeSO₄] IL decreased by about 50% (from 862 to 446 $\mu\text{S}\cdot\text{cm}^{-1}$) whereas the conductivity of the hydrophobic [P₁₄₆₆₆] [DCA] IL decreased by only about 25% (from 216 to 161 $\mu\text{S}\cdot\text{cm}^{-1}$).

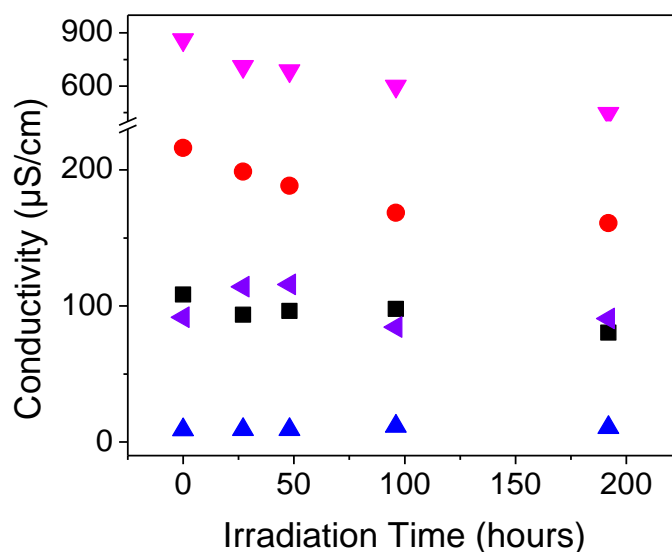


Figure 5.7 Conductivities of phosphonium ILs as a function of irradiation time: ● [P₁₄₆₆₆] [DCA], ▲ [P₁₄₆₆₆] [Br], ■ [P₁₄₆₆₆] [NTf₂], ▼ [PTiBMe] [TsO] and ▼ [P₄₄₄₁] [MeSO₄].

The increase in conductivity of a less conductive IL induced by γ -radiation can be attributed to the radiolytic production of small organic compounds. The conductivity of an electrolyte is known to be inversely proportional to the viscosity of the medium according to the Walden's law [32]. The conductivity of an IL, in particular highly viscous ILs, is known to deviate from Walden's law due to significant ion pairing and the addition of small organic molecules to a highly viscous IL is known to increase its conductivity [32-34].

As the concentration of small organic compounds increases in an IL, the IL molecules reorient themselves around these organic molecules. The IL cations with long organic chains form micelle-like structures and rearrange themselves such that their ion pairing is strengthened, as noted earlier. Such configurational changes in the IL would reduce the mobility of the cations and anions of the IL molecules. This has the effect of lowering the conductivity of the IL, as we have seen.

5.3.5 Comparison with Other Studies on the Irradiation of ILs

Previous studies on the effect of γ -radiation on imidazolium-based ILs have also reported on the increase in the UV-Vis absorbance due to irradiation [35-40]. In these studies the increase in absorbance was attributed to the formation of radiolysis products that have stronger light absorption than the original IL molecule.

In this study on phosphonium-based ILs, the radiolytic products in the ILs are most likely to be small organic compounds based on the species observed in the gas phase. These species arise from the P – C bond dissociation. These small organic

compounds do not absorb light at wavelengths > 250 nm and are more likely to absorb light at even shorter wavelengths than the larger original IL. Radiolysis could create radicals on the chains still attached to the central P atom and these radicals could combine through polymerization of the organic chains. If this occurred to any great extent we would expect to see broadening of the peaks in the FTIR and Raman spectra, but we did not observe any significant broadening of the rotational-vibrational peaks. The low gas phase concentrations of species in the gas phase and the negligible changes in the FTIR and Raman spectra indicate that the net radiolytic decomposition of the ILs studies here is very low even after 192 h irradiation at $4.0 \text{ kGy}\cdot\text{h}^{-1}$ (for a total radiation dose of 0.768 MGy).

Despite the low level of radiolytic decomposition, we do see changes in the UV-Vis spectra. We believe that this is due to the amplification of the impact of very small quantities of small organic species by the configuration changes that they induce in large quantities of ILs. The configurational changes affect the electronic transition probabilities, due to the Franck-Condon principle [41, 42].

It has also been reported by others that γ -radiation of an IL induces a colour change when there is negligible radiolytic chemical decomposition [35-40]. These studies attributed the radiation-induced colour changes to the creation of F-centers or the formation of a new species [40, 43-45]. F-centers are crystallographic defects in which an anionic vacancy in a crystal is filled by one or more electrons [43-45]. The electrons in the anion vacancies diffuse to fill the vacant sites and can absorb visible light. F-centers occur in salt crystals, particularly metallic oxides, when heated or irradiated [43, 44]. Solvated or hydrated electrons in a liquid phase also show a similar light absorption

capability; the hydrated electron absorbs light at around 720 nm and this light absorption property is extensively employed in the study of radiation-induced chemistry in water or organic solvents [14, 46]. Studies on water and organic species radiolysis have also shown that the lifetime of the solvated electrons in liquid phases is very short due to its high chemical reactivity (a lifetime of less than 1 ms in neutral water at 25 °C) [47]. It is possible that radiolysis of an IL liberates an electron that could be ‘solvated’ by the IL to behave like a quasi F-center. Although the lifetime of a ‘solvated’ electron in more viscous ILs might be expected to be longer than the typical lifetime of a solvated electron in water, it is difficult to imagine that quasi F-centers or ‘solvated’ electrons could survive for very long times in an irradiated IL. In our experiments the colour induced by radiation did not change even during a long-term storage (weeks) at room temperature after the irradiation period had ended. Hence we do not believe that quasi F-centers exist in our ILs.

5.4 SUMMARY

The effects of γ -radiation on the physicochemical and ion transport properties of phosphonium-based ILs were investigated. Five ILs that have different physical properties of hydrophobicity, viscosity and conductivity were studied. Airborne radiolysis product analysis was performed using GC-MS, and the IL phase was analysed using UV-Vis, FTIR and Raman spectroscopy, and conductivity measurement.

Gamma irradiation does not induce substantial chemical decomposition of the IL molecules into smaller fragments. Only minute quantities of airborne decomposition products were detected. These were small organic species which was formed mostly

from the radiolytic dissociation of the P – C bond in the cation moiety. The nature of the organic species depends on the cation's alkyl chains. Colour change was observed in most of the ILs with irradiation. Ionic liquids [P₁₄₆₆₆] [Br] and [P₁₄₆₆₆] [DCA] changed from pale yellow to yellow and dark orange, respectively while [P₁₄₆₆₆] [NTf₂] and [PTiBMe] [TsO] changed from colourless to slightly pale yellow. No significant colour change was seen in [P₄₄₄₁] [MeSO₄]. The UV-Vis analysis of the ILs corroborates the observed colour changes. Increases in the number and intensity of the UV-Vis peaks with irradiation are attributed to an increase in the probability of electronic transitions caused by the rearrangement in the IL configuration around the radiolytically-formed small organic molecules, and not due to the creation of a new chromophore. The FTIR and Raman analyses contain no additional peaks or changes in the relative intensities of the sharp and distinct peaks that are seen in an irradiated IL, confirming that the concentrations of radiolytic products is very low. The conductivity of the ILs changes over irradiation time. Those ILs with and initially low conductivity ([P₁₄₆₆₆] [Br] and [PTiBMe] [TsO]) see increases initially in their conductivity but then the conductivity decreases after longer irradiation times. The ILs with initially higher conductivities ([P₄₄₄₁] [MeSO₄], [P₁₄₆₆₆] [DCA] and [P₁₄₆₆₆] [NTf₂]), see their conductivities drop continuously with increasing irradiation.

5.5 REFERENCES

- [1] A. Heintz, *J. Chem. Thermodyn.*, 37 (2005) 525.
- [2] R.D. Rogers, K.R. Seddon, Editors, *Ionic Liquids as Green Solvents: Progress and Prospects*, ACS, Washington, DC (2003).
- [3] J.F. Wishart, *Energy Environ. Sci.*, 2 (2009) 956.
- [4] H. Zhao, S.Q. Xia, P.S. Ma, *J. Chem. Technol. Biotechnol.*, 80 (2005) 1089.
- [5] S. Dai, Y.H. Ju, C.E. Barnes, *J. Chem. Soc. Dalton Trans.*, 24 (1999) 1201.
- [6] S.H. Ha, R.N. Menchavez, Y.M. Koo, *Korean J. Chem. Eng.*, 27 (2010) 1360.

- [7] Cytec product sheet CYPHOS®, <https://www.cytec.com/specialty-chemicals/ionicliquidstable.htm> <Accessed: February 26, 2013>.
- [8] M.G. Freire, P.J. Carvalho, R.L. Gardas, L.M.N.B.F. Santos, I.M. Marrucho, J.A.P. Coutinho, *J. Chem. Eng. Data*, 53 (2008) 2378.
- [9] J.C. Wren, Steady-State Radiolysis: Effects of Dissolved Additives, in: ACS Symposium Series: Nuclear Energy and the Environment, C.M. Wai, B.J. Mincher, Editors, Oxford University Press, Washington, DC (2010), p. 271-295.
- [10] J.C. Wren, J.M. Ball, *Radiat. Phys. Chem.*, 60 (2001) 577.
- [11] P.A. Yakabuskie, J.M. Joseph, P. Keech, G.A. Botton, D. Guzonas, J.C. Wren, *Phys. Chem. Chem. Phys.*, 13 (2011) 7167.
- [12] P.A. Yakabuskie, J.M. Joseph, J.C. Wren, *Radiat. Phys. Chem.*, 79 (2010) 777.
- [13] J.M. Joseph, B.S. Choi, P. Yakabuskie, J.C. Wren, *Radiat. Phys. Chem.*, 77 (2008) 1009.
- [14] J.W.T. Spinks, R.J. Woods, *An Introduction to Radiation Chemistry*, Wiley, New York (1990).
- [15] Farhataziz, M.A.J. Rodgers, *Radiation Chemistry: Principles and Applications*, VHC Publishers, New York (1987).
- [16] A.O. Allen, *The Radiation Chemistry of Water and Aqueous Solutions*, Van Nostrand, New York (1961).
- [17] T. Singh, A. Kumar, *J. Phys. Chem. B*, 112 (2008) 12968.
- [18] J.F. Wishart, P. Neta, *J. Phys. Chem. B*, 107 (2003) 7261.
- [19] S.E. Howett, J.M. Joseph, J.J. Noel, J.C. Wren, *J. Colloid Interface Sci.*, 361 (2011) 338.
- [20] S.E. Howett, Investigating the Effects of Radiation on Phosphonium-Based Ionic Liquids, Ph.D. Thesis, Department of Chemistry, University of Western Ontario, London, Ontario (2013).
- [21] J.C.F. Diogo, F.J.P. Caetano, J.M.N.A. Fareleira, W.A. Wakeham, C.A.M. Afonso, C.S. Marques, *J. Chem. Eng. Data*, 57 (2012) 1015.
- [22] D.R. MacFarlane, S.A. Forsyth, J. Golding, G.B. Deacon, *Green Chem.*, 4 (2002) 444.
- [23] A.A. Zavitsas, D.W. Rogers, N. Matsunaga, *J. Org. Chem.*, 75 (2010) 5697.
- [24] D.C. Nonhebel, J.C. Walton, *Free-radical Chemistry; Structure and Mechanism*, Syndics of the Cambridge University Press, London, UK (1974).
- [25] J. Clayden, N. Greeves, S. Warren, P. Wothers, *Organic Chemistry*, Oxford University Press, New York, (2001).
- [26] H.S. Myers, *Ind. Eng. Chem.*, 47 (1955) 1659.
- [27] A.A. Zavitsas, *J. Org. Chem.*, 73 (2008) 9022.
- [28] G. Le Rouzo, C. Lamouroux, V. Dauvois, A. Dannoux, S. Legand, D. Durand, P. Moisy, G. Moutiers, *Dalton Trans.*, 31 (2009) 6175.
- [29] R.P. Morco, A.Y. Musa, J.C. Wren, *Solid State Ionics*, 258 (2014) 74.
- [30] G.E. Walrafen, L.A. Blatz, *J. Chem. Phys.*, 59 (1973) 2646.
- [31] D.M. Carey, G.M. Korenowski, *J. Chem. Phys.*, 108 (1998) 2669.
- [32] P.C. Trulove, R.A. Mantz, *Electrochemical Properties of Ionic Liquids*, in: *Ionic Liquids in Synthesis*, P. Wasserscheid, T. Welton, Editors, Wiley-VCH Verlag, Weinheim, Germany (2008).

- [33] R.L. Perry, K.M. Jones, W.D. Scott, Q. Liao, C.L. Hussey, *J. Chem. Eng. Data*, 40 (1995) 615.
- [34] Q. Liao, C.L. Hussey, *J. Chem. Eng. Data*, 41 (1996) 1126.
- [35] D. Allen, G. Baston, A.E. Bradley, T. Gorman, A. Haile, I. Hamblett, J.E. Hatter, M.J.F. Healey, B. Hodgson, R. Lewin, K.V. Lovell, B. Newton, W.R. Pitner, D.W. Rooney, D. Sanders, K.R. Seddon, H.E. Sims, R.C. Thied, *Green Chem.*, 4 (2002) 152.
- [36] L. Berthon, S.I. Nikitenko, I. Bisel, C. Berthon, M. Faucon, B. Saucerotte, N. Zorz, P. Moisy, *Dalton Trans.*, 21 (2006) 2526.
- [37] M.Y. Qi, G.Z. Wu, Q.M. Li, Y.S. Luo, *Radiat. Phys. Chem.*, 77 (2008) 877.
- [38] N.J. Bridges, A.E. Visser, M.J. Williamson, J.I. Mickalonis, T.M. Adams, *Radiochim. Acta*, 98 (2010) 243.
- [39] C. Jagadeeswara Rao, K.A. Venkatesan, B.V.R. Tata, K. Nagarajan, T.G. Srinivasan, P.R. Vasudeva Rao, *Radiat. Phys. Chem.*, 80 (2011) 643.
- [40] M.Y. Qi, G.Z. Wu, S.M. Chen, Y.D. Liu, *Radiat. Res.*, 167 (2007) 508.
- [41] B. Valeur, M.N. Berberan-Santos, *Molecular Fluorescence: Principles and Applications*, Wiley-VCH Verlag, Weinheim, Germany (2012).
- [42] J.B. Coon, R.E. DeWames, C.M. Loyd, *J. Mol. Spectrosc.*, 8 (1962) 285.
- [43] C.J. Delbecq, P. Pringsheim, P. Yuster, *J. Chem. Phys.*, 19 (1951) 574.
- [44] N.J. Kreidl, J.R. Hensler, *J. Am. Ceram. Soc.*, 38 (1955) 423.
- [45] F. Wishart James, A. Shkrob Ilya, *Ionic Liquids: From Knowledge to Application*, American Chemical Society, (2009) 119.
- [46] G.V. Buxton, C.L. Greenstock, W.P. Helman, A.B. Ross, *J. Phys. Chem. Ref. Data*, 17 (1988) 513.
- [47] J.F. Wishart, *Radiation Chemistry of Ionic Liquids: Reactivity of Primary Species*, in: *Ionic Liquids as Green Solvents: Progress and Prospects*, R.D. Rogers, K.R. Seddon, Editors, ACS, Washington, DC (2003).

Chapter 6

Corrosion Behaviour of Carbon Steel in [P₁₄₆₆₆][Br]: The Effects of γ -Radiation and Cover Gas

6.1 INTRODUCTION

In Chapter 5, we investigated the effect of γ -radiation on the chemical stabilities and the ion transport properties of phosphonium-based ionic liquids. That work found that phosphonium-based ILs are generally chemically stable under γ -irradiation and this makes them ideal candidates for use in nuclear fuel processing and waste reduction. For such applications, the compatibility of the ILs with the processing system materials under γ -irradiation must also be established.

The most serious form of degradation of a metal alloy in an electrolyte medium is corrosion. Electrochemical corrosion of metal alloys involves metal oxidation coupled, typically, with the reduction of solution species at the metal/solution interface (or if an oxide film is present, the metal/oxide and oxide/solution interfaces). In order for the reaction to occur the interfacial redox reaction must be followed by charge transport between the metal, oxide film, if present, and liquid phases. Thus, radiation-induced changes in the transport properties as well as the production or removal of redox active species in solution can have a significant effect on corrosion.

Electrochemical corrosion has been studied most extensively in aqueous environments; some more recent studies on aqueous corrosion of carbon steel can be

found in references [1-8]. Electrochemical corrosion studies in non-aqueous electrolytes are very rare, mainly due to a lack of important non-aqueous electrolytes (other than alcohol/water mixtures), and are mostly limited to work with molten salts at high temperatures [9-12]. However, the recent development of room temperature ILs with wide electrochemical windows has provided a category of non-aqueous electrolytes that can be used for electrochemical processes at low temperatures. Studies on electrochemical processes in IL electrolytes are still in an infant stage and are furthermore limited to systems with inert surfaces. Studies on electrochemical corrosion of materials in contact with ILs are very rare. To date, only studies on carbon steel corrosion in imidazolium cation-based ILs have been reported [13, 14]. In one of these studies Uerdingen et al. studied the effect of water dissolved in the ILs on corrosion and found that carbon steel may undergo severe corrosion in water-diluted IL media, with the severity of the corrosion depending on the IL composition [13]. We are not aware of any study on the effect of γ -radiation on corrosion of metal alloys in IL solutions.

Ionic liquids are generally redox inactive but their solvation of redox active species such as H_2O and O_2 , and corrosion products such as metal ions and hydrogen, vary considerably [15-18]. Some of the radiolytic decomposition products from certain ILs can be highly redox active. As well the organic radicals produced from the decomposition of the organic chains in the IL molecules can react very effectively with O_2 . Thus, although the net yields from radiolytic decomposition of ILs are relative small, the species that are formed can influence redox chemistry. In addition, our earlier work has shown that the radiolytic production of small organic molecules can affect the molecular configuration within an IL and can lead to the formation of micelles and/or

strengthening of the Coulombic attraction of ion-pairs within the IL [19, 20]. These changes can have a significant effect on the mass and charge transport properties of the ILs and this can affect the mobility of ions and other species involved in corrosion.

We have investigated the corrosion of carbon steel (CS) in the phosphonium IL [P₁₄₆₆₆] [Br] in the presence and absence of γ -radiation. The changes in the surfaces of the carbon steel coupons corroded in the IL solutions exposed to different cover gases (air and argon) were examined. In addition to the surface analyses, the amount of dissolved iron in the ionic liquid phase was analyzed using inductively coupled plasma-mass spectrometry (ICP-MS).

6.2 EXPERIMENTAL

Details on the test preparation and experimental procedures can be found in Chapter 3. Details on the surface analysis procedures are given in the following sections.

6.2.1 X-ray Photoelectron Spectroscopy

The XPS analyses were carried out on a Kratos Axis Ultra spectrometer using a monochromatic Al K(alpha) source (15mA, 14kV). XPS can detect all elements except hydrogen and helium, probe the surface of a sample to a depth of 5-7 nanometres, and has a detection limit ranging from 0.1 to 0.5 atomic percent depending on the element. The instrument work function was calibrated to give a binding energy (BE) of 83.96 eV for the Au 4f_{7/2} line for metallic gold and the spectrometer dispersion was adjusted to give a BE of 932.62 eV for the Cu 2p_{3/2} line of metallic copper. The Kratos charge neutralizer system was used on all specimens. Survey scan and high resolution analyses were

carried out with an analysis area of 300 x 700 microns and a pass energy of 160 eV and 20 eV respectively. Spectra have been charge corrected to the main line of the carbon 1s spectrum (adventitious carbon) set to 284.8 eV. Spectra were analysed using CasaXPS software (version 2.3.14).

6.2.2 Scanning Electron Microscopy/Energy Dispersive X-ray Spectroscopy

Scanning electron micrographs were obtained using an Hitachi S-4500 Field emission scanning electron microscope equipped with a Quartz XOne EDX system at Surface Science Western (SSW) or using the LEO (Zeiss) 1540XB FIB/SEM at the Western Nanofabrication Facility. The images were collected at 1000x to 10000x magnification using an electron beam potential of 10.0 kV or 5.0 kV. Elemental compositions of the surface's features were also characterized by EDX.

6.2.3 Raman Spectroscopy

The chemical composition and phase of an oxide present on a metal surface can be determined using Raman spectroscopy. Raman scattering measurements were performed at SSW using a Renishaw model 2000 Raman Spectrometer (Renishaw PLC., UK), equipped with a MellesGriot 35 mW HeNe laser with excitation wavelength of 633 nm and a focused beam of ~2- μ m diameter. The laser power was reduced to 25% to avoid laser heating effects since small changes in temperature can easily produce minor changes in the frequency and width of Raman lines. The Raman spectrometer was calibrated using a Si crystal standard at room temperature. The laser beam was focused onto the sample mounted on a Leica DMLM microscope with a 50x uncoated objective lens. Each spectrum was acquired for an exposure time of ~30 s over a frequency range

of 120 to 2000 cm^{-1} . Several measurements were conducted at different spots on the coupon surface to ensure consistency in the measured Raman bands.

6.3 RESULTS

6.3.1 The Physical and Chemical Properties of the [P₁₄₆₆₆] [Br] IL

The chemical formula of [P₁₄₆₆₆] [Br] used in this study and its physical and chemical properties are listed in Table 6.1. This IL is highly viscous and not miscible with water, but the solubility of water in this IL is not negligible; it is 7 wt.% or 0.678 in mole fraction. The solubility of O₂ in the IL is not known. Many hydrophobic ILs are known to absorb water from the atmosphere and, in fact, water is frequently one of the most significant impurities in an IL [21]. Since H₂O is an effective oxidant for iron, the water content in the IL electrolyte can affect the corrosion behaviour of carbon steel. An increase in the water content in an IL has also been shown to decrease the viscosity and the electrochemical potential window of the IL [22]. These changes may facilitate the transport of the oxidants H₂O and O₂ as well as metallic ion corrosion products in the IL phase. Listed in the table are the airborne radiolysis products detected in the headspace after irradiation of the IL under Ar-purged conditions in a sealed cell [20].

Table 6.1 The chemical and physical properties ($T = 25\text{ }^{\circ}\text{C}$) of $[\text{P}_{14666}] [\text{Br}]$.

Chemical structure	$\begin{array}{c} (\text{CH}_2)_5\text{CH}_3 \\ \\ \text{H}_3\text{C}(\text{H}_2\text{C})_5-\text{P}^+-\text{(CH}_2\text{)}_{13}\text{CH}_3 \\ \\ (\text{CH}_2)_5\text{CH}_3 \quad \text{Br}^- \end{array}$					
Physical properties	Density (g/mL) [23]	Viscosity (cP) [24]	Conductivity ($\mu\text{S/cm}$)	Miscible with Water [23]	Melting Point ($^{\circ}\text{C}$) [23]	Solubility of H_2O (wt %) [25]
	0.9546	2988	9	No	-61	6.720
Airborne radiolysis products [20]	hexane (C_6H_{14}), hexene (C_6H_{12}), propane (C_3H_8)					

The corrosion of carbon steel in the IL was investigated in the absence and presence of γ -radiation. In both cases the IL electrolyte was exposed to different cover gases: (1) open air (unlimited supply of air), (2) initially aerated headspace in a sealed container (limited supply of air), and (3) an Ar-purged headspace in a sealed container. Hereafter, these cases are referred to simply as open air, sealed air and Ar. To assist in the interpretation of the observed effect of γ -radiation, the corrosion of carbon steel in the absence of γ -radiation was further investigated in the IL diluted with 20 vol.% hexane, hereafter referred to as hexane-IL.

6.3.2 Corrosion Behaviour in the Absence of Radiation

The SEM images and the Raman spectra of the carbon steel surfaces corroded for 96 h in the $[\text{P}_{14666}] [\text{Br}]$ in the absence of γ -radiation are shown in Figure 6.1. The SEM

images show different degrees of oxide formation and growth on the coupon exposed to different cover gases.

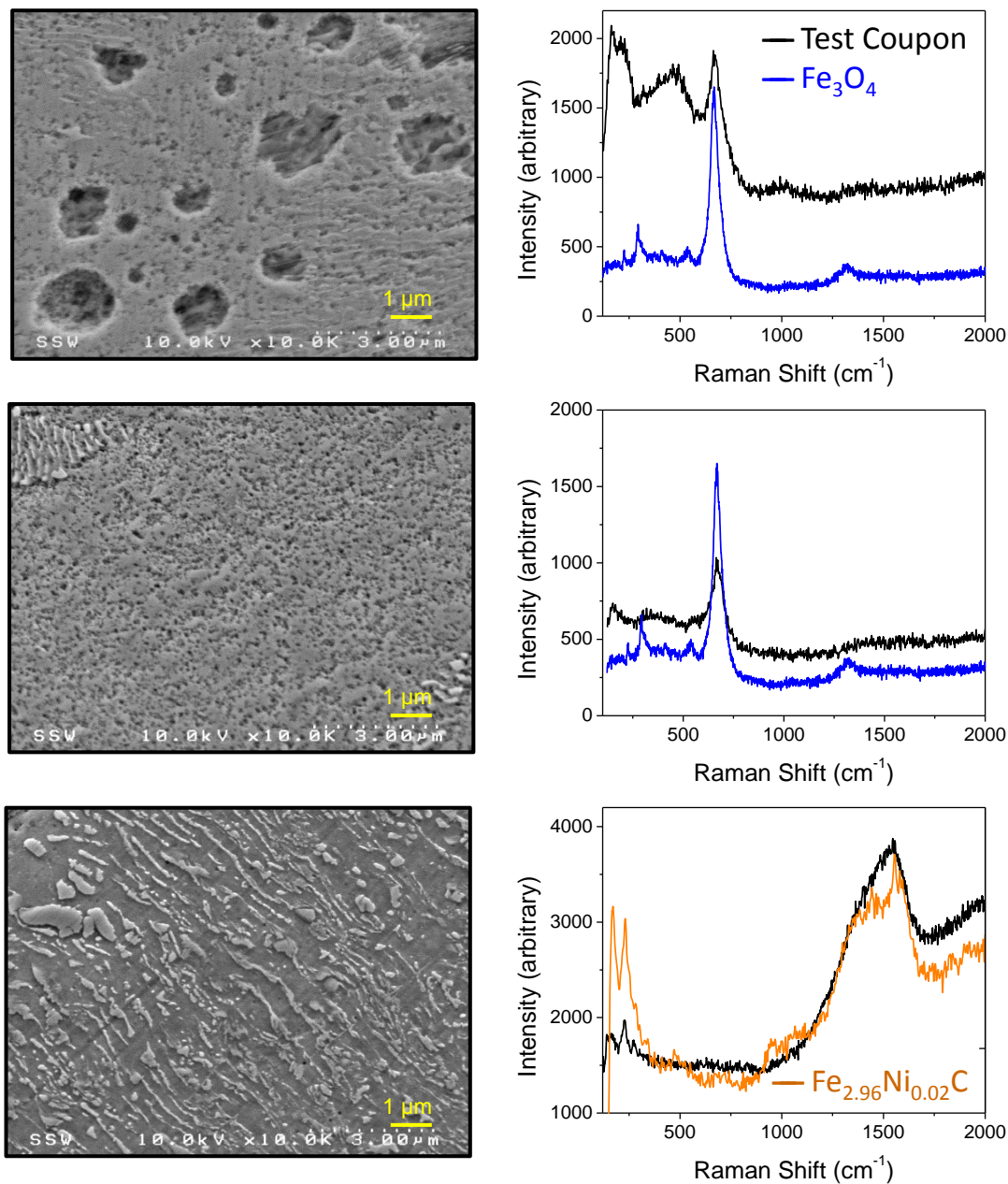


Figure 6.1 SEM images and the Raman spectra versus reference of carbon steel surfaces corroded for 96 h in [P₁₄₆₆₆] [Br] in the absence of γ -radiation, where the IL was exposed to: (top) open air, (middle) sealed air and (bottom) argon.

The carbon steel corroded in the IL exposed to Ar (Figure 6.1-bottom) shows the remnant of the pearlite structure of carbon steel. Pearlite refers to a lamella structure consisting of alternating phases of α -ferrite (a pure Fe phase in a body-centered cubic crystal structure) and cementite (Fe_3C in an orthorhombic crystal structure), and is present in mild steels and cast iron [26-29]. The corresponding Raman spectrum shows no peaks corresponding to iron oxides and is very similar to the reference spectrum taken of a cementite sample containing small amounts of Ni impurity. This result indicates that the corrosion of the carbon steel in this environment is limited to the oxidation of Fe in the α -ferrite phase followed by dissolution of the metal cation (likely Fe^{II}) into the IL solution, leaving the cementite skeletons on the surface. The α -ferrite sites appear to have corroded uniformly and no preferential corrosion along the metal phase boundaries or pitting corrosion were observed.

The SEM image and the corresponding Raman spectrum of the surface of a coupon corroded in the IL exposed to sealed air show the presence of a uniform layer of mostly magnetite (Fe_3O_4) (Figure 6.1-middle). The Raman peak near 660 cm^{-1} is characteristic of magnetite [30]. Magnetite is a mixed $\text{Fe}^{\text{II}}/\text{Fe}^{\text{III}}$ oxide and is less soluble than Fe^{II} species in water [8, 31-37]. The observation that the Fe oxidation leads to the formation of a magnetite layer instead of metal ion dissolution indicates that this oxide is formed faster in the sealed air environment than in the Ar environment and that the magnetite is not as soluble as Fe^{II} species in the IL.

The carbon steel coupon corroded in the IL exposed to open air shows the most extensive corrosion. The SEM images of the coupon show a few micron-sized pits evenly distributed on the surface, in addition to a similar uniform magnetite layer to that

was observed on a coupon corroded in sealed air. The Raman spectrum of this surface also shows an additional broad peak developing in the range of 250 - 600 cm^{-1} . Many Fe^{III} oxides or oxyhydroxides (α - and γ - Fe_2O_3 and α - and γ - FeOOH) have peaks in this wavenumber range as can be seen from the reference spectra of various oxides in Figure 6.2. The XPS analysis of this surface (discussed below) further confirms the presence of Fe^{III} oxides/oxyhydroxides.

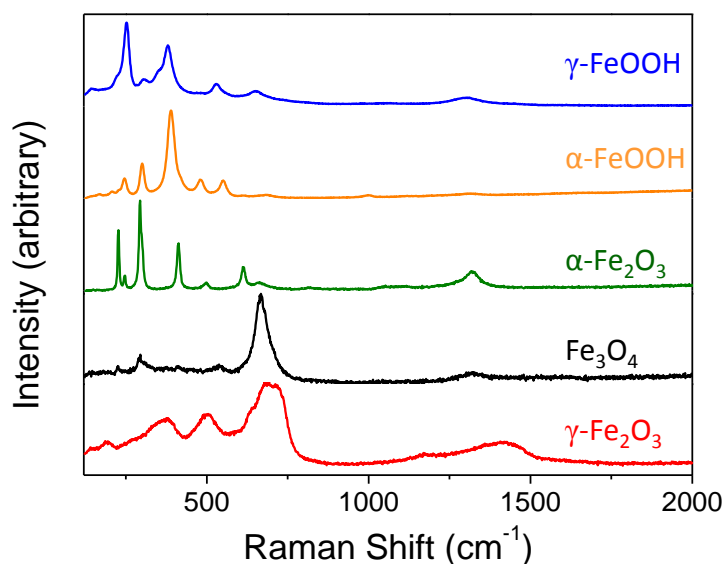


Figure 6.2 Reference Raman spectra of iron oxides and oxyhydroxide minerals.

The surfaces shown in Figure 6.1 were also analyzed by EDX. The EDX elemental analysis results are summarized in Table 6.2. Comparison of the Ar case with the sealed air case shows a smaller O but a larger C fraction for the Ar case, consistent with the SEM image showing the enrichment of cementite on the surface without the formation of an oxide layer. Both O and C fractions are significantly larger on the

coupon corroded in the IL exposed to open air compared to the other cases. The EDX analysis of the open air case also shows the presence of P and Br, albeit at small fractions, indicating the presence of IL residue, particularly in the pits. The XPS analysis of this surface also indicates that the C on the surface is mostly aliphatic carbon and not bound to OH or O, (see below). The high O/Fe ratio suggests that oxide formation is the most extensive with the IL exposed to open air.

Table 6.2 EDX elemental analysis results (in atomic %) of the surfaces of the carbon steel coupons corroded in [P₁₄₆₆₆] [Br] exposed to different cover gases.

Element	Open Air	Sealed Air	Argon
C	30.23	9.37	13.12
O	14.06	1.62	1.42
Si	1.43	0.62	0.58
P	0.80	-	-
Mn	-	1.45	1.52
Fe	52.69	86.93	83.36
Br	0.78	-	-

The XPS obtained for the coupon corroded in the IL exposed to open air are shown in Figure 6.3. The survey XPS taken in the binding energy range of 0 to 1100 eV shows C and P, in addition to O and Fe, peaks with atomic percentages of 46%, 2%, 40% and 11%, respectively. The deconvolution of the high resolution XPS of the C 1s band at binding energy 285 eV shows that aliphatic carbon contributes 77% to the C 1s band. However, the high resolution XPS of the O 1s band shows the presence of a very small organic O percentage. These results suggest that an adsorbed IL layer is present on the surface but the IL molecules have not been directly involved in the metal oxidation.

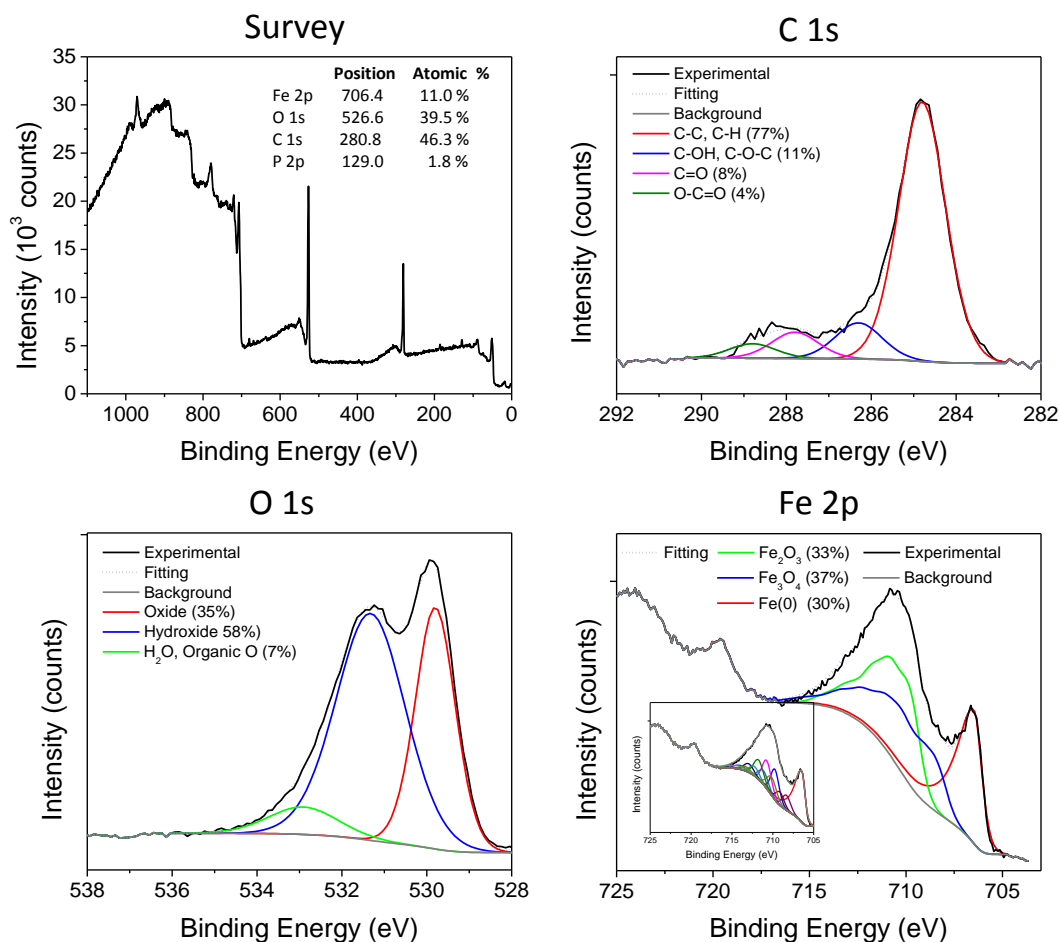


Figure 6.3 XPS spectra taken from a carbon steel surface corroded for 96 h in [P₁₄₆₆₆] [Br] exposed to open air in the absence of γ -irradiation. The survey spectrum in the binding energy of 0 to 1100 eV and the high resolution spectra of the C 1s, O 1s, and Fe 2p bands are shown. The inset in the Fe 2p spectrum shows the deconvoluted Fe_xO_y components, each consisting of multiple peaks.

The high resolution spectra of the O 1s and Fe 2p bands were further analyzed for iron oxide speciation. For this analysis, the Fe 2p spectrum was deconvoluted using the reference spectra taken from pure phase iron and iron oxides as described in references [15-17, 38-40]. Each oxide shows multiple peaks (Figure 6.3 inset). Consistent with the

Raman analysis, the XPS analysis shows the presence of Fe_3O_4 and also Fe^{III} oxides; the atomic percentages of metallic Fe, Fe_3O_4 and Fe_2O_3 are 30, 37 and 33%, respectively.

The presence of Fe^0 in the XPS Fe 2p band suggests that the oxide layer is thin (the XPS analysis depth is estimated to be ~9 nm) or porous.

Cross-section analysis by FIB and SEM of the coupon corroded in the IL exposed to open air shows a grainy oxide layer with a depth ranging from 90 – 150 nm, Figure 6.4. The layered pearlite structure in the carbon steel phase can be clearly seen in the cross section image and the grainy oxides are formed on the surfaces of the cementite as well as α -ferrite rich phases. The image further suggests that small pits may have been initiated from cracks developed along the oxide grain boundaries (rather than the metal phase boundaries), which then separate the grains from the bulk metal and/or metal oxide phase.

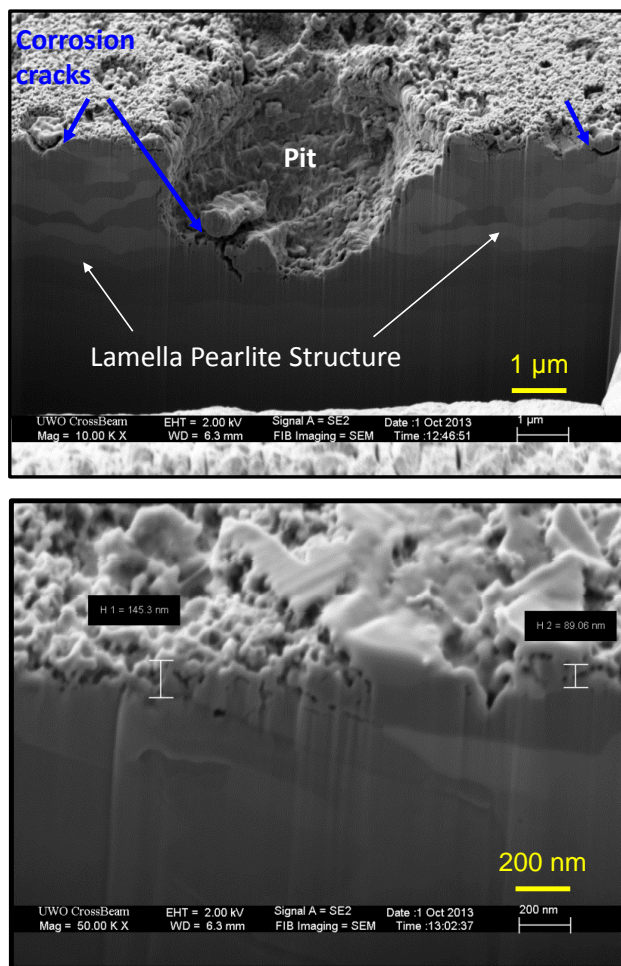


Figure 6.4 The SEM images with different magnifications of the cross section of the carbon steel coupons corroded for 96 h in [P₁₄₆₆₆] [Br] exposed to open air in the absence of γ -irradiation.

In addition to coupon surface analyses, the IL solutions were analyzed for dissolved iron contents using ICP-MS, Table 6.3. In the absence of radiation, the metal dissolution was more extensive in the IL exposed to Ar than in the IL exposed to open air. The results are consistent with the above claim that the oxidation of Fe in the Ar environment is slow and limited to the formation of more soluble Fe^{II} species from the α -ferrite sites. Consequently, the carbon steel corrosion in this environment leads mainly to

iron dissolution and very little oxide film formation. On the other hand, the oxidation of Fe in the open air environment is very fast and leads to the formation of less soluble Fe^{II}/Fe^{III} (magnetite) and Fe^{III} oxides. Due to the more oxidizing IL environment with open air, the oxidation occurs on both α -ferrite and cementite sites as seen in Figure 6.4. The table also presents the results obtained from the radiation tests. These results are discussed in Section 6.3.3.

Table 6.3 Dissolved iron concentration in [P₁₄₆₆₆] [Br] after 96 h corrosion of carbon steel exposed to different cover gases in the absence and presence of γ -irradiation.

Cover Gas	mg/L	
	No Rad	Rad
Open air	10.6	5.8
Argon	21.2	5.5

6.3.3 Corrosion Behaviour in the Presence of γ -Radiation

All of the CS coupons corroded in [P₁₄₆₆₆] [Br] under γ -irradiation show smooth surfaces, irrespective of the cover gas environment (Figure 6.5). Due to the smoothness and reflectivity of the surfaces, the Raman scattering intensities from these surfaces were very weak and the Raman spectra did not reveal much. The irradiated coupons have the same reflectance Raman spectra as a freshly polished CS surface. Nevertheless, the polish lines on the surfaces corroded in the IL exposed to open air and sealed air appear

to be more blurred than those on a surface corroded in Ar, suggesting these surfaces are covered by a uniform oxide layer.

The cross section image of a coupon corroded in the IL exposed to Ar (Figure 6.6) shows the presence of a thin, compact inner oxide layer, ~ 25 nm in depth, and an outer layer with a needle-like structure. The XPS analysis of this surface (see further below) shows the presence of Fe^{II}/Fe^{III} oxide (Fe₃O₄) and Fe^{III} oxides/hydroxides. Thus, we attribute the inner layer to magnetite and the outer layer to Fe^{III} oxides/hydroxides. A smooth, uniform layer of magnetite has been also observed on carbon steel surfaces corroded in high pH water where the solubilities of Fe^{II} and Fe^{III} species are low [37].

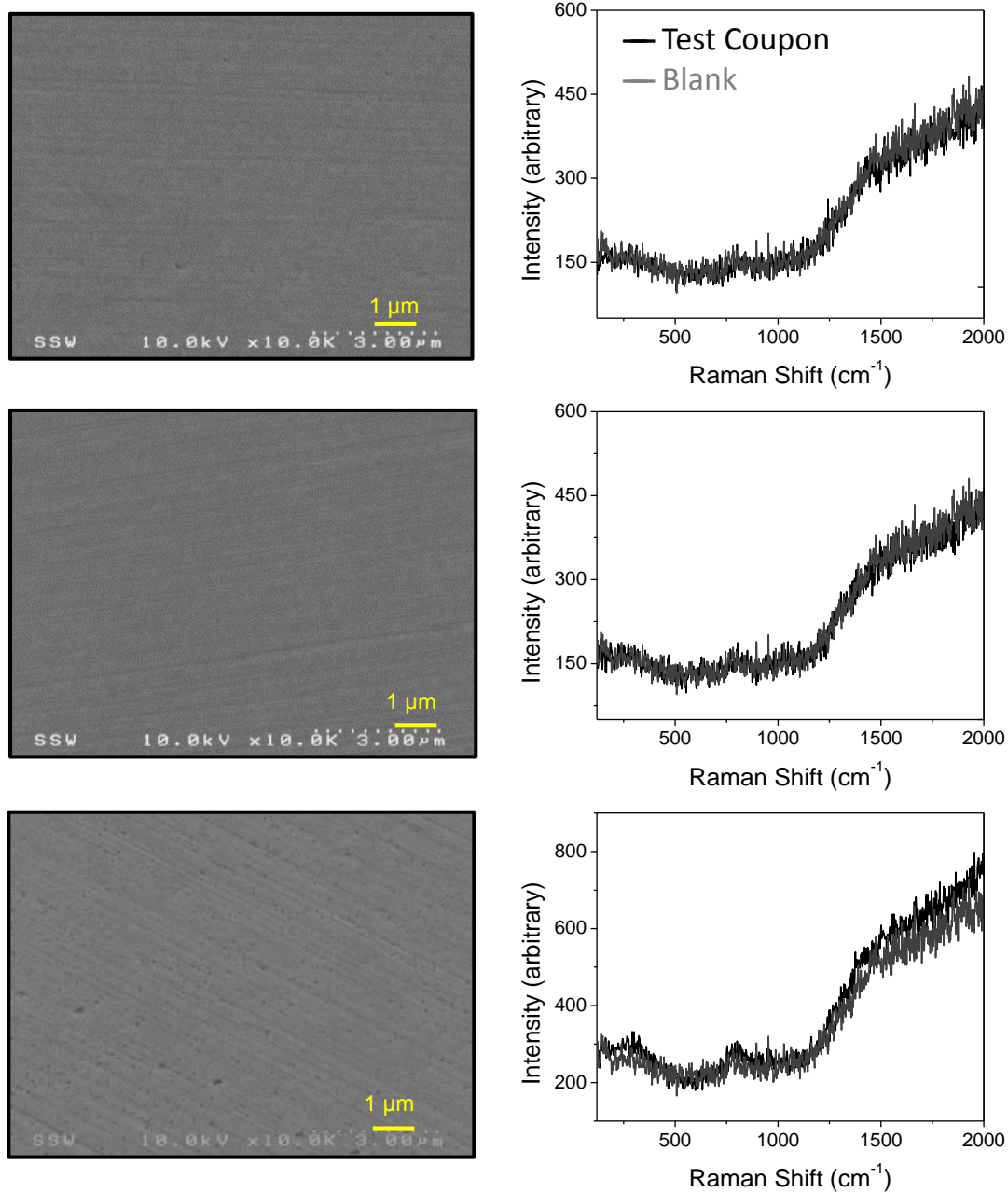


Figure 6.5 SEM images and Raman spectra versus reference of the carbon steel coupon surfaces corroded for 96 h in [P₁₄₆₆₆] [Br] under γ -irradiation where the IL was exposed to: (top) open air, (middle) sealed air and (bottom) argon.

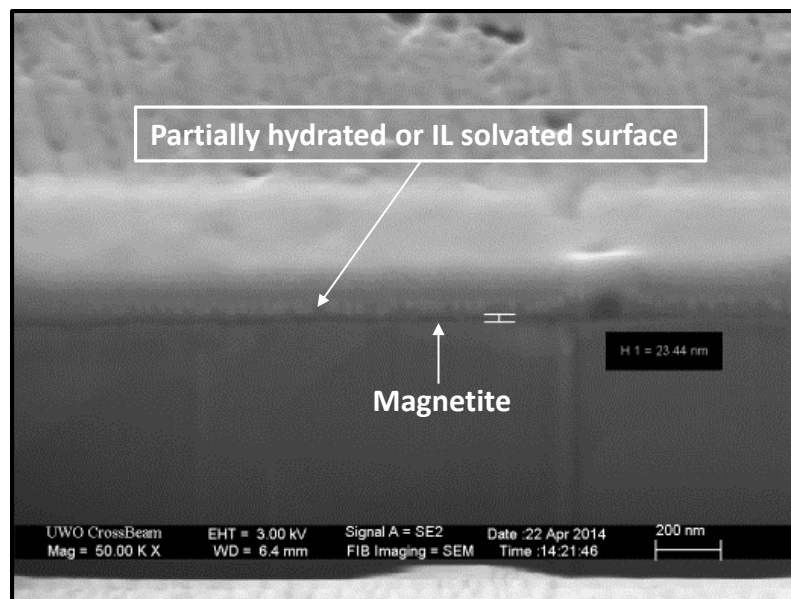


Figure 6.6 Cross-sectional SEM image of a carbon steel surface corroded for 96 h in [P₁₄₆₆₆] [Br] in argon under γ -irradiation.

The coupons corroded in the IL exposed to Ar and open air under γ -irradiation were further analyzed by XPS, Figures 6.7 and 6.8, respectively. On both surfaces the survey spectra show large atomic percentages of C at 51% and 46%, respectively. As observed for the un-irradiated coupon (Figure 6.3), the high resolution C 1s spectrum suggests that the carbon on the surface is mostly aliphatic carbon, contributing 78% and 76% of the C 1s band for the Ar and open air cases. On these surfaces the survey spectra also show the presence of P and N, where the source of P is the IL and the source of N is likely humid air radiolysis [41]. These results suggest that an adsorbed IL layer is present also on the surface but the IL molecules have not been directly involved in the metal oxidation.

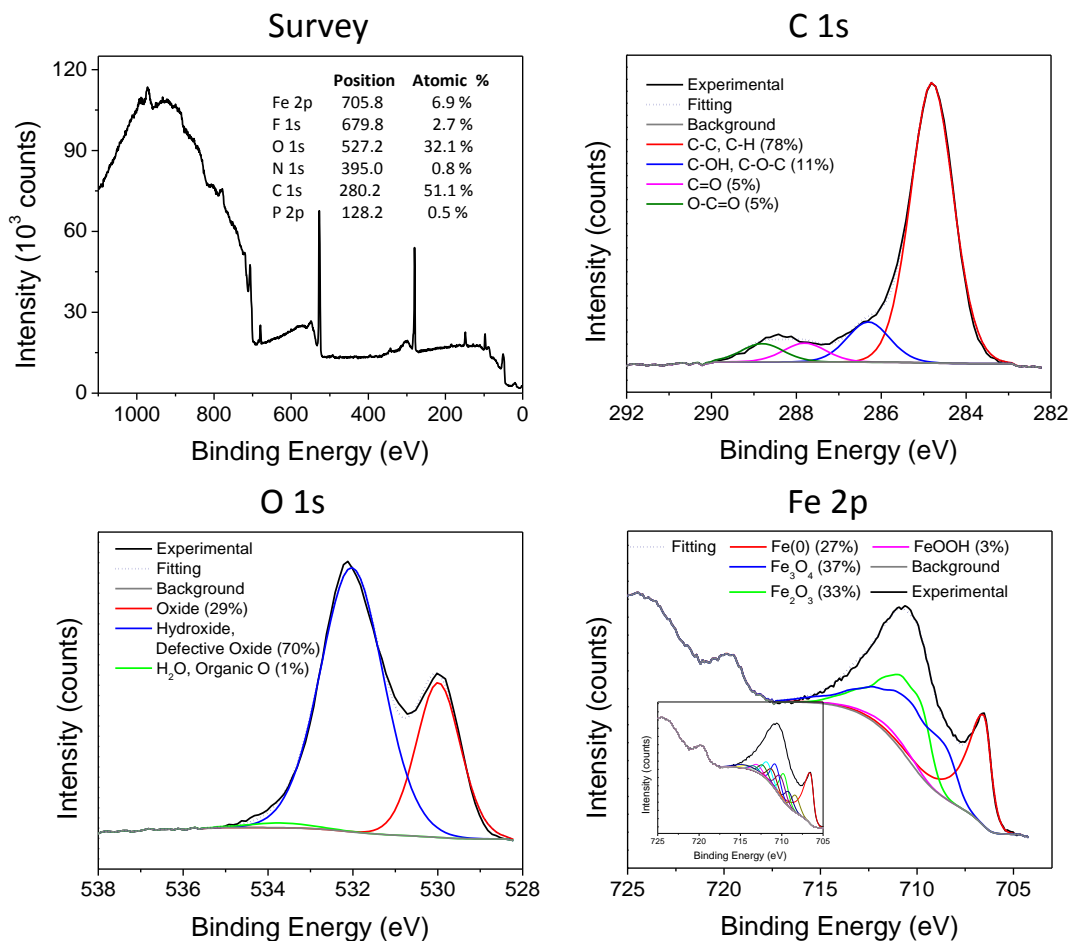


Figure 6.7 XPS spectra taken from a carbon steel surface corroded for 96 h in [P₁₄₆₆₆] [Br] exposed to Ar under γ -irradiation. The survey spectrum in the binding energy of 0 to 1100 eV and the high resolution spectra of the C 1s, O 1s, and Fe 2p bands are shown. The inset in the Fe 2p spectrum shows the deconvoluted Fe_xO_y components, each consisting of multiple peaks.

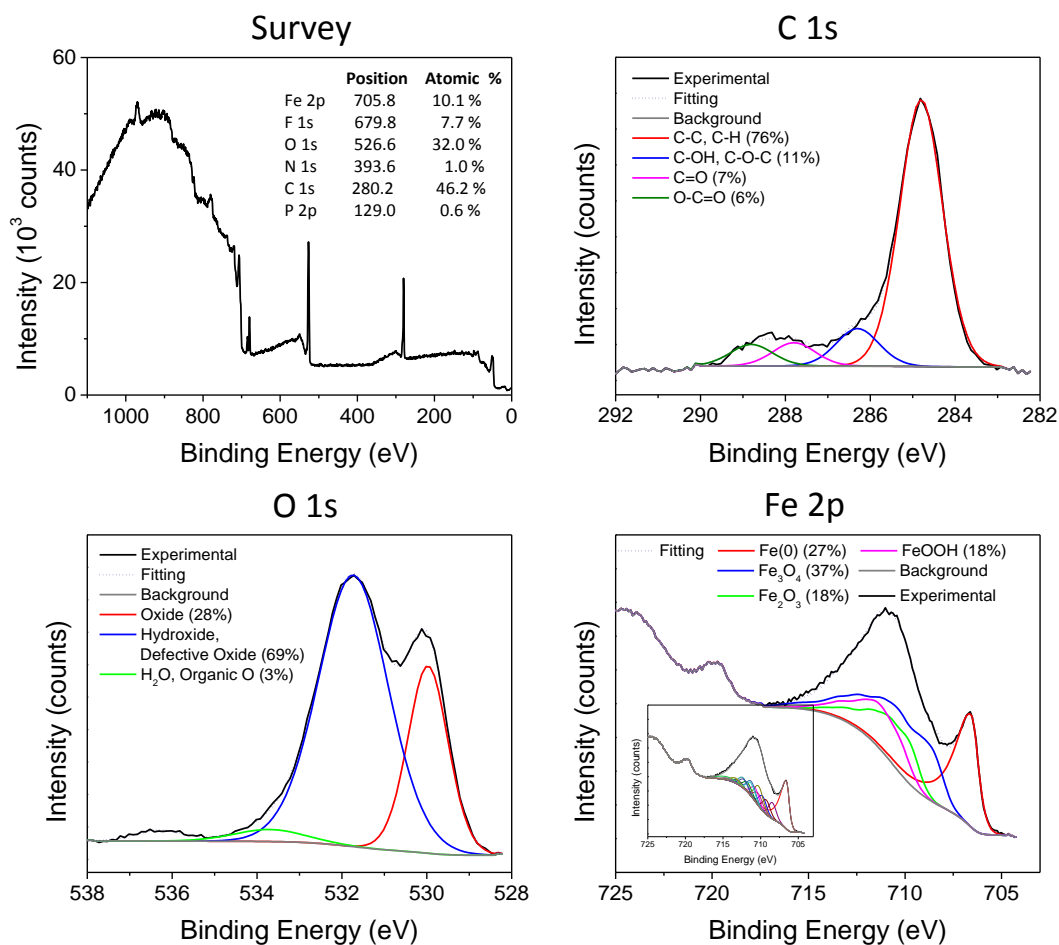


Figure 6.8 XPS spectra taken from a carbon steel surface corroded for 96 h in [P₁₄₆₆₆] [Br] exposed to open air under γ -irradiation. The survey spectrum in the binding energy of 0 to 1100 eV and the high resolution spectra of the C 1s, O 1s, and Fe 2p bands are shown. The inset in the Fe 2p spectrum shows the deconvoluted Fe_xO_y components, each consisting of multiple peaks.

The iron oxide speciation determined from the Fe 2p and the O 1s band analyses are summarized in Table 6.4. Comparison of the results for irradiated coupons in the Ar versus the open air environment shows that (1) the ratios of the Fe oxide to the metallic Fe fraction in the Fe 2p band are similar, and (2) the fractions of Fe₃O₄ (magnetite) in the

Fe oxide component are also similar, but (3) the FeOOH fraction in the Fe^{III} oxide component is higher for the open air environment than for the Ar environment.

Table 6.4 XPS analysis results of Fe speciation (in atomic %) in the surface layer of the carbon steel coupons corroded in [P₁₄₆₆₆] [Br] exposed to different cover gases in the absence and the presence of γ -irradiation.

	Fe ⁰	Fe ₃ O ₄	Fe ₂ O ₃	FeOOH
Un-irradiated in open air	30	37	33	Not observed
Irradiated in Ar	27	37	33	3
Irradiated in open air	27	37	18	18

The dissolved iron contents in the IL solutions exposed to Ar and open air are given in Table 6.3. The results show that metal dissolution is significantly less during corrosion in the presence of γ -radiation than in the absence of radiation. Furthermore, in the absence of radiation the dissolved iron concentration depends strongly on the cover gas environment, whereas in the presence of radiation it is nearly independent of cover gas type. These results are consistent with the surface analysis results that show negligible dependence on cover gas in the presence of radiation.

This apparent independence of the corrosion behaviour on the nature of the cover gas may be attributed to the reactions of radiolytically-formed organic radicals with O₂. Our work in Chapter 5 showed that radiolytic decomposition of phosphonium-based ILs yields small organic molecules. Irradiation of the IL cation induces P – C and C – C

bond dissociation forming organic radicals which then either abstract or donate an H• atom to form stable hydrocarbons [20]. Oxygen is known to be an effective scavenger of organic radicals; organic radicals react readily with O₂ to form alcohols and aldehydes [42-44]. Such reactions will deplete any O₂ dissolved in the IL. If the scavenging is sufficiently fast, the concentration of O₂ in the IL will stay low and the concentration of O₂ in the headspace will not have much influence on corrosion.

Nevertheless, the degree of surface oxidation occurring during 96 h corrosion in the presence of radiation, as observed by XPS, is very similar to the amount of corrosion seen for the open air case in the absence of radiation. That is, the fractions of Fe₃O₄ and Fe^{III} species (Fe₂O₃ + FeOOH) in the XPS Fe 2p bands, are nearly the same (Table 6.4). This suggests that the IL electrolyte environment under γ -irradiation becomes as oxidizing as the IL exposed to open air in the absence of radiation. The ratio of FeOOH to Fe₂O₃ increases in the order: un-irradiated in open air < irradiated in Ar < irradiated in open air. This result can arise if the oxidizing species present in the IL under γ -irradiation is not dissolved O₂ but rather some other radiolytically-formed oxidant.

Daub et al. have found that the aqueous corrosion of carbon steel under γ -irradiation can be simulated by addition of H₂O₂ to the water [1], as H₂O₂ is the corrosion rate controlling water radiolysis product [45, 46]. We speculate that the formation of H₂O₂ or organic super-oxides via radiolytic decomposition of dissolved impurity water in the IL may be also responsible for the radiation-induced corrosion behaviour observed in this study. Hydrogen peroxide is a stronger oxidant than O₂ and, more importantly, is kinetically more effective. Due to the stronger and faster oxidation by H₂O₂, and the low iron solubility in the IL phase, the oxidation of Fe on the cementite sites may become as

rapid as that on the α -ferrite sites, producing a smooth featureless oxide layer. It has been also observed that corrosion of carbon steel in aerated aqueous solutions produces grainy oxides on the surface, whereas corrosion in deaerated aqueous solutions at high temperatures and high pHs, where the rate of oxide formation is high while the iron solubilities are low, produces a smooth amorphous Fe_3O_4 layer [1, 47, 48]. In the presence of γ -radiation a smooth amorphous Fe_3O_4 layer is formed even at low temperatures [1, 47, 48]. A reduction in the dissolved O_2 concentration and the production of a stronger oxidant such as H_2O_2 under irradiation is thus expected to produce a smooth uniform oxide layer during corrosion in the IL with low iron solubility.

6.3.4 Corrosion Behaviour in $[\text{P}_{14666}] [\text{Br}]$ Diluted with 20 % Hexane

Since hexane was detected in the headspace as a radiolytic decomposition product of the IL [19, 20], we have investigated the effect of added hexane in the IL on the carbon steel corrosion. The addition of an organic solvent to an IL can decrease its viscosity, and thereby increase the rates of interfacial transfer of key redox species (O_2 and H_2O) from the gas phase to the IL phase and accelerate the diffusion of dissolved species in the IL [49]. SEM images and Raman spectra of carbon steel surfaces corroded for 96 h in hexane-IL exposed to different cover gases are compared in Figure 6.9.

The coupons corroded in the hexane-IL show similar corrosion levels to coupons corroded in pure $[\text{P}_{14666}] [\text{Br}]$, but, for a given cover gas, the corrosion damage is more pronounced in the hexane-IL mixture than in the pure IL. The coupon corroded in hexane-IL exposed to open air shows a higher density of micron-sized pits uniformly distributed over the surface, compared to a coupon corroded in the pure IL (compare

Figure 6.9 and Figure 6.1). The Raman spectra also show the same magnetite peak near 660 cm^{-1} and broad peaks in the $250 - 600\text{ cm}^{-1}$ range. Likewise, a coupon corroded in hexane-IL and sealed air has the similar surface morphology and Raman spectrum as a coupon corroded in the pure IL exposed to sealed air; there is a uniform layer of mostly grainy magnetite. However, the coupon corroded in the hexane-IL has a few pits already developing on the surface.

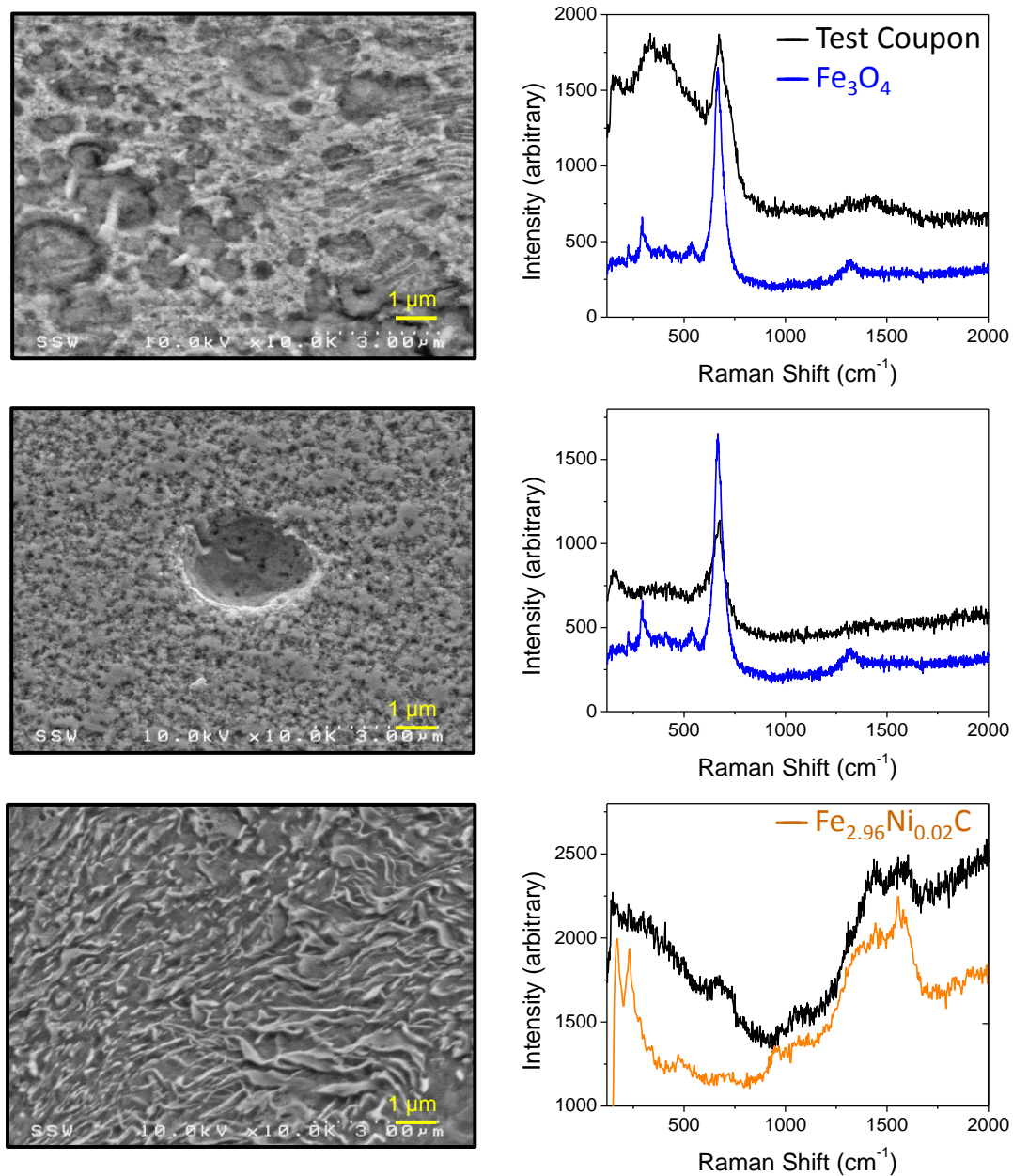


Figure 6.9 SEM images and the Raman spectra versus reference of carbon steel surfaces corroded for 96 h in 20% hexane in $[P_{14666}] [Br]$ solutions, where the IL was exposed to: (top) open air, (middle) sealed air and (bottom) argon.

The coupon corroded in hexane-IL exposed to Ar also shows the pearlite structure but with sharper cementite structures than those observed on a coupon corroded in the

pure IL. The Raman spectrum in this case has peaks corresponding mostly to cementite, but the Raman intensities of the peak near 660 cm^{-1} and the broad band over $250 - 600\text{ cm}^{-1}$ are much higher than those in the coupon Raman spectrum for the pure IL case (Figure 6.1-bottom), indicating the presence of magnetite and Fe^{III} oxides on the surface. The presence of these oxides can be also seen in the SEM image of the same surface, with different areas showing α -ferrite (spot 1) and the cementite (spot 2) phases (Figure 6.10-top). The corresponding EDX analysis of these two spots shows a larger fraction of C on the cementite phase compared to that on the α -ferrite phase. These results are consistent with the claim that the α -ferrite sites are oxidized faster than the cementite sites. The oxide formed on the α -ferrite rich phase shows the same morphology as was observed on a coupon corroded in the sealed air environment but with smaller grains. The cross-section image of the surface (Figure 6.10-bottom) also shows the cementite structure that is left behind after the oxidation and dissolution of the Fe^{II} from the α -ferrite phase. This structure appears to be covered by a thin oxide layer.

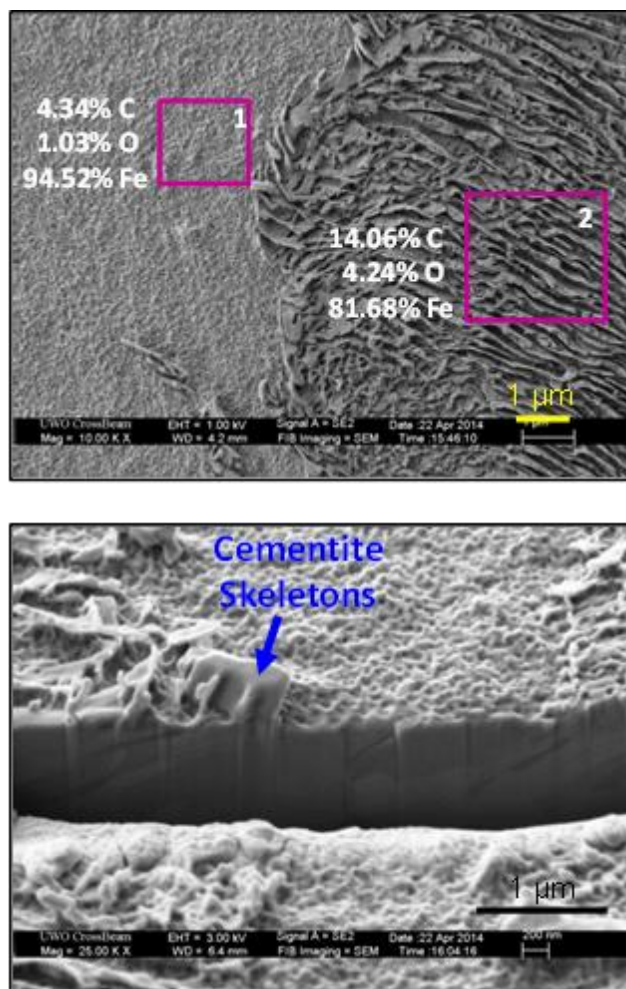


Figure 6.10 SEM image with the elemental distribution of a (top) carbon steel coupon surface corroded for 96 h contact in a 20% hexane in [P₁₄₆₆₆] [Br] solution in argon. Also shown in (bottom) is the cross-sectional image of the coupon surface.

The EDX analyses of the surfaces of the coupons corroded in the hexane-IL exposed to the three different cover gases are listed in Table 6.5. The O/Fe ratios determined by EDX are consistent with the above discussion regarding the corrosion behaviour and show progressively thicker oxide formation in the order: Ar < sealed air < open air.

Table 6.5 EDX elemental analysis (in atomic %) of the surfaces of carbon steel coupons corroded in 20% hexane in [P₁₄₆₆₆] [Br] solutions exposed to different cover gases.

Element	Open Air	Sealed Air	Argon
C	22.54	12.42	9.58
O	12.72	4.16	2.09
Si	0.38	0.45	0.63
P	0.61	0.33	-
Mn	-	1.32	1.71
Fe	63.08	81.18	85.99
Br	0.67	0.15	-

The results show that carbon steel corrodes in a hexane-IL mixture at a faster rate than in pure IL. This is consistent with acceleration of corrosion rates caused by increased diffusion rates of the oxidants O₂ and H₂O in the mixture solution compared to the rates in pure IL.

6.4 PROPOSED CORROSION MECHANISM

The observed carbon steel corrosion in [P₁₄₆₆₆] [Br] under different redox conditions has elements that are similar to carbon steel corrosion in aqueous solutions. Thus, we propose a mechanism for carbon steel corrosion in the IL that is based on our understanding of aqueous corrosion. Corrosion of a metal in an electrolyte medium involves surface redox reactions and interfacial transfer and bulk-phase transport of the reactants and products. The key reactions and transport processes involved in electrochemical corrosion are summarized in Table 6.6, and also schematically shown in

Figure 6.11 [50]. The surface redox reaction consists of the oxidation of Fe (reaction 1a) coupled with the reduction of a species dissolved in the electrolyte (reaction 1b). The carbon steel surface may be covered by an oxide film, which can be initially present from air-oxidation or formed as corrosion progresses. In the presence of a solid oxide film, the metal oxidation occurs at the metal/film interface while the reduction of solution species occurs at the film/solution interface. To complete the corrosion reaction, a net flux of metal cations must occur from the metal and, if present through a solid oxide film, to the solution phase (or the net transport of electrons and anions in the opposite direction). (Note that the net flux of ions from one phase to another does not necessarily mean the physical movement of the massive species through the solid oxide lattice, see further discussion below.) The metal cation can either combine with the oxygen anion to form an oxide or dissolve into the solution phase.

Depending on the redox condition in the electrolyte, the oxidation of Fe can progress from the formation of Fe^{II} species to the formation of oxides of metals with higher oxidation states such as a mixed Fe^{II}/Fe^{III} oxide (Fe₃O₄) and Fe^{III} oxides/oxyhydroxides (Fe₂O₃ and FeOOH). These oxides have different hydrolysis and solubility properties in water. Thus, the oxide formed on carbon steel during aqueous corrosion is typically magnetite or Fe^{III} oxides/hydroxides and not FeO/Fe(OH)₂ due to the large solubility of the latter oxides in water.

Table 6.6 Key reactions and transport processes involved in the electrochemical corrosion of carbon steel.

Redox reactions:	(1a) $\text{Fe}^0 \rightarrow \text{Fe}^{\text{II}} + 2 \text{e}^- \rightarrow \text{Fe}^{\text{III}} + 3 \text{e}^-$ (1b) $2 \text{H}_2\text{O} + 2 \text{e}^- \rightarrow \text{H}_2 + 2 \text{OH}^-$, or $\frac{1}{2} \text{O}_2 + 2 \text{e}^- \rightarrow \text{O}^{2-}$
Net transport of $\text{Fe}^{\text{n}+}$ across surface film:	(2) $\text{Fe}^{\text{n}+}(\text{m} \text{f}) \rightarrow \rightarrow \text{Fe}^{\text{n}+}(\text{f} \text{sol})$, where $n = 2$ or 3
Film growth:	(3) $\text{Fe}^{\text{n}+} + (\text{FeO}_x)_f + \text{n}x \text{OH}^-$ (or $\text{n}x/2 \text{O}^{2-}$) $\rightarrow \text{Fe} -- (\text{FeO}_x)_f -- \text{OH}_{\text{n}x}$ (or $\text{O}_{\text{n}x/2}$) $\rightarrow \rightarrow (\text{FeO}_x)_{f+1} + x \text{H}_2\text{O}$
Metal Dissolution:	(4) $\text{Fe}^{\text{n}+}(\text{f} \text{sol}) \rightarrow \rightarrow \text{Fe}^{\text{n}+}(\text{sol})$

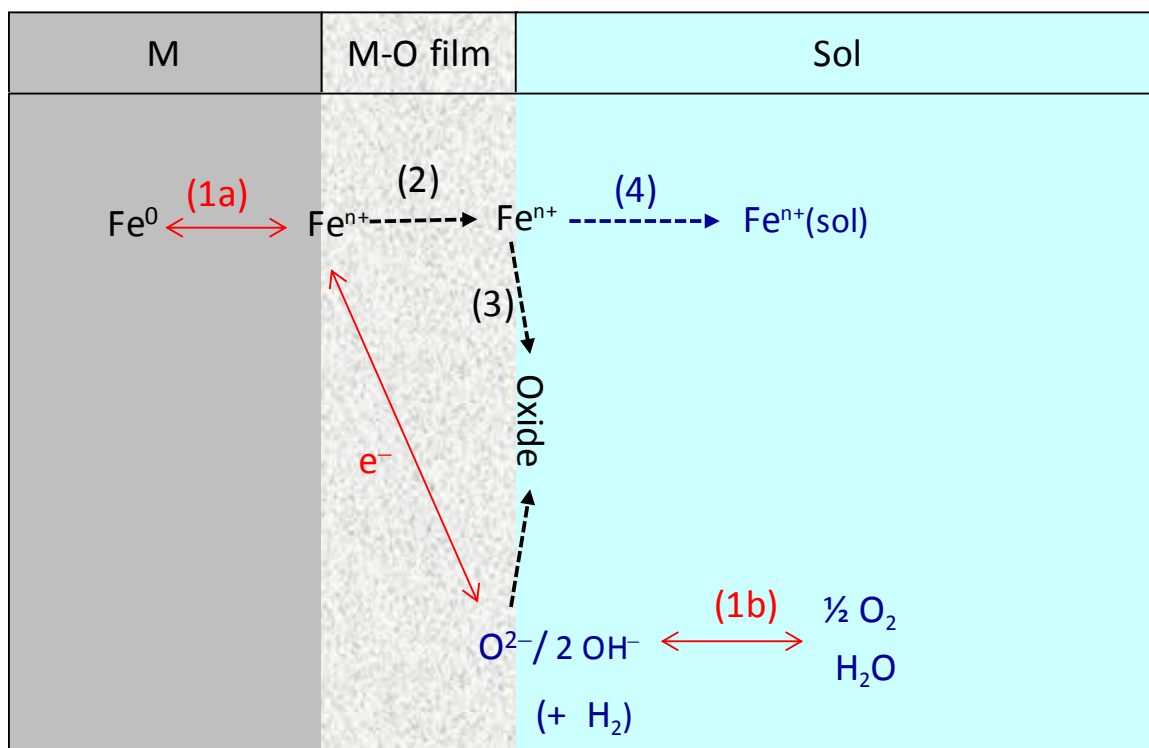


Figure 6.11 A schematic illustration of corrosion reactions in the presence of a surface film. The key reaction steps include: (1a) metal oxidation coupled with (1b) reduction of solution species (in this case H_2O and O_2), (2) net metal cation transport across the solid oxide film, (3) growth of the surface film, and (4) dissolution of a metal cation into the electrolyte solution.

Transition metal oxides are semiconductors. On a chemically inert semiconductor electrode, charge transport through the semiconductor is normally accomplished by electrons (for an n-type semiconductor) and holes (for a p-type semiconductor) [51]. On a corroding surface, charge transport accompanies the net transport of more massive charged species, metal cations and oxygen/hydroxide anions. To account for the charge flux through a solid oxide lattice, many mechanisms, such as transport of metal cations (or oxygen anions) via interstitials, or cation and anion vacancies, and electron hopping (or ion exchanges), have been proposed [52-55]. Irrespective of the ion transport mechanism, the net charge movement in a corroding system is the movement of metal cations from the metal/film interface toward the film/solution interface.

The corrosion mechanism presented in Table 6.6 and Figure 6.11 applies to corrosion of carbon steel in both aqueous and IL solutions. However, there are a few key differences between the two systems. For many transition metals H_2O is an effective oxidant and hence water can function as both an oxidant for the metal and an electrolyte medium that can transport the charged species in the corrosion reactions. The IL studied here (and generally other ILs) is considered to be not redox active with transition metals [18]. Hence, the complexity arising from the solvent molecule participating in the redox reaction is not present. However, the $[\text{P}_{14666}][\text{Br}]$ IL can absorb a considerable amount of H_2O and O_2 . Unfortunately the diffusion rates of these two species in the IL are not known and their migration rates may control the overall corrosion rate. The rate of metal ion dissolution from the solid metal or metal oxide phases depends on the rate of solvation of metal ions from the solid surfaces and the metal ion solubility in the IL. Unfortunately these fundamental properties of the IL are also not known. Nevertheless,

the proposed mechanism can explain the corrosion behaviours observed for the different systems that we examined (pure IL versus the hexane-IL mixture), different cover gas environments, and the absence or presence of γ -radiation.

In the studies of aqueous corrosion of various alloys Behazin et al. have shown that corrosion kinetics can be effectively described by a classical (macroscopic) rate law based on mass and charge balance [50, 56]. That is, the rates of the individual elementary processes in the corrosion mechanism shown in Figure 6.11 cannot vary independently. Mass and charge balance requirements dictate that at any given time, the net rate of corrosion must satisfy

$$\text{Net rate} = \text{rate (1a)} = \text{rate (1b)} = \text{rate (2)} = \text{rate (3)} + \text{rate (4)} \quad (6.1)$$

The mass balance requirement dictates that the rates of reactions that occur in series must be the same and that the overall rate of reactions in parallel is the sum of the individual rates. Hence, the slowest in a series of reactions dictates the oxidation rate, while metal dissolution and oxide film formation compete for the metal cations. If the rate of metal ion dissolution is higher than the rate of solid oxide formation and keeps up with the rate of metal oxidation, there will be no significant build-up of an oxide film. However, if the rate of metal dissolution is slower than the rate of oxide formation or slower than the net metal oxidation rate, the oxide film will grow which, in turn, will impede the transport of metal cations across the film and hence reduce the net corrosion rate. Different corrosion environments influence the rates of the individual steps involved in corrosion differently.

The corrosion behaviours observed for carbon steel in pure [P₁₄₆₆₆] [Br] exposed to different cover gases without irradiation can then be attributed to the different

concentrations of dissolved O_2 and H_2O in the IL. Of those two species, O_2 is the stronger oxidant. The concentrations of dissolved O_2 and H_2O are highest in the IL exposed to open air and lowest in the IL exposed to Ar. Due to the low concentrations of O_2 and H_2O dissolved in the IL exposed to Ar, the rate of Fe oxidation is slow and limited to the more redox active α -ferrite sites, the dissolution of the oxidized metal into the solution can keep up with the oxidation rate, and no oxide film can be formed. This leaves the cementite skeletons on the surface while continuing to expose the fresh α -ferrite surface to the IL solution. With the high concentrations of dissolved O_2 and H_2O in the IL exposed to open and sealed air, the rate of metal oxidation occurs at a much faster rate due to the larger driving force (i.e. the more oxidizing electrolyte environment). The dissolution of Fe^{II} species can't keep up with the metal oxidation rate and the Fe^{II} on the surface can further oxidize to form a mixed Fe^{II}/Fe^{III} oxide (magnetite or Fe_3O_4) and then oxidize further to form Fe^{III} oxides/hydroxides that are not very soluble. The faster these oxides are formed the less dissolution of Fe^{2+} occurs. Under the more oxidizing condition, the metal oxidation occurs on the less reactive cementite sites as well as the more reactive α -ferrite sites. As the metal ion dissolution is suppressed, the oxidative conversion of Fe^{II} to Fe^{II}/Fe^{III} and to Fe^{III} oxides/ hydroxides also occurs at a faster rate. The magnetite formed on a coupon in an IL containing a high concentration of dissolved O_2 is grainy and the fast conversion of the magnetite to Fe_2O_3 creates large gaps between the magnetite grains. Loss of these grains creates pits.

Hexane is a redox inactive compound. However, the addition of 20% hexane to [P₁₄₆₆₆] [Br] increases the transfer rates of the redox species (O_2 and H_2O) from the gas phase to the IL phase and then to the carbon steel surface. Thus, for a given cover gas,

the concentrations of dissolved O_2 and H_2O in the hexane-IL mixture are higher than those in the pure IL, resulting in faster metal oxidation.

Gamma irradiation of $[P_{14666}] [Br]$ generates organic radicals which react readily with O_2 . However, γ -irradiation can also form H_2O_2 or organic super-oxides from the radiolytic decomposition of dissolved water in the IL. Hydrogen peroxide is a stronger oxidant than O_2 and, more importantly reacts faster. Due to the faster oxidation by H_2O_2 and the low iron solubility in the IL phase, the oxidation of Fe on the cementite sites becomes equal in rate to the oxidation on the α -ferrite sites, and in both cases this oxidation progresses very quickly to form Fe_3O_4 , and then Fe_2O_3 and $FeOOH$ before significant dissolution of Fe^{II} species can occur. The result is a smooth uniform oxide layer and a very low concentration of dissolved metal in the IL.

6.5 CONCLUSIONS

The corrosion of carbon steel in $[P_{14666}] [Br]$ in the presence and absence of γ -radiation has been investigated using tests with oxidizing and non-oxidizing cover gases in contact with the IL. Corrosion is seen for all cases in the absence of radiation, with the most substantial corrosion seen for the systems with the most air available. Corrosion is even observed for the case where the IL is in contact with only Ar. The results are explained in terms of the availability of oxygen in the system and the role that dissolved H_2O and O_2 impurities in the IL play in the corrosion.

In the presence of γ -radiation, the rate of corrosion of the carbon steel appears to be slower and more independent of the nature of the cover gas in contact with the IL.

The results are interpreted in terms of the radiolytic formation of H_2O_2 and removal of O_2 in the IL. The H_2O_2 is a stronger oxidant than O_2 and this changes the nature and solubility of the oxide that forms on the carbon steel. The result is a smooth uniform oxide layer and a very low concentration of dissolved metal in the IL.

A corrosion mechanism is presented which explains the observed results in terms of the extent of oxidizing species present in the system and the competition between the rates of dissolution of Fe^{II} species and the formation of less soluble Fe^{III} species. It is known that irradiation of $[\text{P}_{14666}] [\text{Br}]$ leads to the formation of small organic species like hexane. The presence of these species can change the transport properties of the IL, decrease its viscosity, and allow oxidants to migrate more rapidly, thus altering the corrosion rates in the system. Corrosion tests were also performed with a 20% hexane in $[\text{P}_{14666}] [\text{Br}]$ solution to evaluate the impact of the phenomenon. The results of coupon surface analyses and metal dissolution levels are consistent with the proposed mechanism for corrosion in this system. The key driver of the corrosion is the role played by the dissolved O_2 and H_2O in the IL, with the corrosion conditions controlling the thickness and morphology of the oxide that is formed on the carbon steel.

6.6 REFERENCES

- [1] K. Daub, X. Zhang, J.J. Noel, J.C. Wren, *Electrochim. Acta*, 55 (2010) 2767.
- [2] C.T. Lee, M.S. Odziemkowski, D.W. Shoesmith, *J. Electrochem. Soc.*, 153 (2006) B33.
- [3] L.J. Oblonsky, S. Virtanen, V. Schroeder, T.M. Devine, *J. Electrochem. Soc.*, 144 (1997) 1604.
- [4] S. Virtanen, P. Schmuki, A.J. Davenport, C.M. Vitus, *J. Electrochem. Soc.*, 144 (1997) 198.
- [5] K. Yazdanfar, X. Zhang, P.G. Keech, D.W. Shoesmith, J.C. Wren, *Corros. Sci.*, 52 (2010) 1297.

- [6] L. Wang, K. Daub, Z. Qin, J.C. Wren, *Electrochim. Acta*, 76 (2012) 208.
- [7] K. Daub, X. Zhang, L. Wang, Z. Qin, J.J. Noel, J.C. Wren, *Electrochim. Acta*, 56 (2011) 6661.
- [8] W. Xu, K. Daub, X. Zhang, J.J. Noel, D.W. Shoesmith, J.C. Wren, *Electrochim. Acta*, 54 (2009) 5727.
- [9] A. Nishikata, S. Haruyama, *Corrosion* 42 (1986) 578.
- [10] L.C. Olson, J.W. Ambrosek, K. Sridharan, M.H. Anderson, T.R. Allen, *J. Fluorine Chem.*, 130 (2009) 67.
- [11] M. Kondo, T. Nagasaka, Q. Xu, T. Muroga, A. Sagara, N. Noda, D. Ninomiya, M. Nagura, A. Suzuki, T. Terai, N. Fujii, *Fus. Eng. Des.*, 84 (2009) 1081.
- [12] S.H. Cho, J.M. Hur, C.-S. Seo, S.-W. Park, *J. Alloy. Compd.*, 452 (2008) 11.
- [13] M. Uerdingen, C. Treber, M. Balsler, G. Schmitt, C. Werner, *Green Chem.*, 7 (2005) 321.
- [14] A.B. Tolstoguzov, U. Bardi, S.P. Chenakin, *B. Russ. Acad. Sci. Phys.*, 72 (2008) 605.
- [15] A.P. Grosvenor, B.A. Kobe, N.S. McIntyre, *Surf. Sci.*, 565 (2004) 151.
- [16] R. Gupta, S. Sen, *Phys. Rev. B*, 12 (1975) 15.
- [17] A.R. Pratt, I.J. Muir, H.W. Nesbitt, *Geochim. Cosmochim. Acta*, 58 (1994) 827.
- [18] A.P. Abbott, I. Dalrymple, F. Endres, D.R. MacFarlane, *Why Use Ionic Liquids for Electrodeposition?*, in: *Electrodeposition from Ionic Liquids*, F. Endres, D.R. MacFarlane, A. Abbott, Editors, Wiley-VCH Verlag, Weinheim, Germany (2008).
- [19] S.E. Howett, J.M. Joseph, J.J. Noel, J.C. Wren, *J. Colloid Interface Sci.*, 361 (2011) 338.
- [20] R.P. Morco, J.M. Joseph, J.C. Wren, *Green Chem.*, (2014) Submitted.
- [21] U. Schroder, J.D. Wadhawan, R.G. Compton, F. Marken, P.A.Z. Suarez, C.S. Consorti, R.F. de Souza, J. Dupont, *New J. Chem.*, 24 (2000) 1009.
- [22] A.M. O'Mahony, D.S. Silvester, L. Aldous, C. Hardacre, R.G. Compton, *J. Chem. Eng. Data*, 53 (2008) 2884.
- [23] Cytec product sheet CYPHOS® IL 102 and 109, <https://www.cytec.com/specialty-chemicals/ionicliquidstable.htm> <Accessed: February 26, 2013>.
- [24] J.W. Vaughan, D. Dreisinger, J. Haggins, *ECS Trans.*, 2 (2006) 381.
- [25] M.G. Freire, P.J. Carvalho, R.L. Gardas, L.M.N.B.F. Santos, I.M. Marrucho, J.A.P. Coutinho, *J. Chem. Eng. Data*, 53 (2008) 2378.
- [26] D.S. Zhou, G.J. Shiflet, *Metall. Mater. Trans. A*, 23 (1992) 1259.
- [27] R. Cabrera-Sierra, N. Batina, I. González, *Mat. Chem. Phys.*, 96 (2006) 343.
- [28] D.T. Llewellyn, R.C. Hudd, *Steels: Metallurgy and Applications*, Butterworth-Heinemann, Oxford, UK (1998).
- [29] W.D. Callister Jr., *Materials Science and Engineering: An Introduction*, John Wiley & Sons, New York, NY (2003).
- [30] O.N. Shebanova, P. Lazor, *J. Solid State Chem.*, 174 (2003) 424.
- [31] A.E. Kehew, *Applied Chemical Hydrogeology*, Prentice Hall, Upper Saddle River, NJ (2001).
- [32] C.F. Baes Jr., R.E. Mesmer, *The Hydrolysis of Cations*, Krieger Publishing Co., Florida (1986).

- [33] C.F. Baes, R.E. Mesmer, *Am. J. Sci.*, 281 (1981) 935.
- [34] R.H. Byrne, Y.R. Luo, R.W. Young, *Mar. Chem.*, 70 (2000) 23.
- [35] M. Büchler, *J. Electrochem. Soc.*, 145 (1998) 609.
- [36] M. Büchler, *J. Electrochem. Soc.*, 144 (1997) 2307.
- [37] K. Daub, X. Zhang, J.J. Noel, J.C. Wren, *Corros. Sci.*, 53 (2011) 11.
- [38] M.C. Biesinger, B.P. Payne, A.P. Grosvenor, L.W.M. Lau, A.R. Gerson, R.S. Smart, *Appl. Surf. Sci.*, 257 (2011) 2717.
- [39] A.P. Grosvenor, B.A. Kobe, M.C. Biesinger, N.S. McIntyre, *Surf. Interface Anal.*, 36 (2004) 1564.
- [40] A.P. Grosvenor, B.A. Kobe, N.S. McIntyre, *Surf. Sci.*, 572 (2004) 217.
- [41] D.T. Reed, R.A. Van Konynenburg, *Mater. Res. Soc. Symp.P.*, 112 (1987) 393.
- [42] G. Glowa, P. Driver, J.C. Wren, *Radiat. Phys. Chem.*, 58 (2000) 49.
- [43] P. Driver, G. Glowa, J.C. Wren, *Radiat. Phys. Chem.*, 57 (2000) 37.
- [44] J.C. Wren, G.A. Glowa, *Radiat. Phys. Chem.*, 58 (2000) 341.
- [45] J.M. Joseph, B.S. Choi, P. Yakabuskie, J.C. Wren, *Radiat. Phys. Chem.*, 77 (2008) 1009.
- [46] P.A. Yakabuskie, J.M. Joseph, J.C. Wren, *Radiat. Phys. Chem.*, 79 (2010) 777.
- [47] K. Daub, X. Zhang, J.J. Noël, J.C. Wren, *ECS Trans.*, 33 (2011) 15.
- [48] K.J. Daub, X.Y. Zhang, J.J. Noel, D.W. Shoesmith, J.C. Wren, *Abstr. Pap. Am. Chem. Soc.*, 238 (2009).
- [49] J. Wang, A. Zhu, Y. Zhao, K. Zhuo, *J. Solution Chem.*, 34 (2005) 585.
- [50] M. Behazin, J.J. Noel, J.C. Wren, *Electrochim. Acta*, 134 (2014) 399.
- [51] N. Perez, *Electrochemistry and Corrosion Science*, Kluwer Academic Publishers, Boston (2004).
- [52] C.Y. Chao, *J. Electrochem. Soc.*, 128 (1981) 1187.
- [53] B. Krishnamurthy, R.E. White, H.J. Ploehn, *Electrochim. Acta*, 46 (2001) 3387.
- [54] A. Seyeux, V. Maurice, P. Marcus, *J. Electrochem. Soc.*, 160 (2013) C189.
- [55] M. Kamrunnahar, J. Bao, D.D. MacDonald, *Corros. Sci.*, 47 (2005) 3111.
- [56] M. Behazin, M.C. Biesinger, J.J. Noel, J.C. Wren, *Corros. Sci.*, 63 (2012) 40.

Chapter 7

Summary and Future Work

7.1 SUMMARY

This thesis examined the properties and behaviour of a little-studied class of ionic liquids, phosphonium-based ILs. The work looked at several ILs with two different cations and several different anions. The first part of the work was a theoretical analysis of the IL molecular structure and properties. Quantum chemical calculation on six phosphonium ILs with a [P₁₄₆₆₆] cation paired to [Cl], [Br], [DCA], [BF₄], [PF₆] and [NTf₂] anions were performed using density functional theory. The inter-ionic H-bond length and angle, the HOMO and LUMO energy gap, the dipole moment, the cation-anion interaction energy, and the electrostatic potential were calculated for each IL. To test the validity of the calculations, the wavelengths and oscillator strengths of vibrational and electronic transition lines of the ILs were also calculated and compared with measured IR and UV-Vis absorption spectra for the ILs. The calculated spectral lines were in good agreement with those of the measured spectra.

We have found strong correlations between the calculated quantum chemical parameters that describe the ILs and the measured physical and chemical properties of the ILs. We found that the molar conductivity increases, whereas the viscosity decreases, exponentially, with the dipole moment for the ILs, and the melting point increases linearly with interaction energy. The strong correlations are somewhat surprising since

most of the correlated properties are mainly governed by the intermolecular interactions with other IL pairs and not just on the interionic forces within a single pair (the theoretical calculation did not address inter-pair forces). We think that the good correlations may arise because the strength of the intermolecular interactions is proportional to the intramolecular Coulombic interaction in the bulky and viscous phosphonium ILs. Confirming this type of supposition is often addressed by molecular dynamic calculations (MD) on IL clusters of different sizes. However such calculations require supercomputers to accommodate large-scale MD calculations that are required and this is an option for future work.

The effects of ionizing radiation on phosphonium-based ILs and the role of ionizing radiation on the corrosion of carbon steel in an IL have also been explored. Five phosphonium ILs with different physical properties were subjected to gamma irradiation to test their chemical stability. Airborne radiolysis products were analyzed using GC-MS and the IL phase was analyzed using UV-Vis, FTIR and Raman spectroscopy, and conductivity measurement. The ILs experienced negligible radiolytic degradation, even after receiving a total dose of 768 Gy. Those airborne decomposition products detected were small volatile organic molecules formed from the radiolytic dissociation of alkyl chains in the cation moiety. They were only in a very minute fraction of the IL and the IL phase showed no apparent changes in the IL structures as determined using the UV-Vis, FTIR and Raman spectroscopy. Colour changes were observed in the irradiated ILs and these are attributed to agglomeration of IL ion pairs around the radiolytically-formed small organic molecules. This agglomeration was seen in the increased intensity and

scattering background of UV-Vis and Raman spectra, respectively. A drop in the conductivities of the ILs with increased irradiation time corroborates this observation.

The corrosion of carbon steel in [P₁₄₆₆₆] [Br] was studied in the presence and absence of γ -radiation using tests with oxidizing and non-oxidizing cover gases in contact with the IL. In the absence of radiation, substantial corrosion is seen with both cover gases, with the greatest corrosion in the system with the most air available. Corrosion is even observed for the case where the IL is in contact with inert Ar. The results are explained in terms of the availability of oxygen in the system and the role that dissolved H₂O and O₂ impurities in the IL play in the corrosion. In the presence of γ -radiation, the rate of corrosion of the carbon steel appears to be slower and more independent of the nature of the cover gas in contact with the IL. The results are interpreted in terms of the radiolytic formation of H₂O₂ from the H₂O impurity and the consumption of available O₂ by reactions with alkyl organic radicals formed by irradiation of the IL. The H₂O₂ is a stronger oxidant than O₂ and this changes the nature and solubility of the oxide that forms on the carbon steel. The result is a thinner, smooth uniform oxide layer and a very low concentration of dissolved metal loss.

7.2 FUTURE WORK

This research has added to our understanding of the effect of the γ -radiation on the chemical stability of phosphonium ILs and how it can influence the corrosion of a metal alloy. While the measurements that have been performed have been useful in assessing the overall stability of the studied ILs in a radiation field, it would be advantageous if future work looked at the other sensitive properties of the ILs. A

measurement of the electrochemical potential window of the ILs with and without irradiation would be ideal since this property of the IL determines its applicability for the recovery of metals by electrodeposition. Irradiated ILs also can be further analyzed for their thermal stability by differential scanning calorimetry. The small organic molecules formed during irradiation could have affected the melting points of the ILs which can be determined by this technique.

The chemical analysis of radiolysis products performed here was restricted to the airborne products and future work should extend the analysis to the IL phase using chromatographic techniques.

The concentration of airborne products detected in the headspace was found to increase with irradiation time. A more detailed time dependent study of radiolysis would further our understanding of the underlying kinetics of radiolysis as a function of time. While the quantities of radiolysis products appeared to be very low, their accumulation over a long period of irradiation could pose issues for IL applications.

The corrosion behavior of carbon steel in the [P₁₄₆₆₆] [Br] was very interesting. The extent of corrosion without irradiation was somewhat surprising and the suppression of corrosion by irradiation was even more so. We believe that the corrosion of carbon steel in the IL is influenced by the oxidizing species present in the IL solution. The IL used in this study is known to be hygroscopic and can dissolve up to 7% H₂O accompanied by dissolved O₂. Purification of ILs is known to be difficult and a hygroscopic IL like [P₁₄₆₆₆] [Br] can be expected to normally contain a significant amount of H₂O plus O₂. Future work should look at variations in [P₁₄₆₆₆] ILs with respect

to their viscosities water uptake to isolate the effects of different oxidizing species in an IL. It would also be worthwhile investing effort into purifying ILs to remove initial amounts of dissolved H₂O and O₂. This would allow testing with controlled levels of these additives present.

There are many different options for the anion component of a phosphonium IL. In particular ILs with anions that contain fluorine (such as [P₁₄₆₆₆] [NTf₂]). It would be interesting to study metal alloy corrosion in such ILs, because they had been reported to decompose to release a wide range of fluorinated compounds. This could promote challenging interfacial reactions between the IL and steel alloys in the presence γ -radiation as halogens are well known to cause severe degradation in steel alloys.

The corrosion studies performed in this work were limited to carbon steel. There are many other alloys that are candidate materials for IL applications (including stainless steels and nickel alloys) It would be valuable to extend the corrosion studies to other systems where different oxides can form to see how radiation could affect corrosion of those other alloys. As in many corrosion studies, direct electrochemical measurements of the redox processes occurring at the metal interface would be very beneficial in explicating the step by step corrosion process that occurs in an IL. This type of work, however, poses a challenge since the availability of an appropriate reference electrode for use in IL studies is a major issue. Development of such an electrode could be a valuable endeavor.

The applicability of MD calculation to simulate the effects of small organic molecules in cluster of IL would be very useful in understanding the microscopic phenomena observe during the irradiation of ILs.

Appendix A

Copyright Permission

ELSEVIER LICENSE TERMS AND CONDITIONS

Sep 05, 2014

This is a License Agreement between Ryan P. Morco ("You") and Elsevier ("Elsevier") provided by Copyright Clearance Center ("CCC"). The license consists of your order details, the terms and conditions provided by Elsevier, and the payment terms and conditions.

All payments must be made in full to CCC. For payment instructions, please see information listed at the bottom of this form.

Supplier	Elsevier Limited The Boulevard, Langford Lane Kidlington, Oxford, OX5 1GB, UK
Registered Company Number	1982084
Customer name	Ryan P. Morco
Customer address	ChB 027, Dept. of Chemistry London, ON N6A 5B7
License number	3462680890913
License date	Sep 05, 2014
Licensed content publisher	Elsevier
Licensed content publication	Solid State Ionics
Licensed content title	The molecular structures and the relationships between the calculated molecular and observed bulk phase properties of phosphonium-based ionic liquids
Licensed content author	Ryan P. Morco, Ahmed Y. Musa, J. Clara Wren
Licensed content date	1 May 2014
Licensed content volume number	258
Licensed content issue number	n/a
Number of pages	8
Start Page	74
End Page	81

Type of Use	reuse in a thesis/dissertation
Portion	full article
Format	both print and electronic
Are you the author of this Elsevier article?	Yes
Will you be translating?	No
Title of your thesis/dissertation	Effect of Gamma Radiation on the Interfacial Reactions and transfer Processes of Phosphonium-based Ionic Liquids with Carbon Steel
Expected completion date	Sep 2014
Estimated size (number of pages)	180
Elsevier VAT number	GB 494 6272 12
Permissions price	0.00 USD
VAT/Local Sales Tax	0.00 USD / 0.00 GBP
Total	0.00 USD
Terms and Conditions	

INTRODUCTION

1. The publisher for this copyrighted material is Elsevier. By clicking "accept" in connection with completing this licensing transaction, you agree that the following terms and conditions apply to this transaction (along with the Billing and Payment terms and conditions established by Copyright Clearance Center, Inc. ("CCC"), at the time that you opened your Rightslink account and that are available at any time at <http://myaccount.copyright.com>).

GENERAL TERMS

2. Elsevier hereby grants you permission to reproduce the aforementioned material subject to the terms and conditions indicated.

3. Acknowledgement: If any part of the material to be used (for example, figures) has appeared in our publication with credit or acknowledgement to another source, permission must also be sought from that source. If such permission is not obtained then that material may not be included in your publication/copies. Suitable acknowledgement to the source must be made, either as a footnote or in a reference list at the end of your publication, as follows:

“Reprinted from Publication title, Vol /edition number, Author(s), Title of article / title of chapter, Pages No., Copyright (Year), with permission from Elsevier [OR APPLICABLE SOCIETY COPYRIGHT OWNER].” Also Lancet special credit - “Reprinted from The Lancet, Vol. number, Author(s), Title of article, Pages No., Copyright (Year), with permission from Elsevier.”

4. Reproduction of this material is confined to the purpose and/or media for which permission is hereby given.

5. Altering/Modifying Material: Not Permitted. However figures and illustrations may be altered/adapted minimally to serve your work. Any other abbreviations, additions, deletions and/or any other alterations shall be made only with prior written authorization of Elsevier Ltd.

6. If the permission fee for the requested use of our material is waived in this instance, please be advised that your future requests for Elsevier materials may attract a fee.

7. Reservation of Rights: Publisher reserves all rights not specifically granted in the combination of (i) the license details provided by you and accepted in the course of this licensing transaction, (ii) these terms and conditions and (iii) CCC's Billing and Payment terms and conditions.

8. License Contingent Upon Payment: While you may exercise the rights licensed immediately upon issuance of the license at the end of the licensing process for the transaction, provided that you have disclosed complete and accurate details of your proposed use, no license is finally effective unless and until full payment is received from you (either by publisher or by CCC) as provided in CCC's Billing and Payment terms and conditions. If full payment is not received on a timely basis, then any license preliminarily granted shall be deemed automatically revoked and shall be void as if never granted. Further, in the event that you breach any of these terms and conditions or any of CCC's Billing and Payment terms and conditions, the license is automatically revoked and shall be void as if never granted. Use of materials as described in a revoked license, as well as any use of the materials beyond the scope of an unrevoked license, may constitute copyright infringement and publisher reserves the right to take any and all action to protect its copyright in the materials.

9. Warranties: Publisher makes no representations or warranties with respect to the licensed material.

10. Indemnity: You hereby indemnify and agree to hold harmless publisher and CCC, and their respective officers, directors, employees and agents, from and against any and all claims arising out of your use of the licensed material other than as specifically authorized pursuant to this license.

11. No Transfer of License: This license is personal to you and may not be sublicensed, assigned, or transferred by you to any other person without publisher's written permission.

12. No Amendment Except in Writing: This license may not be amended except in a writing signed by both parties (or, in the case of publisher, by CCC on publisher's behalf).

13. Objection to Contrary Terms: Publisher hereby objects to any terms contained in any purchase order, acknowledgment, check endorsement or other writing prepared by you,

which terms are inconsistent with these terms and conditions or CCC's Billing and Payment terms and conditions. These terms and conditions, together with CCC's Billing and Payment terms and conditions (which are incorporated herein), comprise the entire agreement between you and publisher (and CCC) concerning this licensing transaction. In the event of any conflict between your obligations established by these terms and conditions and those established by CCC's Billing and Payment terms and conditions, these terms and conditions shall control.

14. **Revocation:** Elsevier or Copyright Clearance Center may deny the permissions described in this License at their sole discretion, for any reason or no reason, with a full refund payable to you. Notice of such denial will be made using the contact information provided by you. Failure to receive such notice will not alter or invalidate the denial. In no event will Elsevier or Copyright Clearance Center be responsible or liable for any costs, expenses or damage incurred by you as a result of a denial of your permission request, other than a refund of the amount(s) paid by you to Elsevier and/or Copyright Clearance Center for denied permissions.

LIMITED LICENSE

The following terms and conditions apply only to specific license types:

15. **Translation:** This permission is granted for non-exclusive world **English** rights only unless your license was granted for translation rights. If you licensed translation rights you may only translate this content into the languages you requested. A professional translator must perform all translations and reproduce the content word for word preserving the integrity of the article. If this license is to re-use 1 or 2 figures then permission is granted for non-exclusive world rights in all languages.

16. **Posting licensed content on any Website:** The following terms and conditions apply as follows: Licensing material from an Elsevier journal: All content posted to the web site must maintain the copyright information line on the bottom of each image; A hyper-text must be included to the Homepage of the journal from which you are licensing at <http://www.sciencedirect.com/science/journal/xxxxxx> or the Elsevier homepage for books at <http://www.elsevier.com>; Central Storage: This license does not include permission for a scanned version of the material to be stored in a central repository such as that provided by Heron/XanEdu.

Licensing material from an Elsevier book: A hyper-text link must be included to the Elsevier homepage at <http://www.elsevier.com> . All content posted to the web site must maintain the copyright information line on the bottom of each image.

Posting licensed content on Electronic reserve: In addition to the above the following clauses are applicable: The web site must be password-protected and made available only to bona fide students registered on a relevant course. This permission is granted for 1 year

only. You may obtain a new license for future website posting.

For journal authors: the following clauses are applicable in addition to the above: Permission granted is limited to the author accepted manuscript version* of your paper.

***Accepted Author Manuscript (AAM) Definition:** An accepted author manuscript (AAM) is the author's version of the manuscript of an article that has been accepted for publication and which may include any author-incorporated changes suggested through the processes of submission processing, peer review, and editor-author communications. AAMs do not include other publisher value-added contributions such as copy-editing, formatting, technical enhancements and (if relevant) pagination.

You are not allowed to download and post the published journal article (whether PDF or HTML, proof or final version), nor may you scan the printed edition to create an electronic version. A hyper-text must be included to the Homepage of the journal from which you are licensing at <http://www.sciencedirect.com/science/journal/xxxxx>. As part of our normal production process, you will receive an e-mail notice when your article appears on Elsevier's online service ScienceDirect (www.sciencedirect.com). That e-mail will include the article's Digital Object Identifier (DOI). This number provides the electronic link to the published article and should be included in the posting of your personal version. We ask that you wait until you receive this e-mail and have the DOI to do any posting.

Posting to a repository: Authors may post their AAM immediately to their employer's institutional repository for internal use only and may make their manuscript publically available after the journal-specific embargo period has ended.

Please also refer to Elsevier's Article Posting Policy for further information.

18. For book authors the following clauses are applicable in addition to the above: Authors are permitted to place a brief summary of their work online only.. You are not allowed to download and post the published electronic version of your chapter, nor may you scan the printed edition to create an electronic version. **Posting to a repository:** Authors are permitted to post a summary of their chapter only in their institution's repository.

20. Thesis/Dissertation: If your license is for use in a thesis/dissertation your thesis may be submitted to your institution in either print or electronic form. Should your thesis be published commercially, please reapply for permission. These requirements include permission for the Library and Archives of Canada to supply single copies, on demand, of the complete thesis and include permission for UMI to supply single copies, on demand, of the complete thesis. Should your thesis be published commercially, please reapply for permission.

Elsevier Open Access Terms and Conditions

Elsevier publishes Open Access articles in both its Open Access journals and via its Open Access articles option in subscription journals.

Authors publishing in an Open Access journal or who choose to make their article Open Access in an Elsevier subscription journal select one of the following Creative Commons user licenses, which define how a reader may reuse their work: Creative Commons Attribution License (CC BY), Creative Commons Attribution – Non Commercial - ShareAlike (CC BY NC SA) and Creative Commons Attribution – Non Commercial – No Derivatives (CC BY NC ND)

Terms & Conditions applicable to all Elsevier Open Access articles:

Any reuse of the article must not represent the author as endorsing the adaptation of the article nor should the article be modified in such a way as to damage the author's honour or reputation.

The author(s) must be appropriately credited.

If any part of the material to be used (for example, figures) has appeared in our publication with credit or acknowledgement to another source it is the responsibility of the user to ensure their reuse complies with the terms and conditions determined by the rights holder.

Additional Terms & Conditions applicable to each Creative Commons user license:

CC BY: You may distribute and copy the article, create extracts, abstracts, and other revised versions, adaptations or derivative works of or from an article (such as a translation), to include in a collective work (such as an anthology), to text or data mine the article, including for commercial purposes without permission from Elsevier

CC BY NC SA: For non-commercial purposes you may distribute and copy the article, create extracts, abstracts and other revised versions, adaptations or derivative works of or from an article (such as a translation), to include in a collective work (such as an anthology), to text and data mine the article and license new adaptations or creations under identical terms without permission from Elsevier

CC BY NC ND: For non-commercial purposes you may distribute and copy the article and include it in a collective work (such as an anthology), provided you do not alter or modify the article, without permission from Elsevier

Any commercial reuse of Open Access articles published with a CC BY NC SA or CC BY NC ND license requires permission from Elsevier and will be subject to a fee.

Commercial reuse includes:

- Promotional purposes (advertising or marketing)
- Commercial exploitation (e.g. a product for sale or loan)
- Systematic distribution (for a fee or free of charge)

Please refer to Elsevier's Open Access Policy for further information.

Curriculum Vitae

Ryan Peñaranda Morco

EDUCATION

2011– 2014 M.Sc. Chemistry, Western University, London ON, Canada
Supervisor, Dr. J.C. Wren

2000 – 2004 B.Sc. Chemistry, Cagayan State University, Philippines

WORK EXPERIENCE

May 2011 – present
Graduate Research Assistant

- Planned and implemented research project on ionic liquids:
 - 1) theoretical/computational studies on ionic liquids bulk properties and
 - 2) effect of gamma radiation on ionic liquid/gas and ionic liquid/solid interaction.
- Prepared and presented research findings to supervisor by creating a detailed report

Sept. 2011- Apr 2013
Teaching Assistant, Western University

- Chemistry 1100 (General Chemistry), Chemistry 1024 (Engineering Chemistry), Chemistry 2214 (Phys. Chem.)

Feb 2005- Apr 2011
Science Research Specialist, Philippine Nuclear Research Institute
Philippines

Jun 2004 – Dec 2004
Laboratory Technician, Chromatography Section, QC Lab
United Laboratories Inc., Philippines

GRADUATE COURSES

- Chemistry 9764, Spectroscopy and Microscopy in Materials Research, Instructor Dr. F. Lagugné-Labarhet (September 2011)
- Chemistry 9724, Materials Analysis Using Synchrotron Radiation, Instructor Dr. T.K. Sham (September 2011, January 2012)
- Chemistry 9658, Graduate Seminar on “Chemical Fingerprinting of Historic Works of Art” (December 2013)

AWARDS AND ACHIEVEMENTS

- Western Graduate Research Scholarships (WGRS), 2011 – 2013
- Academic Excellence Award 2004, Cagayan State University
- Registered/Licensed Chemist, Board of Chemistry, Philippine Professional Regulation Commission (since 2004)

POSTERS AND PRESENTATIONS, * indicates presenting author

R.P. Morco^{*}, J.M. Joseph, A.Y. Musa, J.C. Wren, The Effect of Gamma Radiation on Phosphonium Ionic Liquids: Its Stability and Interaction towards Solid, Annual UNENE workshop, Toronto, Ontario, December 10, 2013.

R.P. Morco^{*}, J.M. Joseph, A.Y. Musa, J.C. Wren, Corrosion properties of phosphonium-based ionic liquids towards carbon steel, Surface Canada Conference 2013 Student Conference, London, Ontario, May 8, 2013.

R.P. Morco^{*}, J.M. Joseph, A.Y. Musa, J.C. Wren, Effect of phosphonium-based ionic liquids on the corrosion of carbon steel under gamma radiation, 29th Annual Canadian Nuclear Society Conference and 36th Annual CNS/CNA Student Conference, Saskatoon, Saskatchewan, June 12, 2012.

ARTICLES IN PEER-REVIEWED JOURNALS

R.P. Morco, J.M. Joseph, A.Y. Musa, J.C. Wren, Corrosion Behaviour of Carbon Steel in [P14666][Br]: The Effects of γ -Radiation and Cover Gas, Corrosion Science. Submitted.

R.P. Morco, J.M. Joseph, J.C. Wren, The Chemical Stability of Phosphonium-based Ionic liquids under Gamma Irradiation, Green Chemistry. Submitted.

R.P. Morco, A.Y. Musa, J.C. Wren, The molecular structures and the relationships between the calculated molecular and observed bulk phase properties of phosphonium-based ionic liquids, Solid State Ionics 258 (2014) 74-81.

P.C.B. Pabroa, F.L. Santos, **R.P. Morco**, J.M.D. Racho, A.T. Bautista VII, C.G.D. Bucal, Receptor modeling studies for the characterization of air particulate lead pollution sources in Valenzuela sampling site (Philippines), Atmospheric Pollution Research 2 (2011) 213-218.

F.L. Santos, P.C.B. Pabroa, **R.P. Morco**, J.M.D. Racho, Elemental characterization of inhalable particulate emissions on New Year's Day in Metro Manila, Philippine Nuclear Journal 15 (2010) 35-43.